DOT/FAA/TC-26/19

Federal Aviation Administration
William J. Hughes Technical Center
for Advanced Aerospace
Aviation Research Division
Atlantic City International Airport
New Jersey 08405

National Airport Pavement Test Facility Construction Cycle 9

Volume 5—Flexible Pavement Overload Test

April 2026

Final Report

U.S. Department of Transportation
Federal Aviation Administration

NOTICE

Technical Report Documentation Page

1. Report No.	2. Government Accession No.	3. Recipient's Catalog No.
DOT/FAA/TC-26/19		

4. Title and Subtitle	5. Report Date
NATIONAL AIRPORT PAVEMENT TEST FACILITY CONSTRUCTION CYCLE 9 VOLUME 5—FLEXIBLE PAVEMENT OVERLOAD TEST	April 2026
	6. Performing Organization Code ANG-E262

7. Author(s)	8. Performing Organization Report No.
Hasan Kazmee*, Scott Murrell*, Ebenezer Duah*, Daniel I. Offenbacker, and David R. Brill	

9. Performing Organization Name and Address	10. Work Unit No. (TRAIS)
U.S. Department of Transportation Federal Aviation Administration Airport Pavement R&D Section William J. Hughes Technical Center for Advanced Aerospace Atlantic City International Airport, NJ 08405 *ARA, Inc. 2628 Fire Road Suite 300 Egg Harbor Twp, NJ 08234	11. Contract or Grant No. 692M15-21-D-00004

12. Sponsoring Agency Name and Address	13. Type of Report and Period Covered
U.S. Department of Transportation Federal Aviation Administration Airport Engineering Division 800 Independence Ave., SW Washington, DC 20591	Final Report
	14. Sponsoring Agency Code AAS-100

15. Supplementary Notes

The Federal Aviation Administration Contracting Officer's Representative (COR) was Murphy Flynn.

16. Abstract

The Federal Aviation Administration (FAA) conducted traffic tests of full-scale flexible airport pavements at the National Airport Pavement Test Facility (NAPTF) as part of Construction Cycle 9 (CC9). Within CC9, the Flexible Pavement Overload Test was designed to develop International Civil Aviation Organization (ICAO) criteria for allowable overload operations. ICAO Annex 14 currently suggests that airports should limit overloads to aircraft having an Aircraft Classification Rating (ACR) not exceeding 10% above the Pavement Classification Rating (PCR). In CC9, the overload test consisted of two test items with the same cross-section but different load histories. One overload test item was subjected to overload traffic up to 75% above PCR, while a second test item received the same regular traffic but did not receive overloads. The overload test was concluded after 56,100 passes of the test vehicle simulating slow-roll taxi operations, in addition to three overload series. Pavement performance was monitored by regular visual distress surveys, nondestructive testing (NDT), and in-pavement sensors. Test results showed that (a) neither the control test item nor the test item with 75% above PCR overloads experienced full structural failure after more than 56,000 passes; (b) both test items experienced significant rutting and extensive surface cracking constituting a functional failure; and (c) measured vertical strains at the top of the clay subgrade differed significantly from the design strains, and continued to increase with accumulated traffic. In part because of the unpredictability of in situ strain and its dependence on non-load factors, the authors propose an alternative criterion for allowable overloads based on the subgrade shear stress ratio (SSR).

17. Key Words	18. Distribution Statement
National Airport Pavement Test Facility, Flexible airport pavement, ACR/PCR, Overload	This document is available to the U.S. public through the National Technical Information Service (NTIS), Springfield, Virginia 22161. This document is also available from the Federal Aviation Administration William J. Hughes Technical Center for Advanced Aerospace at actlibrary.tc.faa.gov.

19. Security Classif. (of this report)	20. Security Classif. (of this page)	21. No. of Pages	22. Price
Unclassified	Unclassified	125	

TABLE OF CONTENTS

		Page
EXECUTIVE SUMMARY		xii
1.	INTRODUCTION	1
1.1	Background	1
1.2	Objective and Scope	1
1.3	National Airport Pavement Test Facility Terminology	1
1.3.1	Test Terminology	1
1.3.2	Work Item Modifiers	2
2.	DESIGN AND CONSTRUCTION OF TEST AREAS	2
2.1	Review of Construction Quality Control and Assurance	5
2.1.1	Placement and Compaction of Subgrade (P-152MR)	5
2.1.2	Placement and Compaction of Subbase Course (P-154MR)	6
2.1.3	Placement and Compaction of Base Course (P-209MR)	6
2.1.4	Placement and Compaction of Asphalt Concrete (P-401MR)	6
2.2	In-Place Testing for Construction Uniformity	7
2.2.1	Subgrade (P-152MR)	8
2.2.2	Subbase Course (P-154MR)	13
2.2.3	Base Course (P-209 MR)	16
2.2.4	Asphalt Concrete (P-401MR)	19
2.3	Review of Instrumentation	20
2.3.1	Asphalt Strain Gages	20
2.3.2	Pressure Cells	21
2.3.3	Coil Sensors	21
2.3.4	Static Sensors	21
3.	LABORATORY MATERIAL CHARACTERIZATION	21
3.1	Resilient Modulus of Granular Materials	22
3.1.1	Subgrade	23
3.1.2	Granular Subbase	23
3.1.3	Base Course	23

3.2 Asphalt Concrete 27

3.2.1 Dynamic Modulus 27
3.2.2 Rutting-Related Tests 27
3.2.3 Cracking-Related Tests 31

4. TRAFFIC TESTS ON OVERLOAD TEST ITEMS 36

4.1 Overload Ratio 36
4.2 Pre-Traffic Tests 37

4.2.1 Slow-Roll Response Tests 37
4.2.2 Ramp-up Response Test 40
4.2.3 Baseline NDT 40

4.3 Traffic Tests 43

4.3.1 Traffic Loading Sequence 43
4.3.2 Wander Pattern 43
4.3.3 Failure Criteria 47
4.3.4 Traffic History 47
4.3.5 Routine Monitoring and Testing 47

5. TEST RESULTS AND DISCUSSION 49

5.1 Surface Monitoring Data 49

5.1.1 Upheaval and Rutting 49
5.1.2 Cracking 51

5.2 Sensor Response Data 55

5.2.1 Asphalt Sensors 55
5.2.2 Subbase Sensors 61
5.2.3 Subgrade Sensors 62

5.3 Nondestructive Testing Analysis 66
5.4 Failure Condition Analysis 74
5.5 Subgrade Response Analysis 77
5.6 Overload Criteria Based on Shear Stress Ratio 84

6. CONCLUSIONS 89

7. REFERENCES 90

APPENDICES

A—Layout of Sensors in Overload Test Items
B—Maximum Upheavals in Construction Cycle 9 Overload Test Items C—Visual Distress Log
D—Distress Map
E—Aircraft Classification Number/Pavement Classification Number and Aircraft Classification Rating/Pavement Classification Rating Calculations
F—Finite Element Model Assumptions and Conditions

LIST OF FIGURES

Figure		Page
1	Satellite Image of the CC9 Test Area and the CC9 Overload Test Area	3
2	Plan View of the CC9 Test Areas and Items	4
3	As-Built Cross-Sections of Overload Test Items	5
4	Construction Cycle 9 Subgrade CBR Test Locations	9
5	As-Built Subgrade Shear Strength in Overload Test Items Measured with Vane Shear Tests	9
6	As-Built Subgrade Modulus in Overload Test Items Measured with Light Weight Deflectometer	11
7	As-Built Subgrade Seismic Modulus in Overload Test Items Measured with D-PSPA	12
8	As-Built Subgrade Modulus in Overload Test Items Measured with GeoGauge	13
9	As-Built Subbase Modulus in Overload Test Items Measured with LWD	14
10	As-Built Subbase Seismic Modulus in Overload Test Items Measured with D-PSPA	15
11	As-Built Subbase Modulus in Overload Test Items Measured with GeoGauge	16
12	As-Built Base Modulus in Overload Test Items Measured with LWD	17
13	As-Built Base Seismic Modulus in Overload Test Items Measured with D-PSPA	18
14	As-Built Base Modulus in Overload Test Items Measured with GeoGauge	19
15	Layout of Instrumentation in Overload Test Item LFC-5N	20
16	Layout of Instrumentation in Overload Test Item LFC-5S	21
17	Resilient Modulus of Granular Subbase Sampled During the Construction of Overload Test Items	25
18	Resilient Modulus of Crushed Aggregate Base Sampled During the Construction of Overload Test Items	26
19	Dynamic Modulus Master Curves, Phase Angle Master Curves, and Black Space Diagram of CC9 Asphalt Concrete Mixes	28

20	Asphalt Pavement Analyzer Rut Depths of PG 64-22 Mix used in CC9 Overload Test Items at 100-psi and 250-psi Hose Pressures	29
21	Flow Number of PG 64-22 Mix Used in CC9 Overload Test Items	30
22	Initial Flexural Stiffness, Fatigue Life at Three Strain Levels, Predicted Plateau Values, and Predicted Fatigue Life of PG 64-22 Mix used in Overload Test Items	33
23	Correlation Between PV and Fatigue Life	34
24	Fracture Energies, Flexibility Indices of SCB, and Fracture Energies of DCT Specimens Consisting of PG 64-22 Mix Used in CC9 Overload Test Items	35
25	Carriage Positions for Each Pass of Proof-Roll Wander	39
26	Heavy Weight Deflectometer and PSPA Test Locations in Overload Test Items	42
27	Construction Cycle 9 Traffic Wander Wheel Tracks	45
28	Evolution of Surface Upheaval in Overload Test Items	50
29	Rut Accumulation in the Overload Test Items Measured with Straightedge	51
30	Variation of Crack Densities with Traffic in Test Items LFC-5N and LFC-5S	52
31	Cracking Densities in Overload Test Item LFC-5N at 18,480 Passes	53
32	Cracking Densities in Control Test Item LFC-5S at 18,480 Passes	54
33	Peak Transverse Tensile Strain Response by Direction of Traffic	56
34	Variation of Peak Longitudinal Tensile Strain in Test Item LFC-5N with Pass Number and Asphalt Temperature	57
35	Variation of Peak Longitudinal Tensile Strain in Test Item LFC-5S with Pass Number and Asphalt Temperature	58
36	Variation of Peak Transverse Tensile Strain in Test Item LFC-5N with Pass Number and Asphalt Temperature	59
37	Variation of Peak Transverse Tensile Strain in Test Item LFC-5S with Pass Number and Asphalt Temperature	60
38	Variation of Asphalt Concrete Temperature with Pass Number for Test Item LFC-5N	61
39	Peak Vertical Compressive Stress at top of P-154 Subbase	62
40	Peak Vertical Compressive Stress at top of Clay Subgrade	63

41	Permanent Deformation of Subgrade from CS Data	64
42	Peak Compressive Strain at Top of Clay Subgrade from CS Pairs	65
43	Gravimetric Moisture Content in Clay Subgrade	66
44	Change in AUPP Ratios	68
45	Backcalculated Modulus Values of P-401MR Asphalt Concrete, P-209MR Base Course, P-154 Granular Subbase, and P-152MR Clay Subgrade	69
46	Longitudinal Profiles	71
47	Transverse Profiles, STA 2+55	72
48	Compressive Strains Recorded at the Top of Subgrade During the Ramp-Up Response Test in Overload Test Item LFC-5N	75
49	Variability in Peak Asphalt Strain Readings Following First Overload Event	76
50	Signal Normalization Process Using CS Data and an Illustration of its Physical Interpretation	78
51	Critical Responses During CC9 Trafficking for CS and PC	79
52	Environmental Responses During CC9 Trafficking for MS and LFC-5N Thermocouples	80
53	Gravimetric Moisture Content w Versus Time	81
54	Top-of-Subgrade Average Deflection Versus w	82
55	Top-of-Subgrade Average Deflection Versus Δw	83
56	Change in Computed Subgrade Modulus During Traffic	83
57	Overload Aircraft Gear Load Simulations Using FAARFIELD and ABAQUS	87

LIST OF TABLES

Table		Page
1	P-401MR Aggregate Gradation	7
2	Properties and Assumptions for the Determination of LWD Modulus	8
3	Summary of In-Place Characterization of Clay Subgrade	8
4	Summary of In-Place Characterization of Granular Subbase	13
5	Summary of In-Place Characterization of Base-Course Materials	16
6	Summary of In-Place Characterization of P-401 AC Layer	19
7	Summary of Subgrade Resilient Modulus	24
8	High-Temperature Indirect Tensile Strength S Test Results for PG 64-22 Mixture Used in CC9 Overload Test Items	31
9	Summary of ACR/PCR Data for CC9 Overload Test Items	37
10	Carriage Positions for Each Pass of Proof-Roll Wander	38
11	Construction Cycle 9 Traffic Wander Wheel Track Locations	44
12	Construction Cycle 9 Complete Wander Sequence	46
13	Construction Cycle 9 Traffic Summary	47
14	Ground-Penetrating Radar Datasets Analyzed for the CC9 Overload Test	70
15	Estimated Thickness of Asphalt Layer	73
16	Estimated Thickness of Base Layer	73
17	Critical Gear Loads on CC7 and CC9	86
18	Maximum Shear Stress and SSR for CC7 and CC9 Overload Test Items	88
19	Maximum Allowable Overload for CC7 and CC9 Test Items Using SSR = 0.75	89

LIST OF SYMBOLS AND ACRONYMS

ε-mu	Strain measuring unit
Δw	Change in gravimetric moisture content
μ	Mean
σ	Standard deviation
M_R	Resilient modulus
w	Gravimetric moisture content
2D	Two duals in tandem (four-wheel)
3D	Three duals in tandem (six-wheel)
3-D	Three-dimensional
AC	Asphalt concrete
ACR	Aircraft Classification Rating
APA	Asphalt pavement analyzer
ASTM	American Society for Testing Materials
ASG	Asphalt strain gauge
AUPP	Area under pavement profile
BDF	Bridge deck finisher
CBR	California bearing ratio
CC	Construction cycle
CC7	Construction cycle 7
CC9	Construction cycle 9
CD	Crack density
CDF	Cumulative damage factor
CH	High-plasticity clay
COV	Coefficient of variation
CS	Coil sensor
D	Dual (two-wheel)
DBP	Deflection-based parameter
DCT	Disk-shape compact tension
D-PSPA	Portable seismic pavement analyzer for unbound layers
FE	Finite element
FEA	Finite element analysis
FAA	Federal Aviation Administration
FAA AC	FAA Advisory Circular
FAARFIELD	FAA Rigid and Flexible Iterative Elastic Layered Design
FI	Flexibility index
FN	Flow number
GPR	Ground-penetrating radar
HMA	Hot mix asphalt
HWD	Heavy weight deflectometer
HTITS	High-temperature indirect tensile strength
ICAO	International Civil Aviation Organization
IDT	Indirect tensile
ksi	Kilopounds per square inch
LEA	Layered elastic analysis
LEAF	Layered Elastic Analysis—FAA (computer program)

LiDAR	Light Detection and Ranging
LSG	Longitudinal strain gauge
L/T	Longitudinal/transverse
LWD	Light weight deflectometer
MC	Moisture content (volumetric)
MEPDG	Mechanistic-Empirical Pavement Design Guide
MH	High-plasticity silt
MnDOT	Minnesota Department of Transportation
MS	Moisture sensor
MTV	Material transfer vehicle
NAPMRC	National Airport Pavement and Materials Research Center
NAPTF	National Airport Pavement Test Facility
NAPTV	National Airport Pavement Test Vehicle
NDT	Nondestructive testing
PC	Pressure cell
PCI	Pavement condition index
PCR	Pavement Classification Rating
pcf	Pounds per cubic foot
PV	Plateau value
PSPA	Portable seismic pavement analyzer
QA/QC	Quality assurance/quality control
QS	Quick shear
RDEC	Ratio of dissipated energy change
S	Single (one-wheel)
SCB	Semi-circular bend
SSR	Shear stress ratio
STA	Station
TSG	Transverse strain gauge
UCS	Unconfined compressive strength
UU	Unconsolidated-undrained
VUC	Virtual upheaval calculator

EXECUTIVE SUMMARY

From 2020 to 2024, the Federal Aviation Administration (FAA) executed a series of full-scale traffic tests on flexible airport pavements at the National Airport Pavement Test Facility (NAPTF), designated Construction Cycle 9 (CC9). Within CC9, the Flexible Pavement Overload Test was designed to support development of International Civil Aviation Organization (ICAO) standards for occasional overload operations, as provided for in ICAO Annex 14, Volume I. Current Annex 14 guidance stipulates that occasional overload aircraft traffic should not have an Aircraft Classification Rating (ACR) exceeding 10% above the reported Pavement Classification Rating (PCR). The acceptable number of annual overload operations is further limited to less than 5% of the total annual aircraft traffic (exclusive of light aircraft). Based on previous NAPTF tests in Construction Cycle 7 (CC7), it is believed that these criteria are unduly conservative.

As a follow-up to the CC7 overload tests, the FAA constructed two full-scale flexible test items during CC9. The main purpose of the test was to determine, if possible, the threshold level of vertical subgrade strain corresponding to a permanently damaging overload condition (i.e., an overload that should not be exceeded). The paired test items with identical layered structures were subjected to different traffic conditions. Both test items received identical regular traffic from the design load, a dual (D) gear loaded to 36,000 pounds per wheel (representing an ACR-to-PCR ratio of 1.0). The north test item was heavily overloaded on three occasions, with ACR exceeding PCR by 75%, while the south test item received no overloads and acted as the control. Both test items were instrumented with asphalt strain gauges, pressure cells, and coil sensor pairs at the top of the subgrade layer to record vertical strain. In addition to monitoring sensor responses, the performance of the test items was monitored by periodic rut measurements, visual surveys, nondestructive testing (NDT), and periodic surface scans using a high-resolution laser scanner. The influence of seasonal variability was considered using asphalt temperature and subgrade moisture data.

The applied overload substantially exceeded the ICAO-recommended 10% limit. Despite this, the repeated heavy overloads did not significantly reduce pavement structural life. Both test items (overload and control) failed in a surface cracking mode prior to shear failure in the subgrade. The FAA computer program, FAA Rigid and Flexible Iterative Elastic Layered Design (FAARFIELD), which relies on a layered elastic analysis to compute PCR, substantially underpredicted vertical compressive strain in the subgrade in comparison to the strains measured with coil sensors. For this reason, it may not be feasible to define a limiting strain criterion for overload guidance within the current design framework. Seasonal variation in temperature, moisture mobilization due to thermal gradients, and fatigue-induced reductions in structural capacity significantly influenced the measured critical pavement responses. Based on an analysis of the CC7 and CC9 data, the authors propose an alternative overload criterion that considers the subgrade stress ratio (SSR) as an indicator of damage. The SSR criterion is feasible for clay subgrades but requires laboratory determination of the subgrade shear strength as an additional parameter.

1. INTRODUCTION

1.1 BACKGROUND

The Federal Aviation Administration (FAA) conducted a previous overload traffic test in 2014–2016 as part of National Airport Pavement Test Facility (NAPTF) Construction Cycle 7 (CC7), to evaluate the International Civil Aviation Organization's (ICAO) existing criteria for allowable occasional aircraft overloads on flexible airport pavements (ICAO, 2020). The CC7 test identified limiting subgrade vertical strain as a possible criterion. The Construction Cycle 9 (CC9) overload test fulfills a need to generate data to support the development of a possible strain criterion for allowable overloads of flexible airport pavements.

1.2 OBJECTIVE AND SCOPE

The objective of the CC9 Overload Test was to determine the effect on pavement life of short-term aircraft overloads exceeding the ICAO Annex 14 limit (currently 10% above published Pavement Classification Rating [PCR]).

1.3 NATIONAL AIRPORT PAVEMENT TEST FACILITY TERMINOLOGY

1.3.1 Test Terminology

The following terms and phrases are commonly used at the NAPTF:

Construction Cycle (CC). CC refers to the overall test project including design, construction, traffic testing, post-traffic testing, data collection, data analysis, and final demolition. Each CC is developed with specific test objectives in mind. Typically, a CC is dedicated to either rigid or flexible pavement testing.

Test Area. Each CC is divided into multiple test areas as required by the test objectives. Dividing the test pavement into test areas allows the FAA to conduct multiple experiments simultaneously. A test area can be made up of one or more test items.

Transition Area. Transition areas separate the test items in the longitudinal direction, avoiding abrupt changes in layer thickness at test item boundaries. Transition areas are of sufficient length to allow vehicle startup and shutdown while maintaining a constant speed and load over the test items themselves.

Test Item. A test item is a unit of pavement within the test area characterized by a unique combination of pavement structure and test traffic. For CC9, each test area was divided into two test items, designated north and south, on the corresponding sides of the facility centerline. Each test item is designated by an identifier consisting of three letters, followed by a dash and two additional characters.

- The first letter corresponds to the strength of the subgrade (L = Low strength, M = Medium strength, H = High strength).

- The second letter corresponds to the type of pavement structure (F = Flexible, R = Rigid).

- The third letter corresponds to the type of base (S = Stabilized, C = Conventional/unstabilized, G = Slab-on-grade/no base).

- The last two characters give the sequential numbering of the test item, and whether it is on the north (N) or south (S) side of the centerline.

For example, in this report, the designation LFC-5N refers to the north test item of Test Area 5 that is built on a low-strength subgrade (L), using a flexible (F) pavement, with an aggregate (i.e., conventional, C) base course. Test items are numbered from west to east.

Wander Pattern. The National Airport Pavement Test Vehicle (NAPTV) executes a wander pattern consisting of a repeated sequence of 66 passes arranged in 9 longitudinal tracks. The lateral spacing between adjacent tracks is 10.25 in. The NAPTF wander pattern is designed to approximate a normal lateral distribution of aircraft traffic with a standard deviation from centerline equal to 30.54 in.

1.3.2 Work Item Modifiers

In general, NAPTF test items follow the material and construction standards in FAA Advisory Circular 150/5370-10H, *Standard Specifications for Construction of Airports* (FAA, 2018). However, research objectives may require deviation from some aspects of the standard. To indicate that the construction specification is altered, work items are modified with the following designations: M = Modified, R = Research, MR = Modified Research. Material items listed below are modified from the standard FAA specifications.

- P-152MR Subgrade: Work Item P-152MR is a prepared subgrade composed of soil that provides the specified design California bearing ratio (CBR) values for test items constructed on low strength subgrades. The subgrade material is prepared in the excavated bed of the NAPTF or the FAA Subgrade Processing building in accordance with the project specifications.

- P-209MR Crushed Aggregate Base Course: Work Item P-209MR is a base course composed of crushed aggregate.

- P-401MR Asphalt Mix Pavement Surface Course: Work Item P-401MR is a hot mix asphalt (HMA) pavement course composed of mineral aggregate and asphalt binder mixed in a central mixing plant, placed on a prepared base or stabilized course, and compacted. It can be used for multiple pavement courses but is typically used as a surface course.

2. DESIGN AND CONSTRUCTION OF TEST AREAS

CC9 was built on the west end of the NAPTF building. All test areas were built on clay subgrade with a nominal CBR of 5 (hence low strength, L). Figure 1(a) shows the CC9 test area inside NAPTF, located in the FAA William J. Hughes Technical Center for Advanced Aerospace at Atlantic City International Airport, NJ. The hatched rectangle highlighted with green in Figure 1(b) shows the CC9 overload test area. The CC9 test pavement within the NAPTF is 320 feet long and

60 feet wide and extends from stations (STAs) 0-20 to 3+00. There is a 3-foot-wide shoulder on both sides of the test pavement.

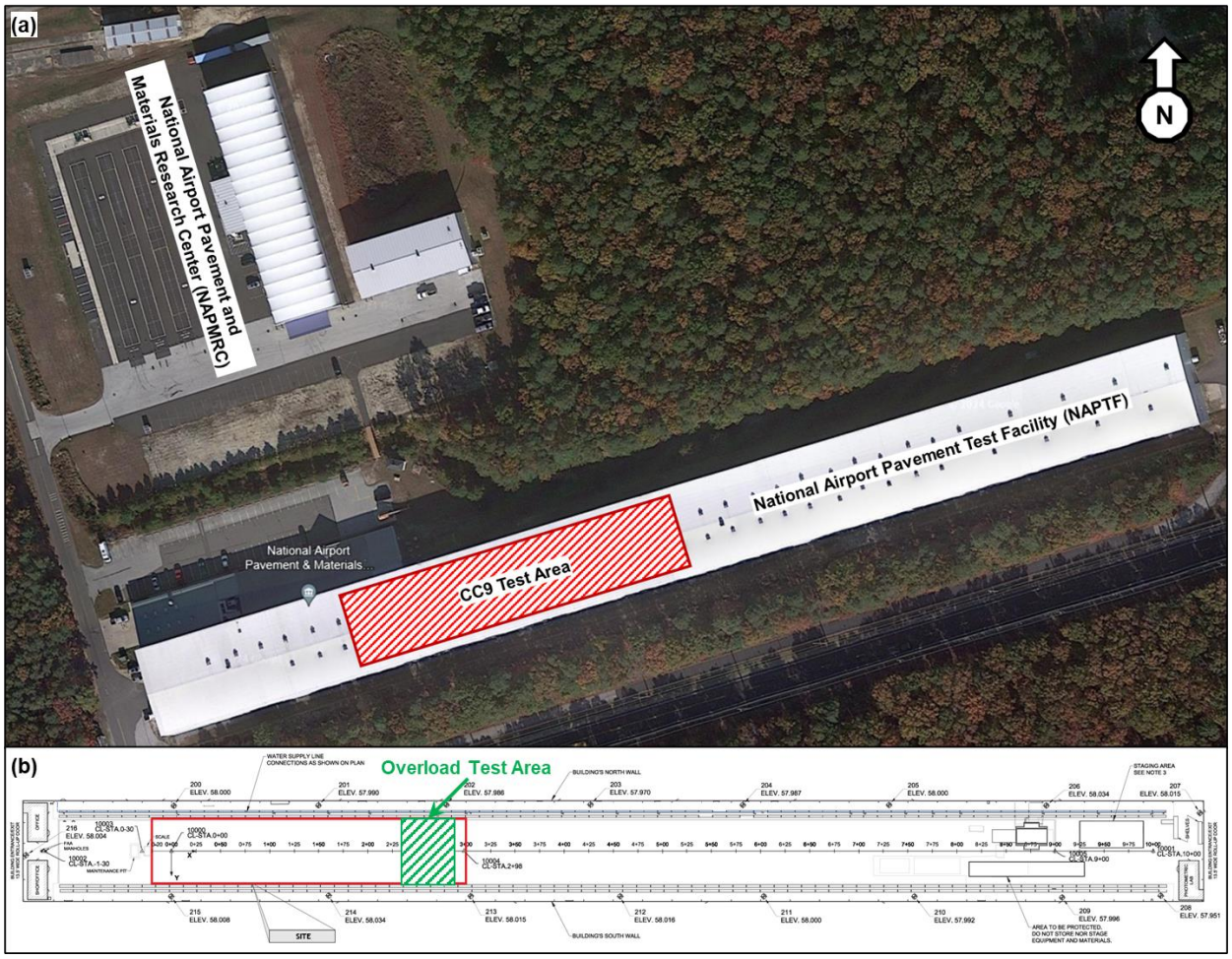

Figure 1. Satellite Image of (a) the CC9 Test Area and (b) the CC9 Overload Test Area

Figure 2 shows the test area plan for CC9. The designated test areas are organized into ten test items, five north and five south of the centerline. Each test item is 45 ft long and 30 ft wide. The two test items assigned to the overload test area are LFC-5N and LFC-5S (STAs 2+40 to 2+85). The structural design for the CC9 overload test area was intended to replicate the CC7 overload test items, which had nominally 3-in. P-401 asphalt surface, 6-in. P-209 crushed aggregate base, and 20-in. P-154 subbase consisting of compacted manufactured screenings, on a CBR 5 clay subgrade. Figure 3 shows the as-built layer structure. While the two test items are nominally identical in cross section, they were subjected to different traffic loads.

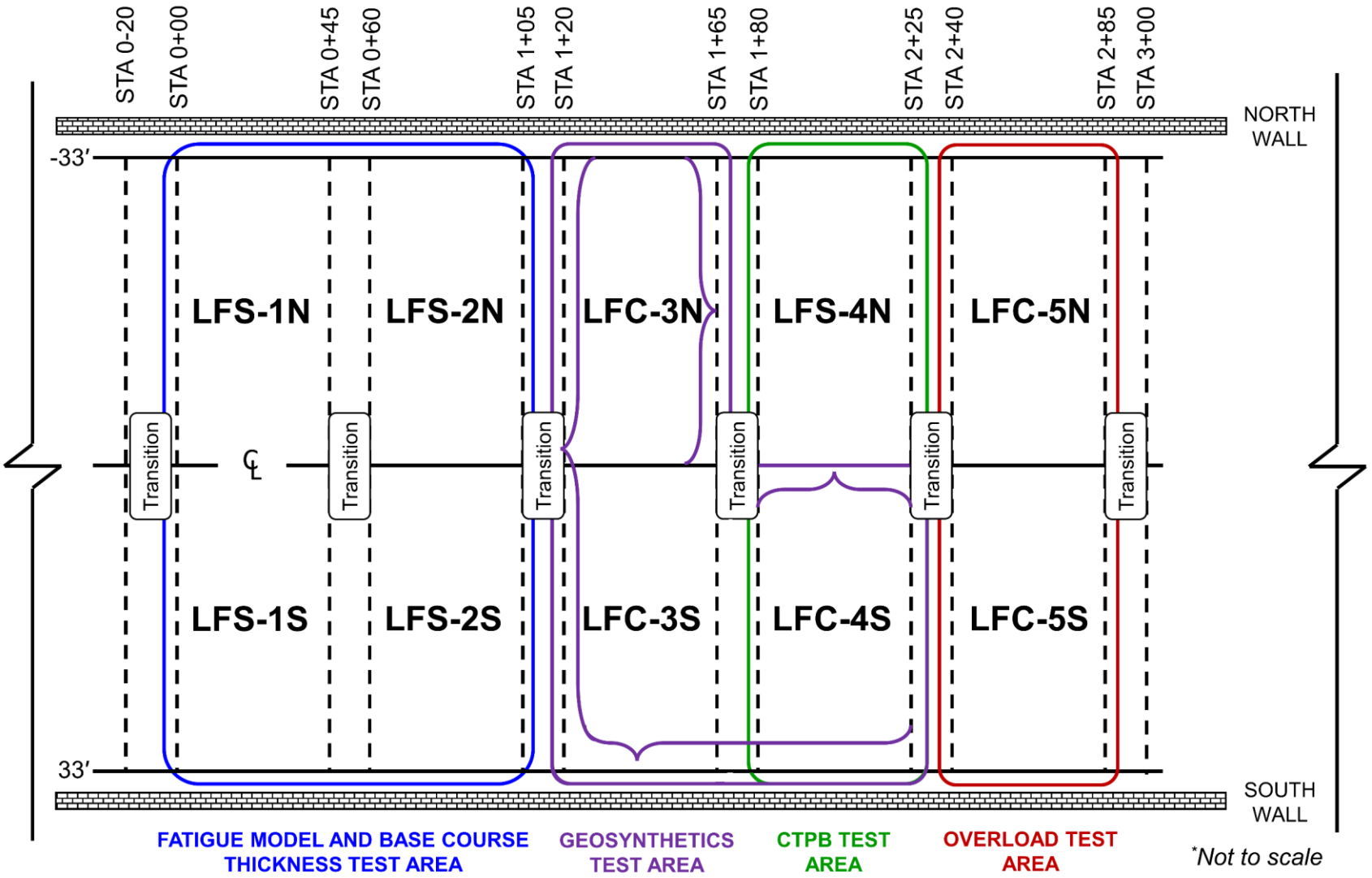

Figure 2. Plan View of the CC9 Test Areas and Items

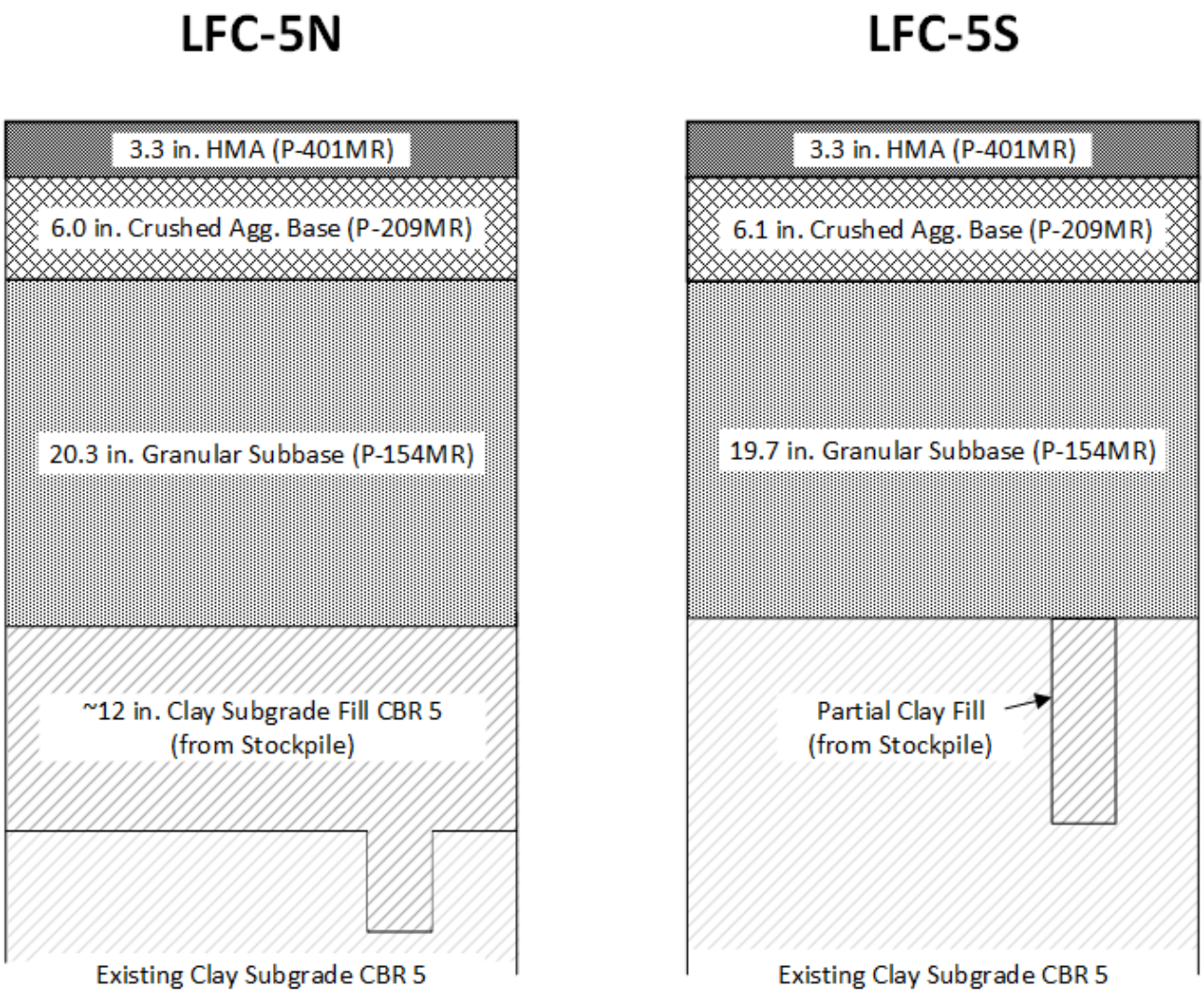

Figure 3. As-Built Cross-Sections of Overload Test Items

2.1 REVIEW OF CONSTRUCTION QUALITY CONTROL AND ASSURANCE

2.1.1 Placement and Compaction of Subgrade (P-152MR)

The existing CC9 subgrade (P-152MR) consisted of two clay materials. The upper subgrade is Dupont Clay, classified by the Unified Soil Classification system as a high-plasticity clay (CH) with a plastic limit of 19 and liquid limit of 56. Approximately 5 feet below the surface of Dupont clay is County Sand and Stone clay originally placed during CC1 construction. County Sand and Stone clay may be classified as either high-plasticity silts (MH) or CH per the original NAPTF pavement design report (Hall, 1998). Both materials were sourced from the Delaware Bay area, approximately 40 miles west of the NAPTF. For CC9, subgrade areas north of the centerline were in fill, and areas south of the centerline were in cut. (This was a result of the profile remaining from CC7, where test items on the north were thicker than those on the south.) As shown in Figure 3, test item LFC-5N was backfilled with approximately 12 in. of stockpiled Dupont clay, while test item LFC-5S received only a partial fill and recompaction. Subgrade was rolled with a steel drum roller followed

by a rubber tire roller, after which the subgrade was recompacted with a steel drum roller to ensure a smooth surface. The steel drum roller was used to provide a smooth surface for CBR testing, and the rubber tire roller was used to remove air from the clay. Based on previous experience at the NAPTF, the rubber tire roller adequately consolidates the clay and stitches sequential lifts together. The clay was processed (tilled, spread, shifted, or recompacted) in situ to the target CBR of 5 to meet the required grade. More details of the subgrade placement can be found in the CC9 Construction Report (Tomlinson et al., 2022).

2.1.2 Placement and Compaction of Subbase Course (P-154MR)

The subbase was a carbonate-based manufactured sand placed in lifts ranging from 5–10 in. for all layers. After delivery by truck, each lift was leveled using a bulldozer, followed by vibratory compaction with steel drum rollers. The edges of the test items were compacted with a plate tamper. The granular subbase was rolled over until no further densification was observed, starting with the first lift above the finished subgrade. ("No further densification" was defined as the mean density for all tests performed within a test item that did not change by more than 0.5% in successive readings after a minimum of three passes with the roller.) Compaction was performed in both longitudinal and transverse directions throughout the test items. A nuclear density gauge was used to determine density and moisture content (MC). Measurements were made at two random locations in each test item, and the average of those values had to meet or exceed the target dry density of 138.3 pounds per cubic foot (pcf), with a MC between 2% and 6%. In establishing these criteria, the target density corresponded to the maximum density on the modified Proctor curve at 6% MC. A maximum of 6% MC was chosen since that was the highest value for which no drain-down was observed during laboratory testing. To elevate the MC (up to 6%) when the target density could not be achieved at lower MC, water was added using a bridge deck finisher (BDF) fitted with a spray bar, and riding on the NAPTF rails. This procedure allowed each successive lift to be compacted to the required density.

2.1.3 Placement and Compaction of Base Course (P-209MR)

The base layer material was a blend of three diabase granular materials sourced from Birdsboro Quarry in Skippack, PA. The base was placed in lifts of 4–8 in. Steel drum rollers were used to compact each lift. A nuclear density gauge was used to determine density and MC. Two random locations were selected in each test item for acceptance testing, and the average of those values was required to meet or exceed the target dry density of 151.3 pcf, with a MC between 1.5% and 5.5%. The target density corresponded to the maximum density on the modified proctor curve. A maximum of 5.5% MC was chosen because that was the highest value where no drain-down was observed during laboratory testing.

2.1.4 Placement and Compaction of Asphalt Concrete (P-401MR)

The asphalt layer was constructed using an asphalt mixture conforming to the P-401MR specification (Tomlinson et al., 2022). The mixture had a nominal maximum aggregate size of 0.75 in. The full gradation is provided in Table 1. The surface layers of the overload test items were paved with an unmodified (neat binder) PG 64-22 asphalt concrete (AC) mix. The binder performance grade was selected to maintain consistency with the CC7 overload test items.

Table 1. P-401MR Aggregate Gradation (for both asphalt mixtures)

Sieve Designation	Contractor-Provided Percent Passing, %	Percent Passing Band, %
1 in. (25 mm)	100.0	100
3/4 in. (19 mm)	97.1	90–100
1/2 in. (12.5 mm)	84.0	68–88
3/8 in. (9.5 mm)	74.4	60–82
No. 4 (4.75 mm)	52.0	45–67
No. 8 (2.38 mm)	36.0	32–54
No. 16 (1.19 mm)	25.2	22–44
No. 30 (600 µm)	17.8	15–35
No. 50 (300 µm)	11.4	9–25
No. 100 (150 µm)	7.2	6–18
No. 200 (75 µm)	4.0	3–6

Asphalt was placed in the overload test area on December 11, 2019. The finished surfaces of the compacted P-209 layer in the overload test items were tacked with PG 64-22 asphalt binder prior to paving. A stringline was set on vertical rods spaced every 20 feet to maintain the designed grade while paving. A material transfer vehicle (MTV) was placed in front of the paver. Production mixes were continuously fed into the paver through the MTV as the placement and compaction proceeded from east to west. The paver had sonic grade-control for use with the stringline system. AC thickness was assessed with surveyor's rulers and calibrated depth gauges. Rollers were used in static mode to compact the center of the pass before switching to vibratory mode. Then two vibratory rollers were used in tandem until the achieved densities met the target according to nuclear gauge tests. Lastly, both rollers were operated in static mode, rolling out any ripples in the mat.

The contractor had difficulty achieving the target grade. The finished grade was higher than the target between stations 2+40 and 2+55. The overshot at the start of the test area was attributed to the limited ramp/takeoff distance available to elevate the paver to the target grade. Because the high grade was symmetrical in both test items, and to avoid the loss and replacement of embedded instrumentation which repaving would have entailed, no corrective measure was taken.

2.2 IN-PLACE TESTING FOR CONSTRUCTION UNIFORMITY

This section discusses characterization of both unbound and bound layers. Characterization tests for unbound layers included stiffness from light weight deflectometer (LWD), GeoGauge, and portable seismic pavement analyzer for unbound layers (D-PSPA). For asphalt, test results included mat and joint densities and air voids, and seismic moduli from the portable seismic pavement analyzer (PSPA).

LWD modulus values were determined from Boussinesq's half-space equation (Mooney and Miller, 2009). The stress distribution factors listed in Table 2. are those recommended by Bilodeau and Doré (2014), assuming Poisson's ratios and LWD plate radii are as listed in Table 2.

$$E = \frac{f \times (1-\nu^2) \times \sigma_0 \times a}{d_0} \quad (1)$$

where:

E = LWD modulus,
f = stress distribution factor,
ν = Poisson's ratio,
σ_0 = contact stress,
a = plate radius, and
d_0 = center deflection.

Table 2. Properties and Assumptions for the Determination of LWD Modulus

Layer	Poisson's Ratio	Stress Distribution Factor	Plate Radius (in.)
Subgrade	0.4	4/3	5.9
Granular subbase	0.35	8/3	5.9
Crushed aggregate base	0.35	8/3	3.0

2.2.1 Subgrade (P-152MR)

Table 3 lists seven material properties tested on the subgrade. Comparing the two test items, moisture content and density were nearly equal. However, average shear strength and subgrade modulus were consistently higher for LFC-5N than for LFC-5S. The discrepancy in moisture-density measurements between the stockpile and in situ clayey subgrade (Section 2.1.1) could have contributed to the difference.

Table 3. Summary of In-Place Characterization of Clay Subgrade

Test Item	LFC-5N			LFC-5S		
Properties	**μ**	**σ**	**COV (%)**	**μ**	**σ**	**COV (%)**
CBR (%)	5.5	0.2	3.8	5.2	0.3	5.8
MC (%)	24.2	N/A	N/A	24	N/A	N/A
In situ dry density (pcf)	100.1	N/A	N/A	99.8	N/A	N/A
Shear strength (psi)	14.8	1.6	10.6	12.3	1	8
LWD modulus (ksi)	8.9	3.0	33.3	4.9	2.5	50.4
Seismic modulus (ksi)	20.6	1.7	8	17.2	2.1	12.4
GeoGauge modulus (ksi)	15.8	2.6	16.8	14.3	3	21.1

μ = Mean, σ = Standard deviation, COV = Coefficient of variation.

Figure 4 shows the stations and offsets where CBR tests were performed. There were only small differences in CBR between the test items. All CBR tests were conducted in traffic areas. Figure 5 plots the results of the Vane shear test against the transverse offset. As shown in Figure 5, LFC-5S generally had lower vane shear strength than LFC-5N.

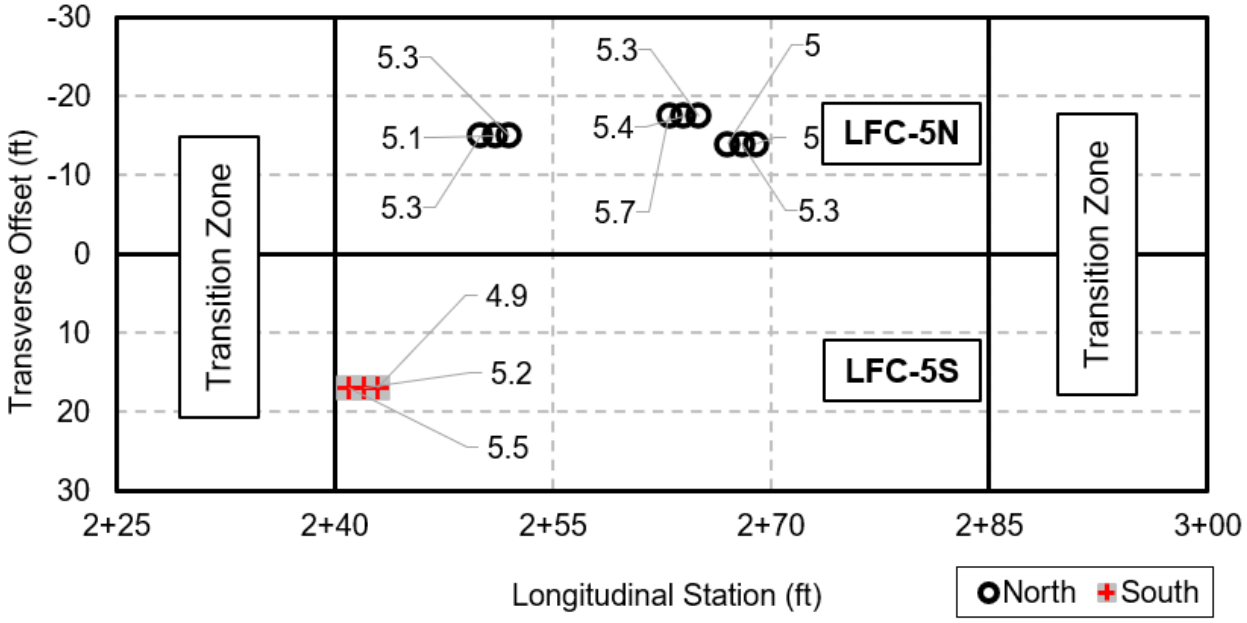

Figure 4. Construction Cycle 9 Subgrade CBR Test Locations

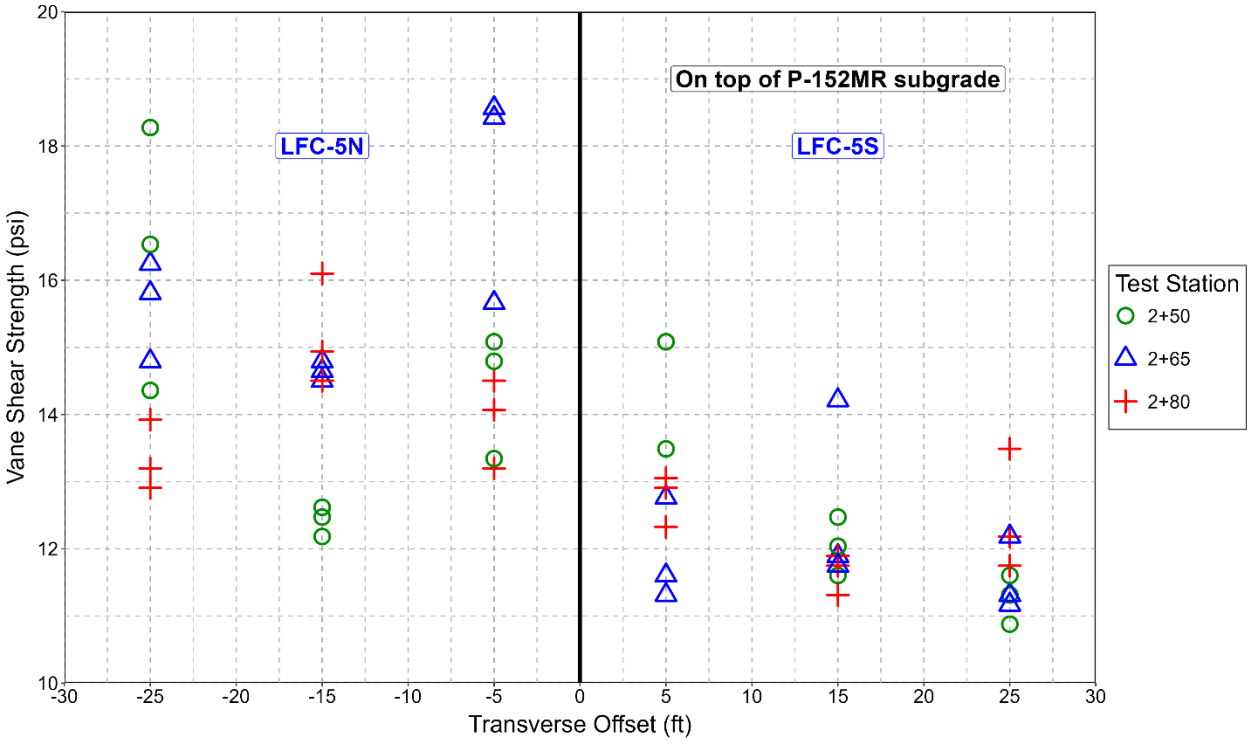

Figure 5. As-Built Subgrade Shear Strength in Overload Test Items Measured with Vane Shear Tests

Modulus values varied considerably depending on the device used to measure them. As a general point of reference, consider the widely used conversion formula $E = 1500 \times CBR$. That is, based on the nominal CBR 5, expect approximately $E = 7.5$ kilopounds per square in. (ksi).

2.2.1.1 Light Weight Deflectometer Modulus

The LWD tests in LFC-5S exhibited mean modulus values lower than the above conversion formula on the south, but higher on the north. Figure 6(a) and (b) plot LWD modulus against the LWD plate contact stress for test items LFC-5N and LFC-5S, respectively. LWD modulus values for LFC-5N were generally higher than those for LFC-5S. The LWD moduli decreased with increasing contact stress, showing stress-softening behavior characteristic of fine-grained soil.

2.2.1.2 Seismic Modulus

Seismic moduli of the subgrade layers were measured using D-PSPA device (Nazarian et al., 1993). Figure 7(a) and (b) show D-PSPA moduli measured parallel and perpendicular to the direction of traffic. Like the LWD case, LFC-5N exhibited higher seismic moduli than LFC-5S in both directions. Seismic devices such as D-PSPA operate at very low strain; therefore, the measured seismic modulus is typically several times higher than the modulus from a falling weight device, as shown in Figure 6. Similarly, the seismic modulus must be corrected to compare it to the modulus converted from CBR.

2.2.1.3 GeoGauge Modulus:

Figure 8 plots the GeoGauge moduli against the lateral offset. The highest GeoGauge moduli in both test items were found at an offset of 25 ft (outside the trafficked area). Modulus values did not exhibit any consistent trend except that, regardless of the device, LFC-5N exhibited higher values on average compared to LFC-5S.

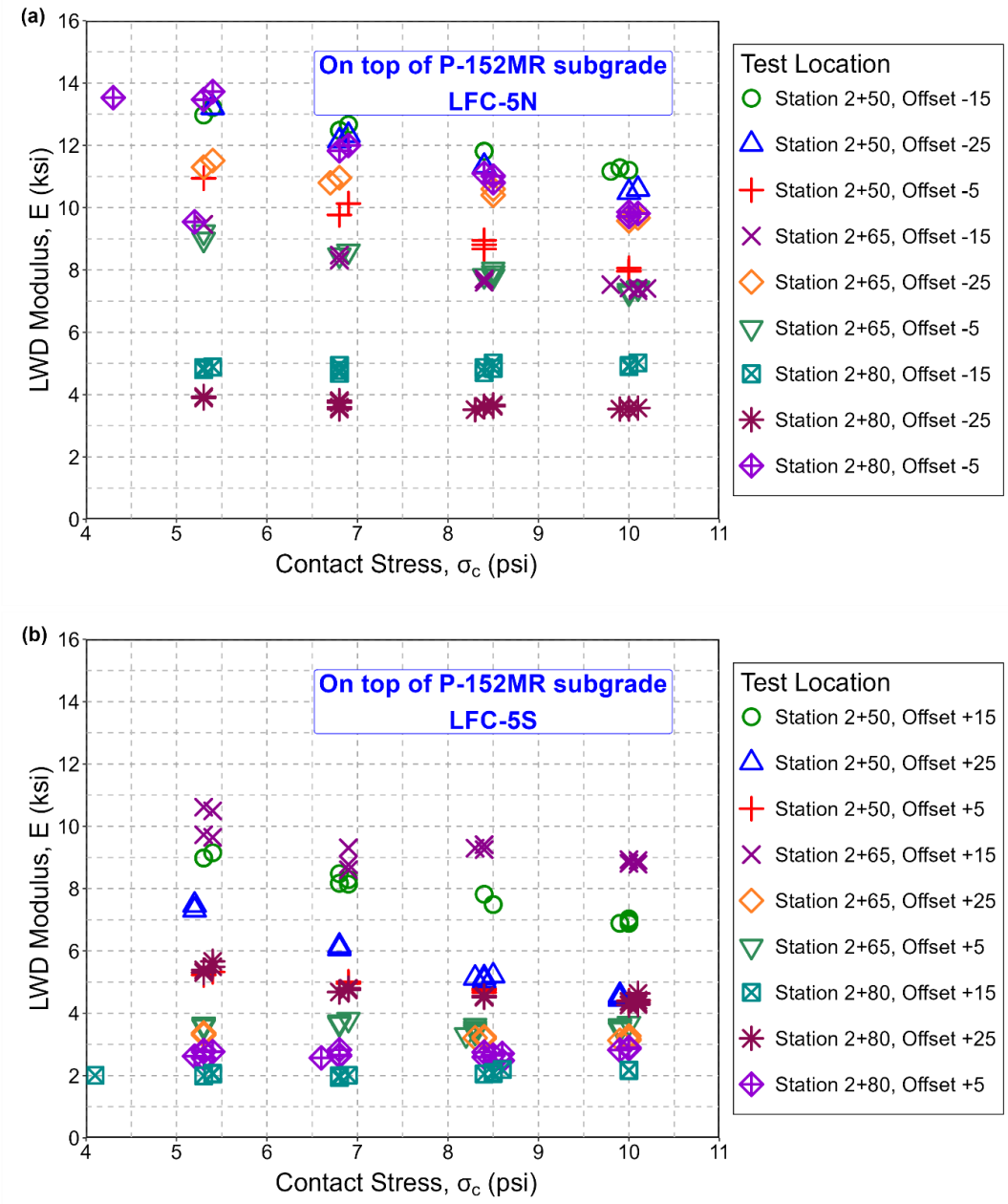

Figure 6. As-Built Subgrade Modulus in Overload Test Items Measured with LWD

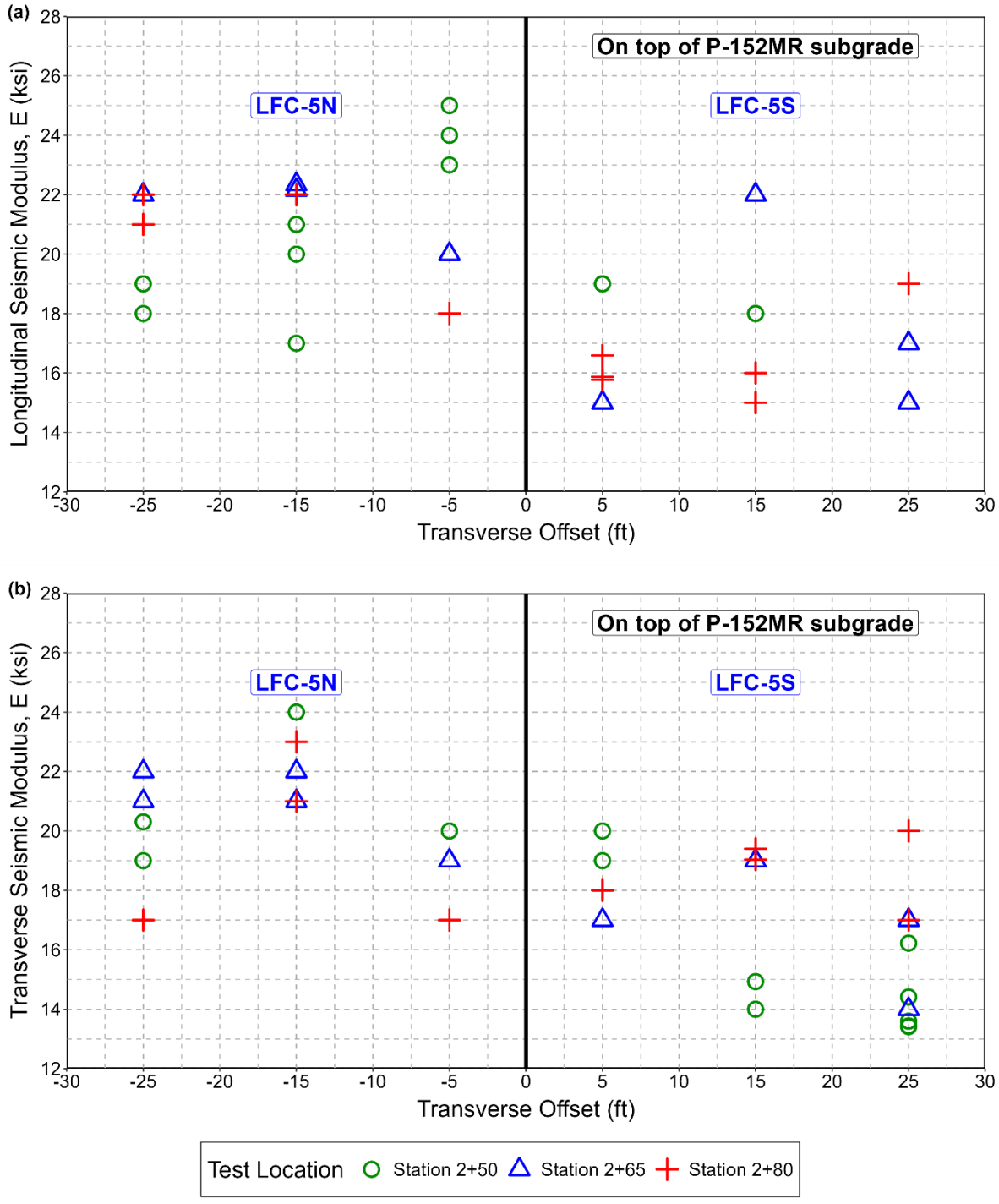

Figure 7. As-Built Subgrade Seismic Modulus in Overload Test Items Measured with D-PSPA

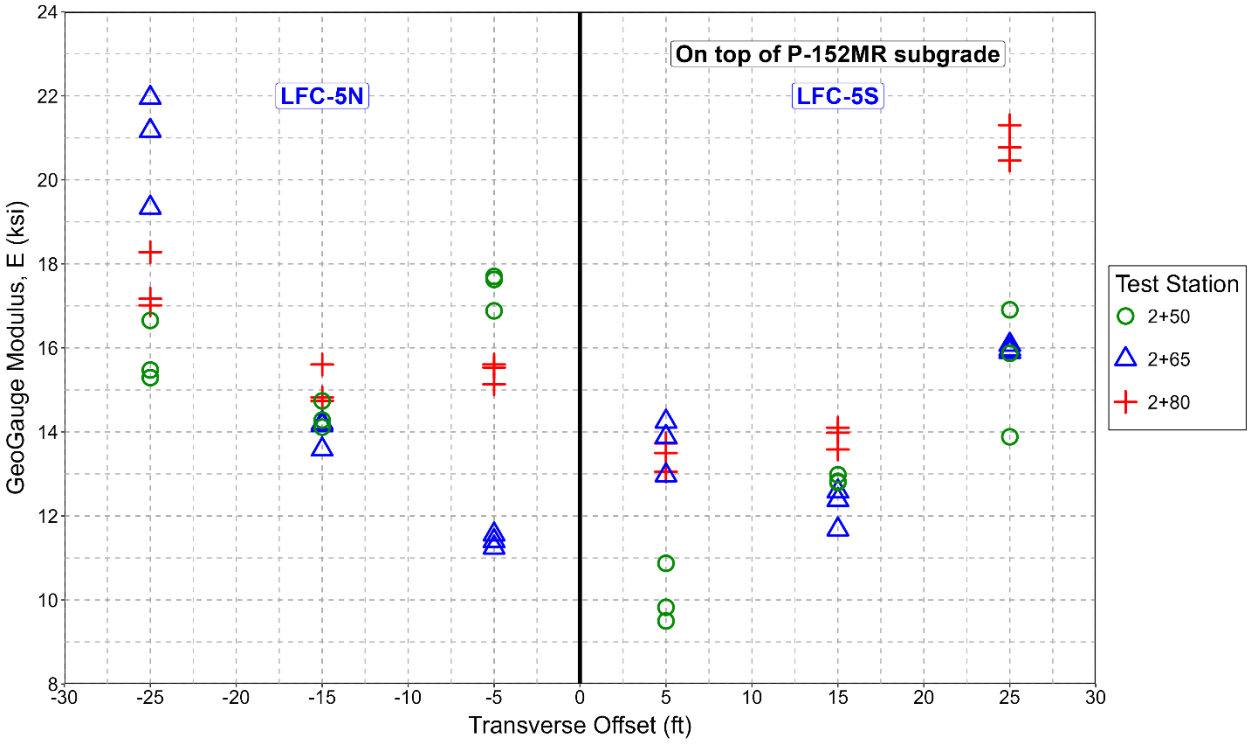

Figure 8. As-Built Subgrade Modulus in Overload Test Items Measured with GeoGauge

2.2.2 Subbase Course (P-154MR)

Table 4 lists summary statistics for five material properties measured on the granular subbase. Seismic modulus values measured with the D-PSPA device were on average about four times higher than moduli from LWD and GeoGauge. However, regardless of the testing method, the average modulus measured at the top of subbase was similar for both test items.

Table 4. Summary of In-Place Characterization of Granular Subbase

Test Item	**LFC-5N**			**LFC-5S**		
Properties	**μ**	**σ**	**COV (%)**	**μ**	**σ**	**COV (%)**
Nuclear gauge density (pcf)	141.5	N/A	N/A	138.8	N/A	N/A
Nuclear gauge MC (%)	3.7	N/A	N/A	4.4	N/A	N/A
LWD modulus (ksi)	17.3	3.3	19.3	15.7	2.4	15.3
Seismic modulus (ksi)	66.6	13.6	20.4	62.5	9	14.4
GeoGauge modulus (ksi)	15.1	1.8	11.9	16	1.2	7.6

μ = Mean, σ = Standard deviation, COV = Coefficient of variation

Figure 9 plots the LWD modulus at top of subbase against the corresponding LWD plate contact stresses. The subbase layers of LFC-5N show the stress-hardening behavior expected in aggregate materials, as LWD modulus increases with increasing stress. By contrast, LFC-5S did not show evidence of stress hardening in these results. In general, modulus variation with respect to contact

stresses, transverse offset, and longitudinal position were all higher in LFC-5S compared to LFC-5N.

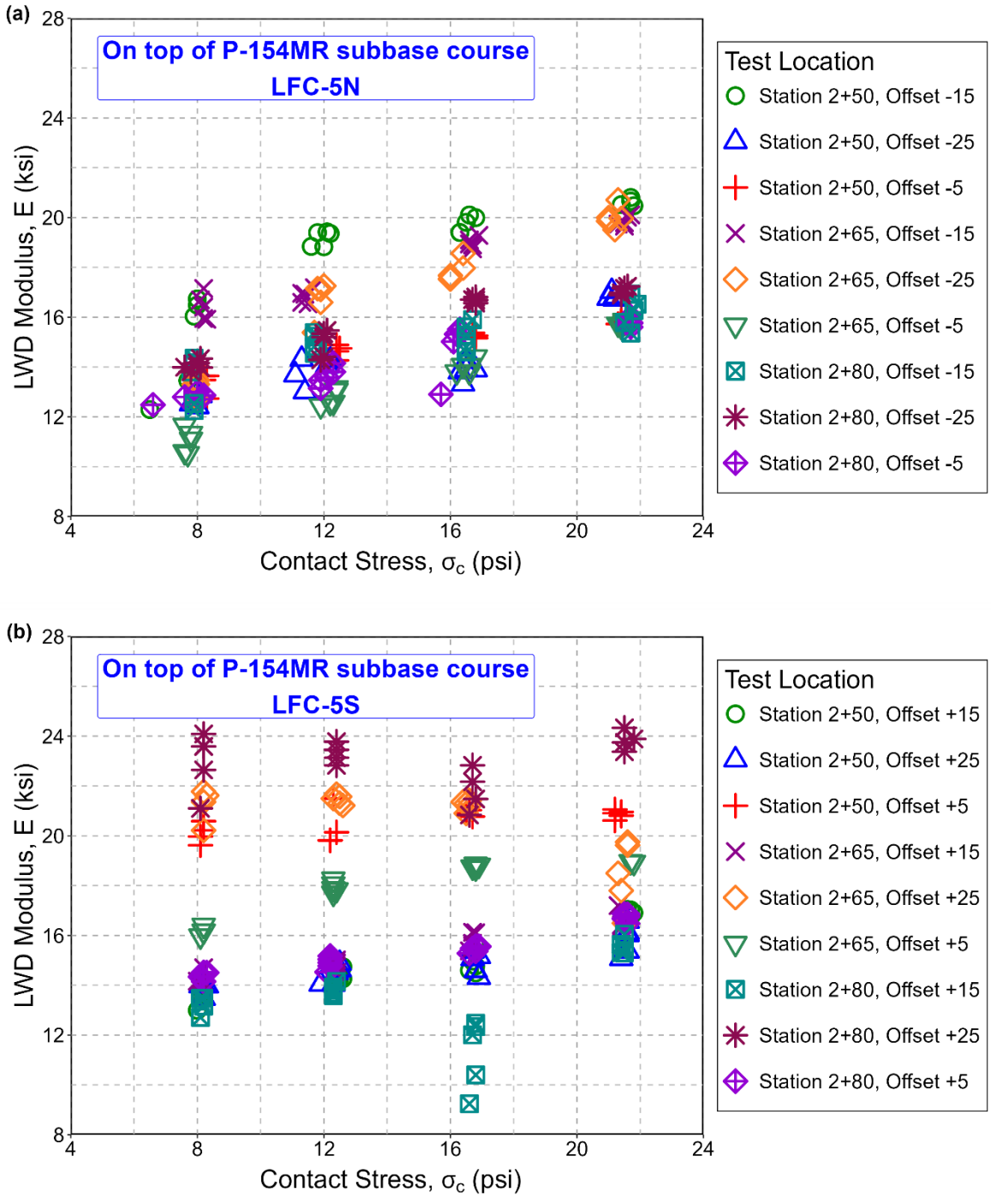

Figure 9. As-Built Subbase Modulus in Overload Test Items Measured with LWD

Figure 10 plots top-of-subbase seismic moduli (D-PSPA) measured in the longitudinal and transverse directions against the transverse offset for LFC-5N and LFC-5S. The difference in modulus based on the direction of measurement directions might indicate anisotropic behavior.

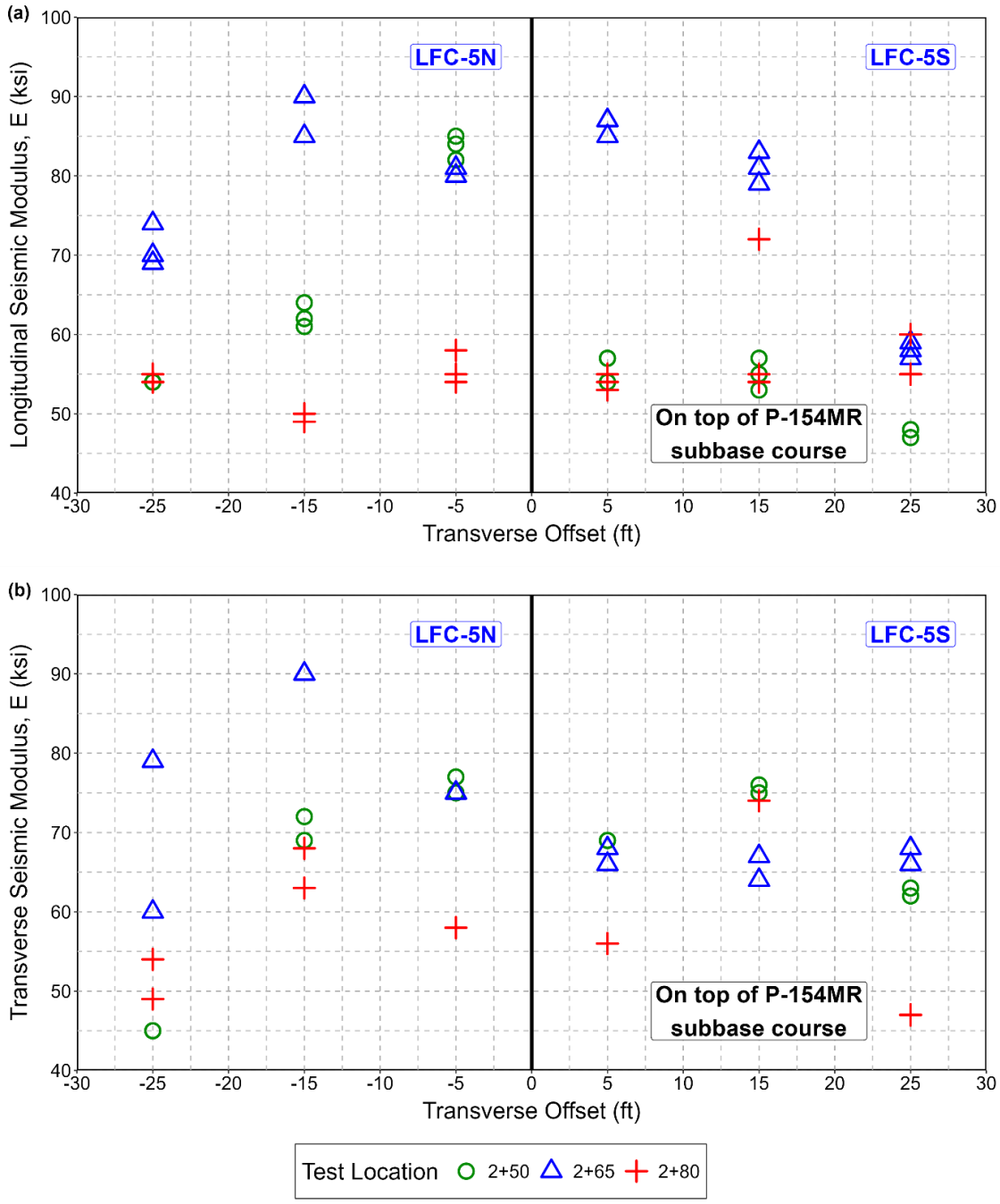

Figure 10. As-Built Subbase Seismic Modulus in Overload Test Items Measured with D-PSPA

Figure 11 plots top-of-subbase GeoGauge moduli against the transverse offset. GeoGauge exhibited the lowest variability among the three testing devices. However, subbases in both test items might have had similar moduli considering the reported variability.

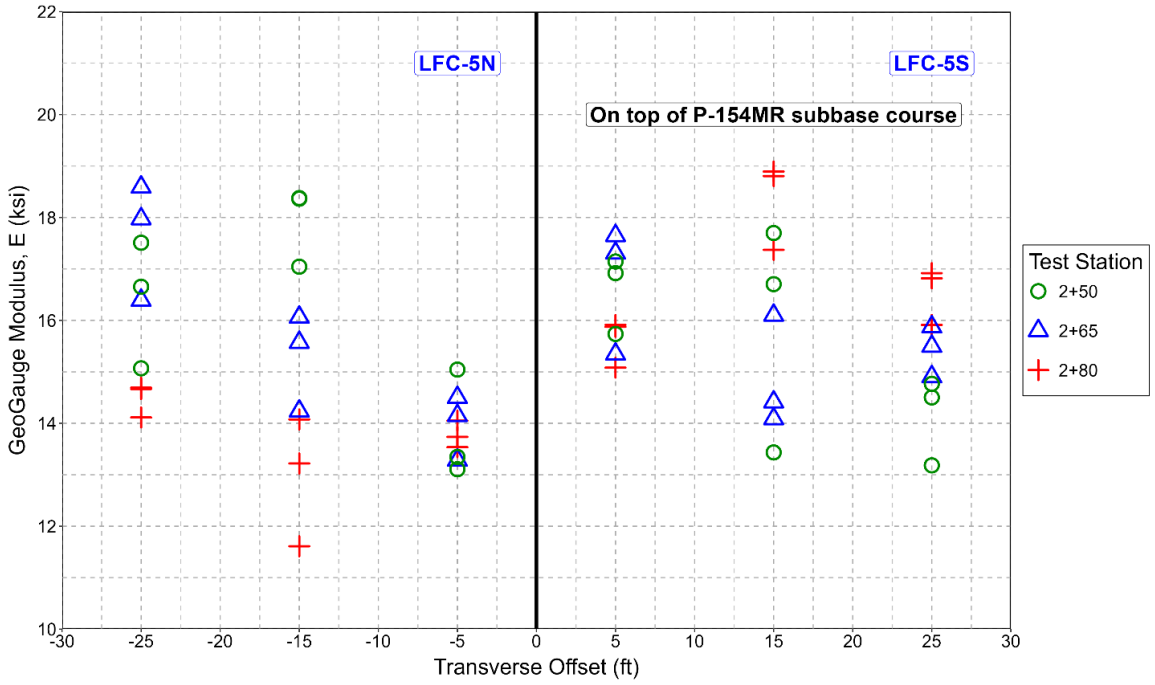

Figure 11. As-Built Subbase Modulus in Overload Test Items Measured with GeoGauge

2.2.3 Base Course (P-209 MR)

Table 5 lists summary statistics for five material properties measured on the base course. Like the subbase layer (Section 2.2.2), the LFC-5N side exhibited a slightly higher mean dry density than LFC-5S as measured by the nuclear gauge. LWD showed an increase in average modulus values compared to top-of-subbase values, but neither D-PSPA nor GeoGauge showed the same trend; indeed, the latter two tests both showed a decrease compared to Table 4. This result could indicate either a compaction issue or a testing equipment issue.

Table 5. Summary of In-Place Characterization of Base-Course Materials

Test Item	**LFC-5N**			**LFC-5S**		
Properties	**μ**	**σ**	**COV (%)**	**μ**	**σ**	**COV (%)**
Nuclear gauge density (pcf)	154.2	N/A	N/A	151.8	N/A	N/A
Nuclear gauge MC (%)	2.5	N/A	N/A	2.2	N/A	N/A
LWD modulus (ksi)	28.6	3.3	11.7	25.7	1.9	7.3
Seismic modulus (ksi)	53.5	16.8	31.3	46.1	11.7	25.4
GeoGauge modulus (ksi)	13.2	1.5	11.2	13.3	2	14.8

μ = Mean, σ = Standard deviation, COV = Coefficient of variation

Figure 12 plots the LWD modulus at top of base against the corresponding LWD plate contact stresses. The base layers of both LFC-5N and LFC-5S show the stress-hardening behavior expected in aggregate materials, as LWD modulus increases with increasing stress. The LWD modulus values exhibited slightly higher variation in LFC-5S than in LFC-5N.

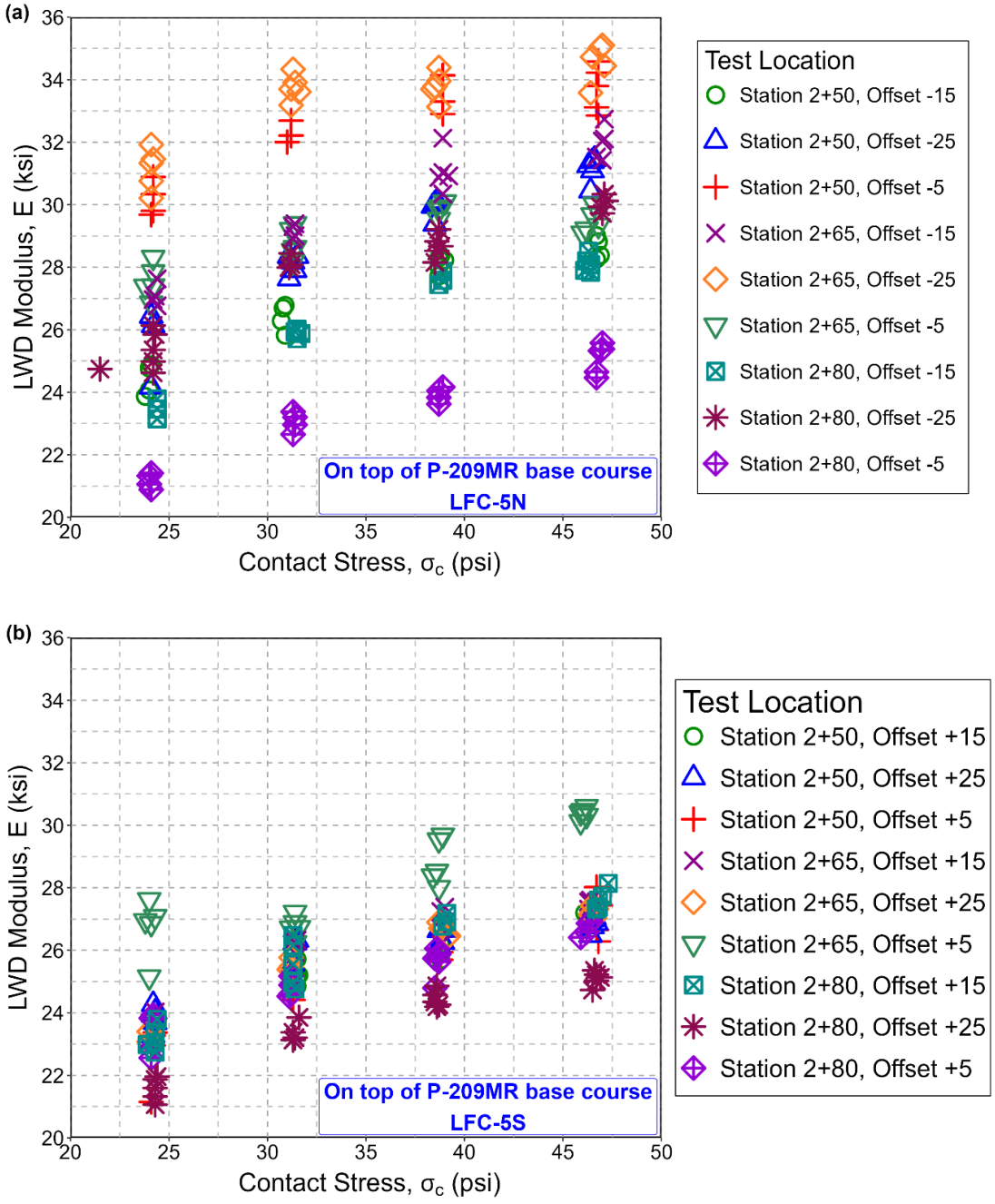

Figure 12. As-Built Base Modulus in Overload Test Items Measured with Light Weight Deflectometer

Figure 13 plots top-of-base seismic moduli measured in the longitudinal (top) and transverse (bottom) directions against the transverse offset. Measurements on LFC-5N exhibited somewhat higher variation than on LFC-5S, contrary to the LWD observations.

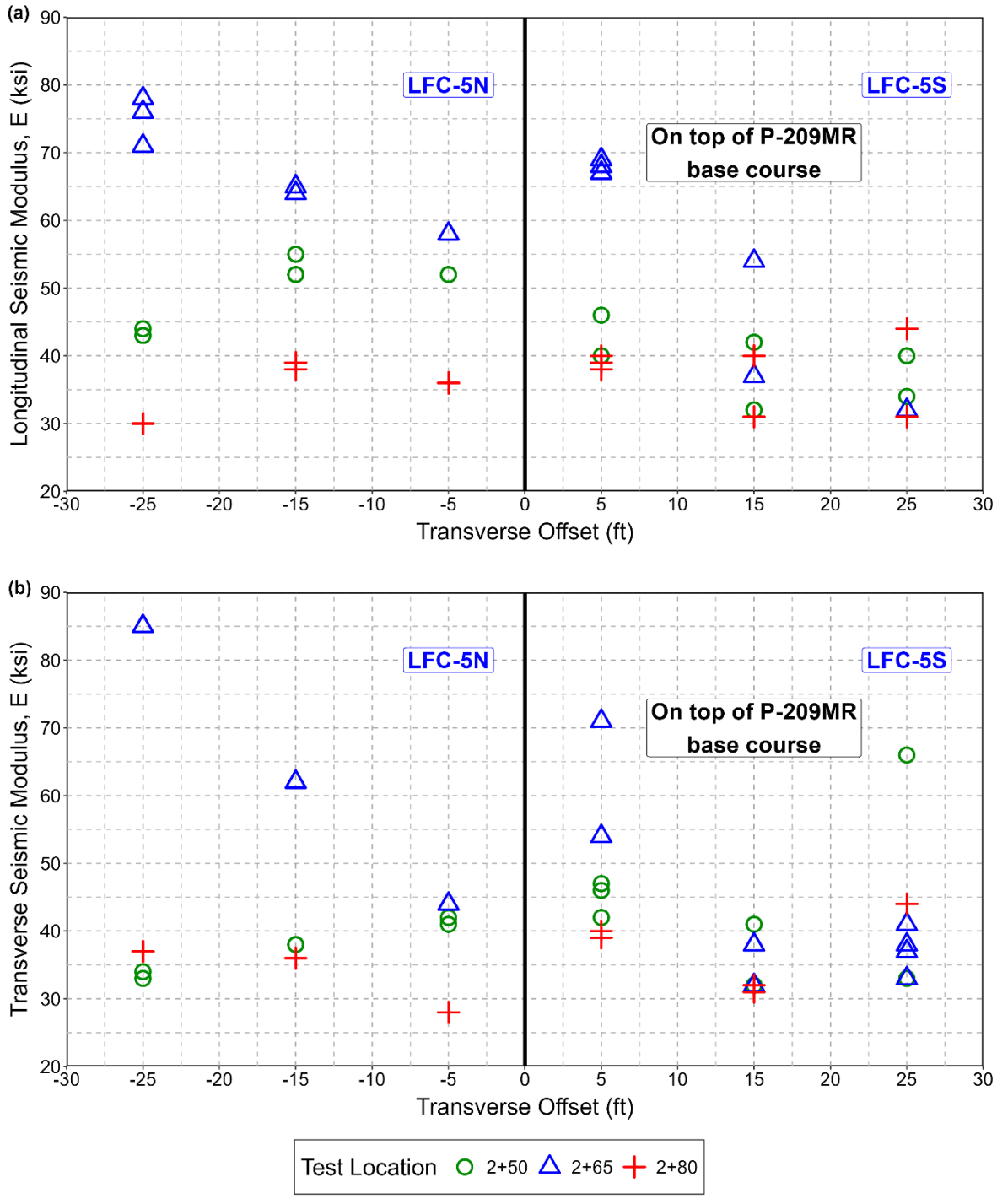

Figure 13. As-Built Base Seismic Modulus in Overload Test Items Measured with D-PSPA

Figure 14 plots top-of-base GeoGauge moduli against the transverse offset. GeoGauge exhibited the lowest variability among the three testing devices.

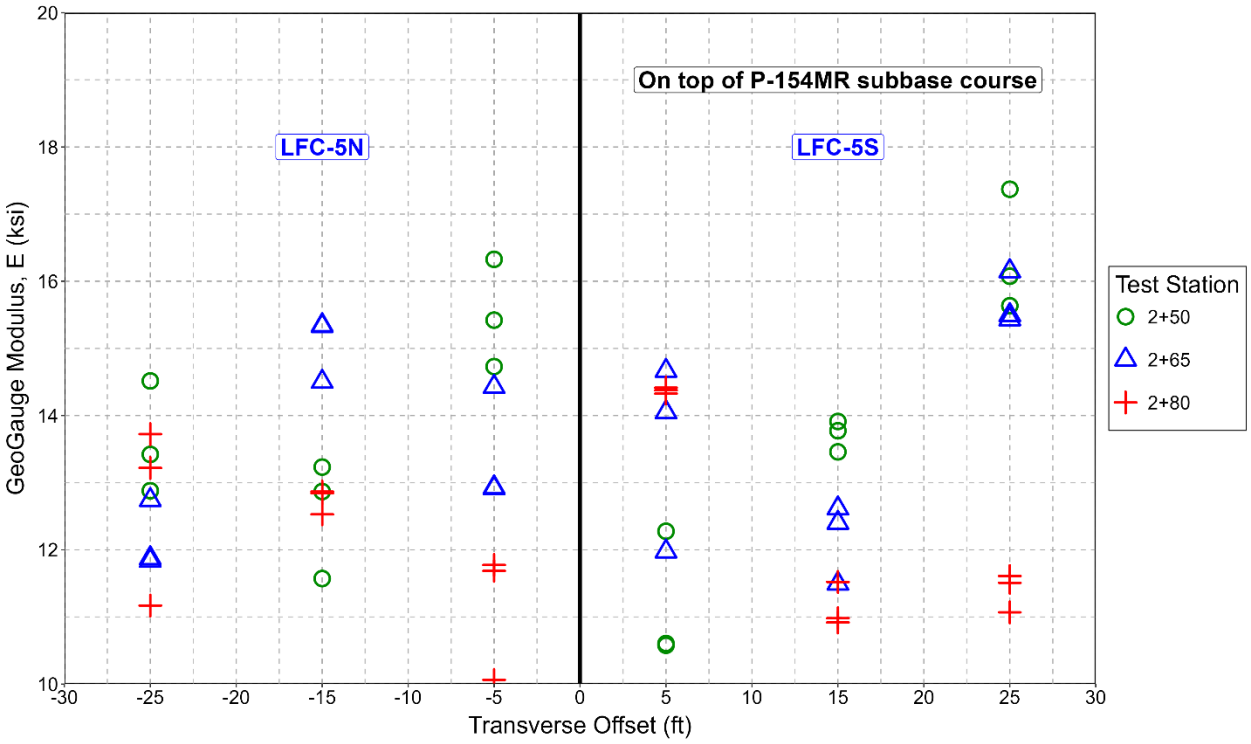

Figure 14. As-Built Base Modulus in Overload Test Items Measured with GeoGauge

2.2.4 Asphalt Concrete (P-401MR)

Table 6 summarizes the Quality Assurance/Quality Control (QA/QC) results for the AC surface layer. Mat densities for the two test items exhibit some disparity, but joint densities and air voids were practically identical. Seismic moduli were obtained from the PSPA device, and elastic moduli were backcalculated from heavy weight deflectometer (HWD) tests. Both seismic modulus and backcalculated modulus were higher on the LFC-5N side than on LFC-5S.

Table 6. Summary of In-Place Characterization of P-401 AC Layer

Test Item	**LFC-5N**			**LFC-5S**		
Properties	**μ**	**σ**	**COV (%)**	**μ**	**σ**	**COV (%)**
Mat density (%)	93.7	N/A	N/A	95.2	N/A	N/A
Joint density (%)	94.3	0.8	0.8	94.3	0.8	0.8
Lab air voids (%)	6.4	N/A	N/A	6.4	N/A	N/A
Seismic modulus (ksi)	2,289.00	584.1	25.5	2013.2	285.7	14.2
Elastic modulus (ksi)	891.7	84.3	9.5	839	92.8	11.1

μ = Mean, σ = Standard deviation, COV = Coefficient of variation

2.3 REVIEW OF INSTRUMENTATION

Sensors were installed in both test items to monitor the critical pavement responses. Embedded sensors included asphalt strain gauges (ASGs), coil sensors (CSs), pressure cells (PCs), moisture sensors (MSs), and thermocouples. Details are found in the CC9 Construction Report (Tomlinson et al., 2022). Appendix A gives sensor locations for the overload test items. Figure 15 and Figure 16 show the sensor layouts for LFC-5N and LFC-5S, respectively.

A wander sequence consisting of 66 passes on 9 tracks was used to traffic CC9. Dynamic sensors (ASG, CS, and PC) were aligned with the wheel paths on certain tracks, such that they record the maximum critical response under the wheel. Figure 15 and Figure 16 show the tracks that produce the maximum responses for specific sensor types. In general, Track 0 is critical for ASG and Tracks 3 and -3 for CS and PC. Section 4. covers tracking and sensor response in more detail.

2.3.1 Asphalt Strain Gauges

ASGs were of two types, sourced from different manufacturers. Type 1 was a quarter bridge sensor (single leg of the Wheatstone bridge), while Type 2 was full bridge (connecting all four legs of the Wheatstone bridge). The full bridge sensors were anticipated to be more sensitive than the quarter bridge gauges. Eight quarter-bridge gauges and four full-bridge gauges were installed in the overload test area. The Type 1 and Type 2 asphalt strain gauges are highlighted with blue and black colors in Figure 15 and Figure 16. Using both types allowed the FAA to compare strain response and survivability under similar load conditions.

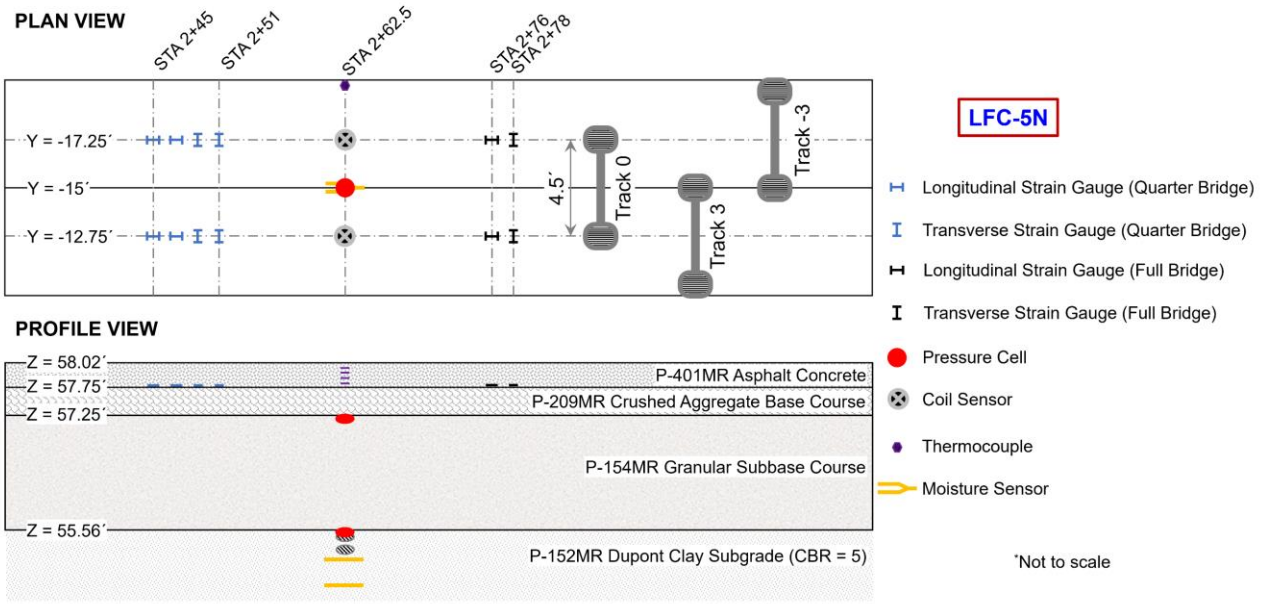

Figure 15. Layout of Instrumentation in Overload Test Item LFC-5N

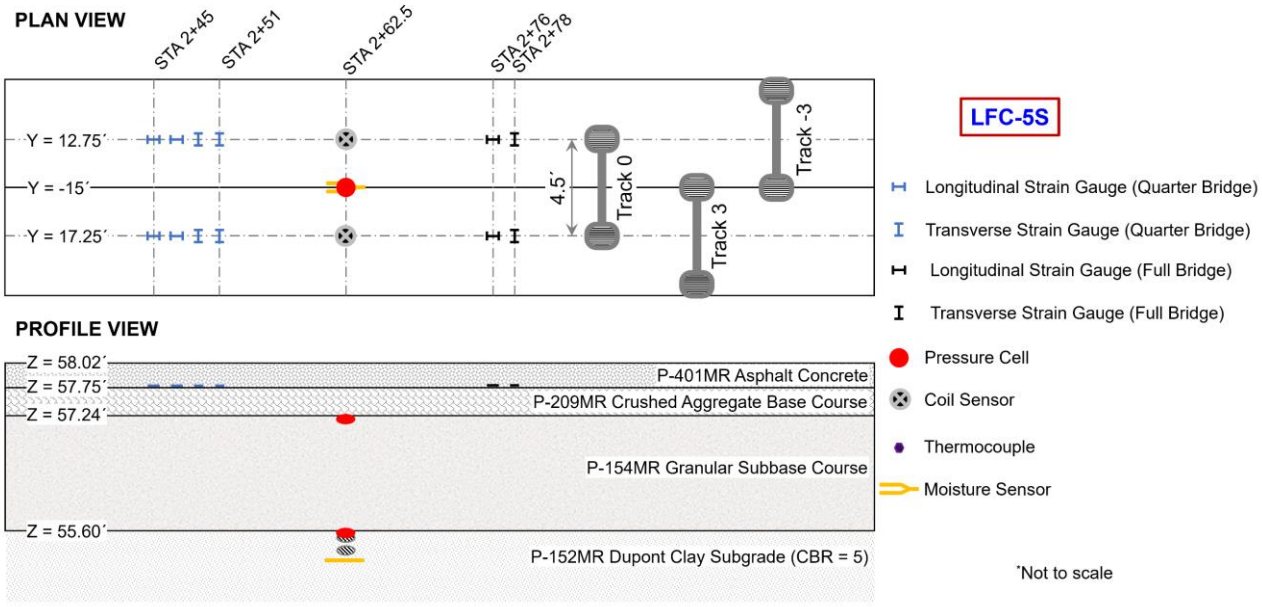

Figure 16. Layout of Instrumentation in Overload Test Item LFC-5S

2.3.2 Pressure Cells

PCs were installed along the center offset (15 ft) of the north and south test items. One PC was installed at the top of the subbase, and one at the top of the subgrade in both test items.

2.3.3 Coil Sensors

Paired induction CSs spaced at approximately 3 in. were installed near the top of the subgrade to measure traffic-induced compressive strain. The induction-coil based strain measurement system (known as ε-mu, an acronym for strain (ε) measuring unit) has been used extensively to monitor permanent deformation and strain in pavement subsurface layers. The system was originally developed by Selig and Grangaard (1970). The data acquisition process was later automated by Dawson (1994).

2.3.4 Static Sensors

A thermocouple tree consisting of six temperature probes was installed in the AC layer of LFS-4N only. MSs were installed at two depths within the subgrade soil.

3. LABORATORY MATERIAL CHARACTERIZATION

This section reviews specific aspects of the CC9 material characterization activities that explain observations from the overload traffic tests. During construction, laboratory test materials were retrieved from subgrade (P-152MR), subbase (P-154), base (P-209), and asphalt (P-401) layers. The subgrade material specimens were collected in Shelby tubes (12 in. long and 3 in. diameter) at random locations at the top of the finished subgrade along the pavement center line. Two specimens were taken from within the overload test area (Table 7). Subbase and base materials were collected

in 5-gallon buckets. Fifteen 5-gallon buckets of the PG 64-22 asphalt concrete mix used in the overload test area were collected from the plant for advanced material characterization.

Resilient modulus tests on the subgrade and base courses are discussed in Section 3.1 . AC and binder were tested to quantify rutting, fatigue, and cracking potential. Laboratory tests related to rutting potential of the asphalt mixture were asphalt pavement analyzer (APA) rut depth, high-temperature indirect tensile strength, and flow number. Additional laboratory tests (i.e., intermediate temperature semi-circular bend, flexural beam fatigue, viscoelastic continuum damage, and low-temperature disk-shaped compact tension) were conducted on the neat binder to investigate fatigue and cracking behavior.

3.1 RESILIENT MODULUS OF GRANULAR MATERIALS

Resilient modulus tests were performed on both fine-grained subgrade (P-152MR), granular subbase (P-154MR), and base (P-209MR) materials following AASHTO T307 (AASHTO, 2021) guidance. Compacted specimens were tested at three confining pressures and five cyclic deviator stresses, replicating 15 stress sequences. Per AASHTO P307, confining pressures and deviator stresses were higher for granular materials. Estimated resilient moduli, bulk stresses, and octahedral shear stresses were then fitted to the mechanistic-empirical pavement design guide (MEPDG) model (AASHTO, 2008) to characterize the nonlinear stress-dependent behavior of unbound aggregates. The MEPDG model is known popularly as the enhanced universal model because it can accommodate both stress-hardening and stress-softening behavior of geomaterials. The following equation describes the form of the enhanced universal model.

$$M_R = k_1 p_a \left(\frac{\theta}{p_a}\right)^{k_2} \left(\frac{\tau_{oct}}{p_a} + 1\right)^{k_3} \quad (3)$$

where:

M_R = resilient modulus,
$\theta = \sigma_d + 3\sigma_3$= bulk stress,
σ_d = deviator stress,
σ_3 = confining stress,
$\tau_{oct} = \frac{1}{3}\sqrt{(\sigma_1 - \sigma_2)^2 + (\sigma_2 - \sigma_3)^2 + (\sigma_3 - \sigma_1)^2}$ = octahedral shear stress,
σ_1 = major principal stress,
σ_2, σ_3= intermediate and minor principal stresses,
p_a= atmospheric pressure,
K, n = model parameters obtained from multiple regression,
k_1, k_2, k_3 = model parameters obtained from multiple regression.

Regression coefficient k_1 should take a positive value and is proportional to the elastic modulus of the material. Coefficient k_2 corresponds to the bulk stress term and should have a positive value. A positive bulk stress term indicates hardening behavior (where the resilient modulus of unbound materials increases with increasing confinement and deviatoric stress). The value of k_3 relates to shearing behavior and is expected to be negative. An increase in the octahedral shear stress and associated high shear stress coefficient leads to lower modulus values and indicates stress softening behavior.

3.1.1 Subgrade

Resilient modulus tests were performed on the two samples of subgrade material collected from the CC9 overload test area. The resilient modulus test protocol (AASHTO, 2021) includes the quick shear (QS) test at zero confining pressure to obtain the unconfined compressive strength (UCS) of the material. Table 7 summarizes the test results. The universal model fitted the data well for both samples as indicated by the high coefficient of determination. Resilient modulus values in the table use confining pressure 2 psi and deviator stress 8 psi. Table 2 shows that the sample from test item LFC-5N had higher modulus and UCS than the sample from test item LFC-5S. However, both samples were taken from the area of the centerline (offsets ±1 ft. from centerline) and should not be considered representative of the respective test items.

3.1.2 Granular Subbase

Figure 17 shows resilient modulus data for P-154 material used in the overload test items. Corresponding universal model parameters are shown for each replicate. Stress-hardening behavior of the granular materials was evident, because the resilient modulus increased with increasing deviator stress and bulk stress. The first replicate exhibited both the highest stiffening term (k_1) and the highest shear stress term (k_3).

3.1.3 Base Course

Figure 18 shows resilient modulus data for P-209 material sampled from the overload test area. As expected, the P-209 material exhibited stress-hardening behavior. Resilient modulus ranged from 20 to 100 ksi.

Table 7. Summary of Subgrade (P-152MR) Resilient Modulus

Specimen ID	Test Item	Station	Offset (ft)	Moisture Content (%)			Dry Density (pcf)	Predictive Model Coefficients			Statistical Parameters		Resilient Modulus, M_R (psi)	Unconfined Compressive Strength (psi)
				Average	Max	Min		k_1	k_2	k_3	S_e/S_y	R^2_{adj}		
STA 2+78	LFC-5S	2+78	+1	25.4	25.8	25.2	99.4	1032.4	0.232	-2.664	0.140	0.98	8,156	25.9
STA 2+83	LFC-5N	2+83	-1	23.5	23.9	23.1	102.5	1617.6	0.466	-3.211	0.156	0.97	11,152	33.6

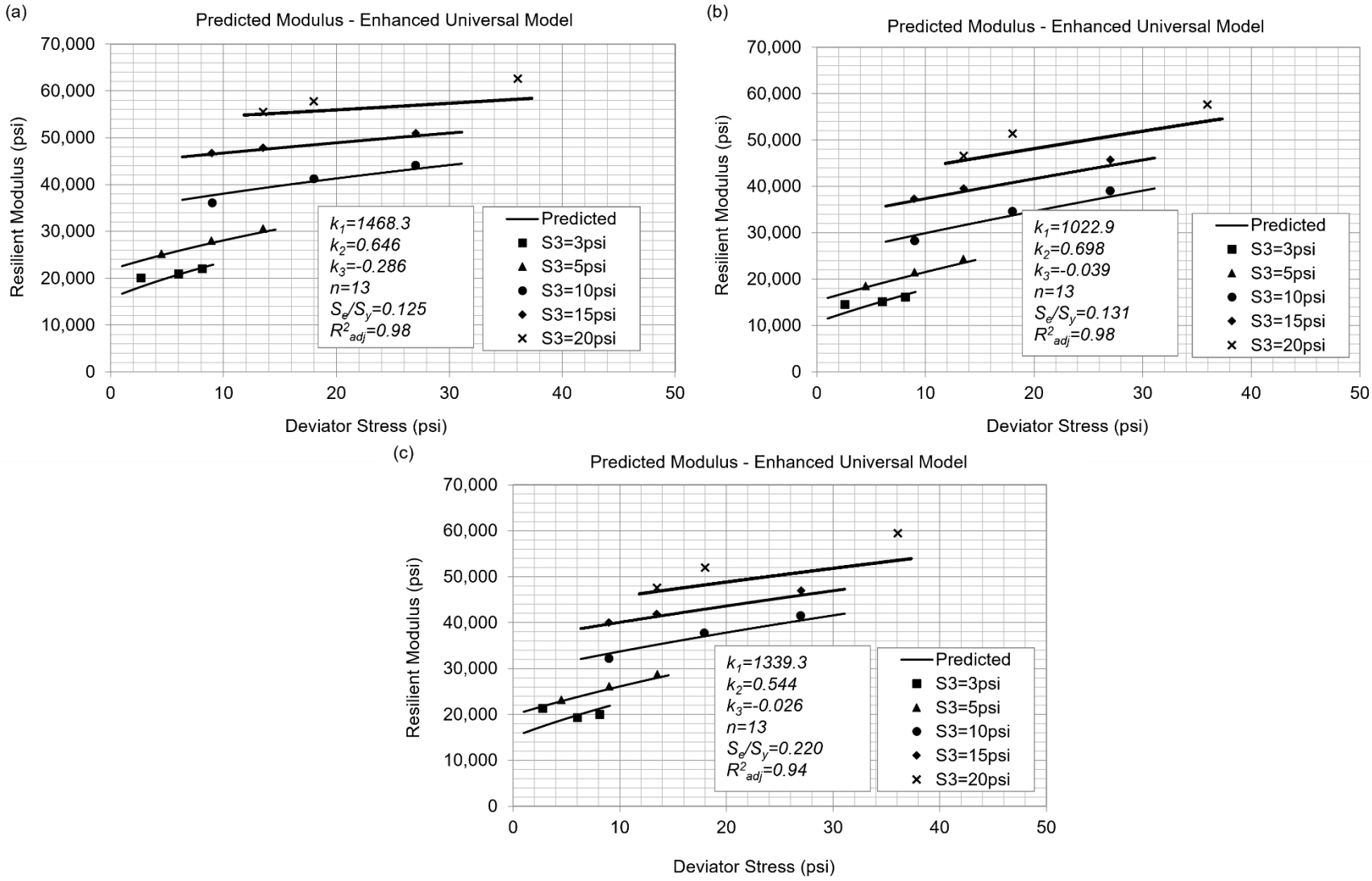

Figure 17. Resilient Modulus of Granular Subbase (P-154MR) Sampled During the Construction of Overload Test Items

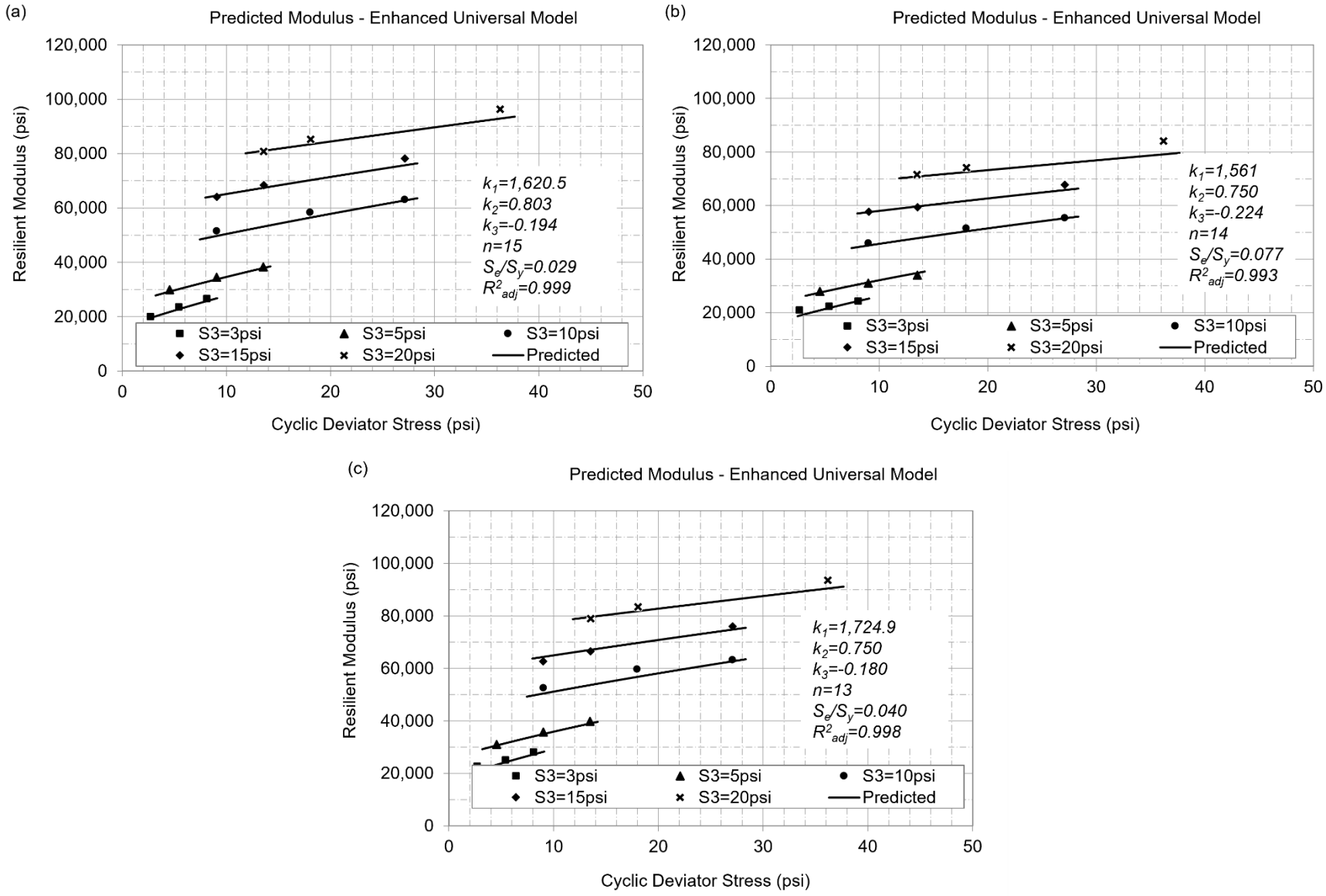

Figure 18. Resilient Modulus of Crushed Aggregate Base (P-209MR) Sampled During the Construction of Overload Test Items

3.2 ASPHALT CONCRETE

This section reviews the viscoelastic stiffness, rutting, and fatigue cracking potential of the asphalt mixture (PG 64-22) used in the surface layer of the overload test items.

3.2.1 Dynamic Modulus

Dynamic modulus tests were conducted on asphalt concrete specimens following AASHTO T342 (AASHTO, 2019). Three specimens with a diameter of 4 in.es and trimmed height of 6 in.es were tested at four temperatures: 14 °F, 39 °F, 70 °F, and 99 °F, using loading frequencies of 25, 10, 5, 1, 0.5, and 0.1 Hz. Figure 19 shows (a) master curves for dynamic modulus, (b) phase angle at a reference temperature of 70 °F, and (c) black space diagram for the PG 64-22 AC mix used in the overload test. Dynamic modulus decreased with increasing phase angle (as expected). Phase angle initially increased with frequency (a high-temperature phase), but after reaching a peak value, the phase angle then decreased with further frequency increases. Similar behavior was also evident from the black space diagram. An observed increase in phase angle with frequency may be linked to aggregate interlock, i.e., at high temperature the asphalt mastic is very soft, and the aggregate skeleton (which resists the load) exhibits stress-hardening behavior.

3.2.2 Rutting-Related Tests

3.2.2.1 Asphalt Pavement Analyzer

Figure 20(a) and (b) show average APA rut depths for samples prepared from the PG 64-22 mix for two hose pressures (100 and 250 psi). Samples were tested at 147 °F (64 °C), which falls on the high temperature end of the binder performance grade. AASHTO T340 sets the benchmark hose pressure for the APA test at 100 psi. However, this standard hose pressure is intended to replicate highway stress conditions. FAA Advisory Circular (FAA AC) 150/5370-10H recommends a higher hose pressure of 250 psi but also permits use of the AASHTO T340 test at 100 psi hose pressure (FAA, 2018). As shown in Figure 20. The PG 64-22 mix satisfied the FAA AC 150/5370-10H APA test criteria for both hose pressures.

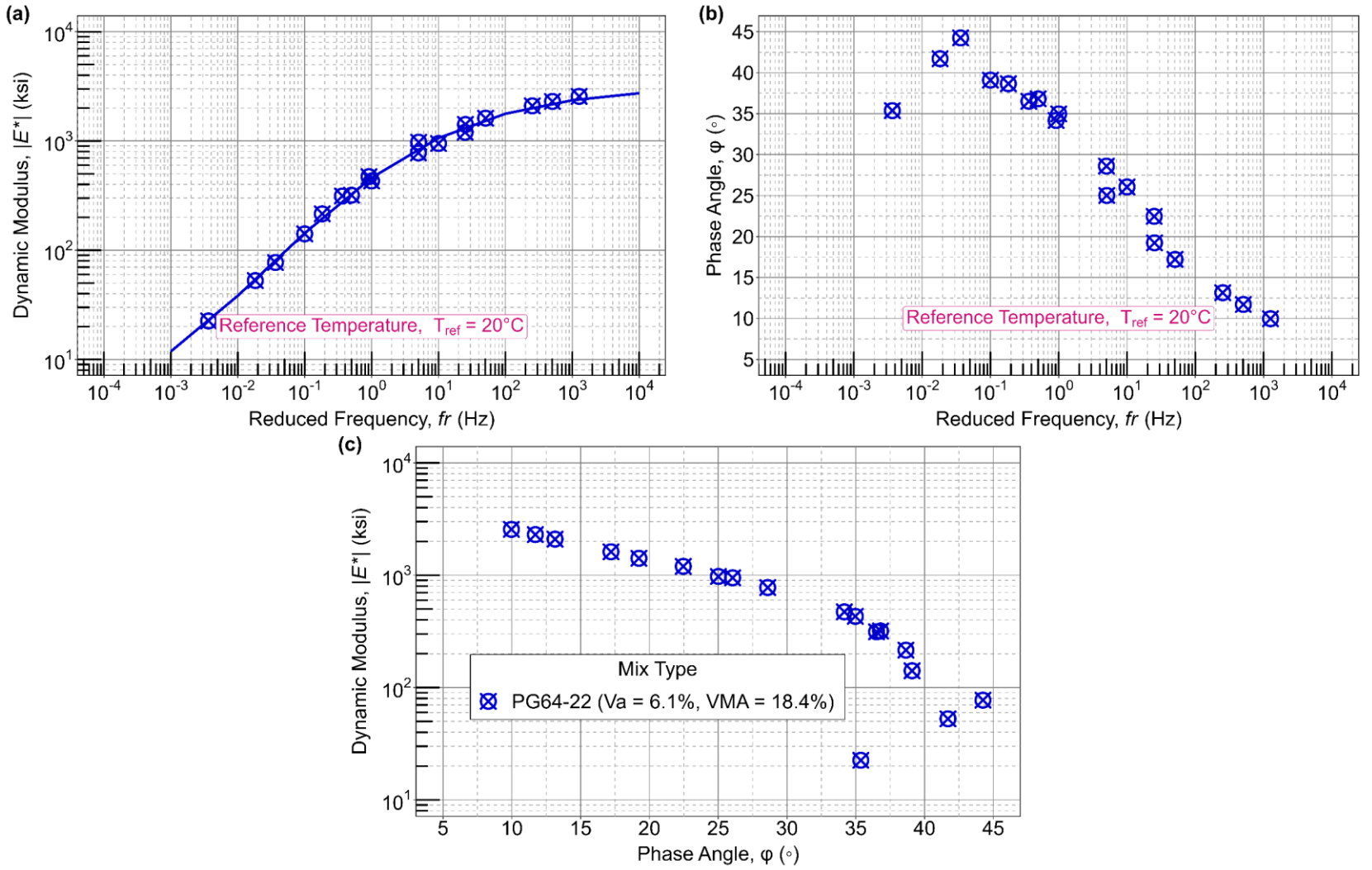

Figure 19. (a) Dynamic Modulus Master Curves, (b) Phase Angle Master Curves, and (c) Black Space Diagram of CC9 Asphalt Concrete Mixes

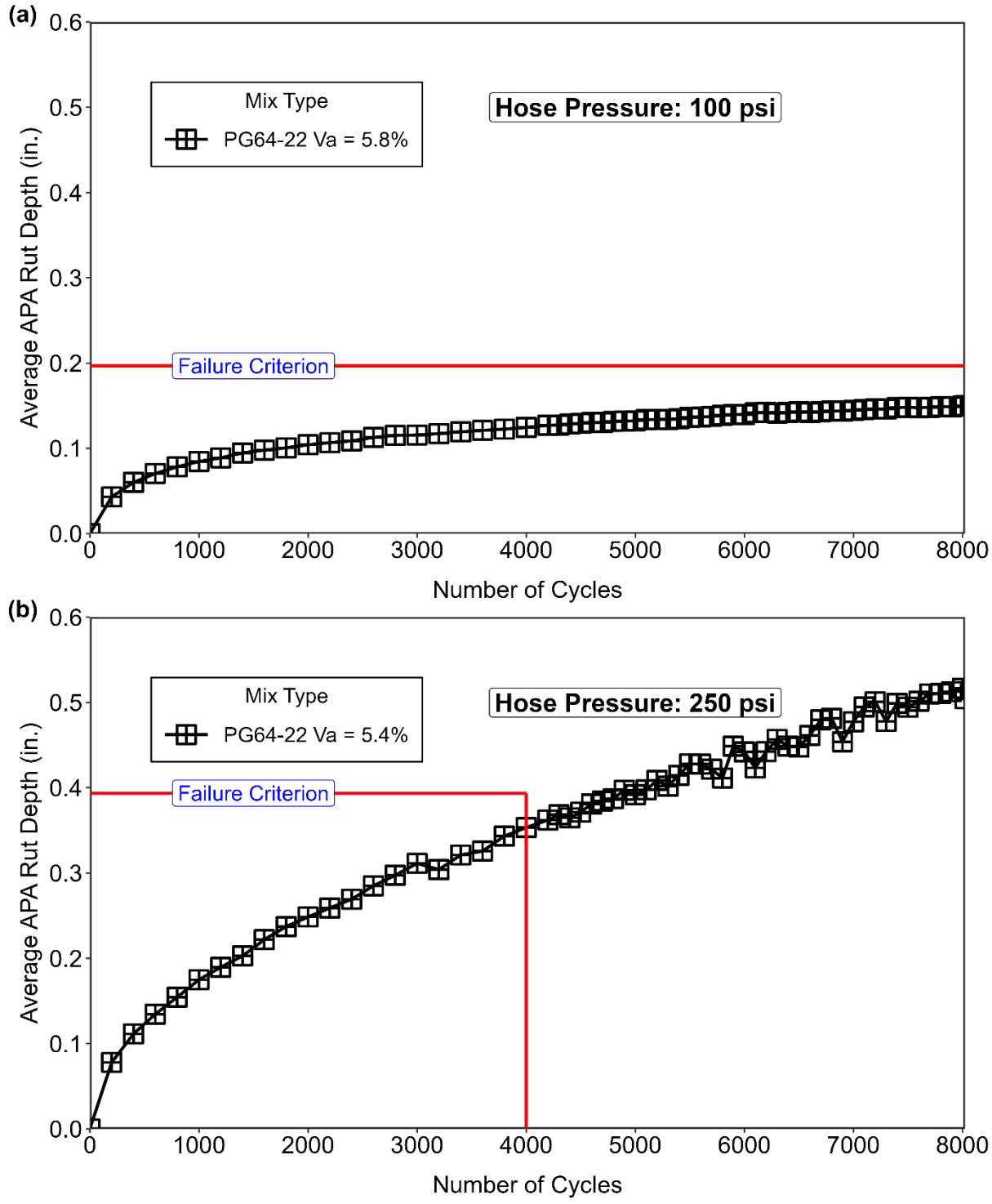

Figure 20. Asphalt Pavement Analyzer Rut Depths of PG 64-22 Mix used in CC9 Overload Test Items at (a) 100-psi and (b) 250-psi Hose Pressures

3.2.2.2 Flow Number

Three asphalt specimens were tested for flow number (FN). Tests were conducted without applying confining pressure, considering the high variability in flow numbers previously observed in confined testing on similar mixes (Tomlinson et al., 2022; Kazmee et al., 2019). As shown in Figure 21, tested samples exhibited small variability in flow number. Observed flow numbers were much lower than the limiting criterion FN = 200 for a rut-resistant mix proposed by Rushing et al. (2012).

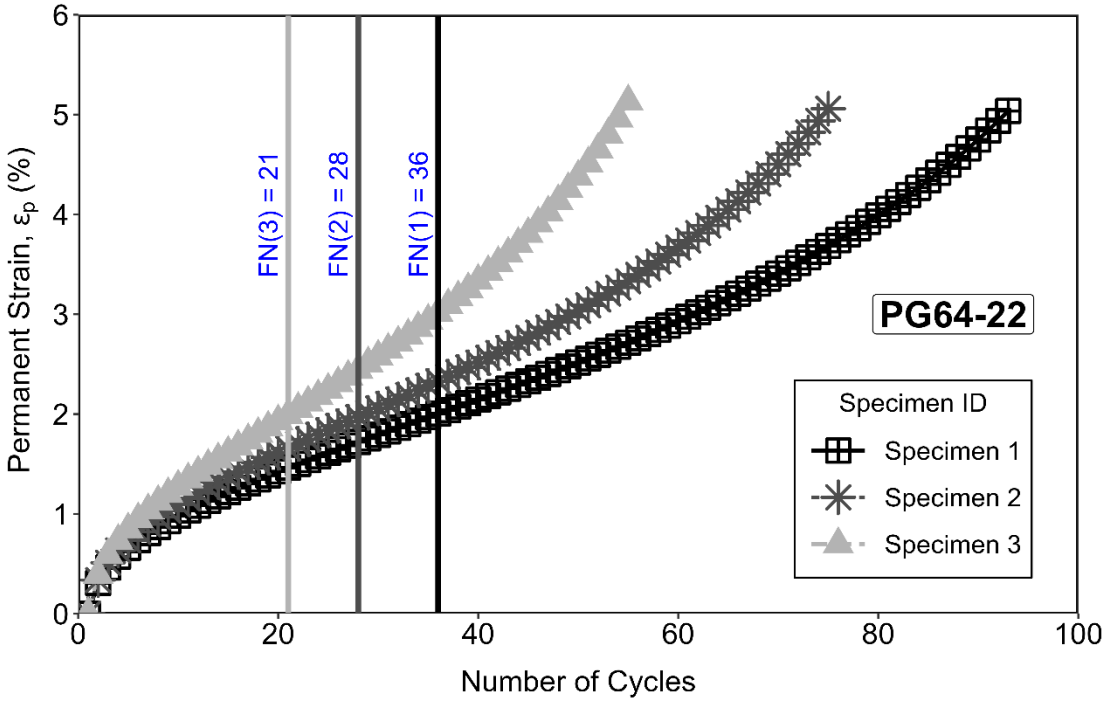

Figure 21. Flow Number of PG 64-22 Mix Used in CC9 Overload Test Items

3.2.2.3 High-Temperature Indirect Tensile Strength

Three asphalt samples from the overload test area were tested using an indirect tensile (IDT) testing apparatus following American Society for Testing and Materials (ASTM) D6391-17. IDT tests followed the standard procedure except the temperature was increased from 25 °C to 40 °C, hence these tests are referred to as high-temperature indirect tensile strength (HTITS) tests. Research (Batioja-Alvarez et al., 2024) indicates that the HTITS test correlates well with APT and may serve as a rutting performance indicator. Table 8 summarizes the HTITS results and shows that HTITS decreased with increasing air voids.

Table 8. High-Temperature Indirect Tensile Strength S Test Results for PG 64-22 Mixture Used in CC9 Overload Test Items (All samples tested at 40 °C.)

Sample No.	Air Void, %	Indirect Tensile Strength, psi
64-4	4.7	43.5
64-9	5.3	37.7
64-10	5.6	34.8

3.2.3 Cracking-Related Tests

3.2.3.1 Flexural Beam Fatigue Tests

Figure 22 shows the results of flexible beam fatigue tests performed on beam samples prepared from the PG 64-22 asphalt mixture used in CC9 overload test items. Figure 23(a) shows the initial flexural stiffness *S*, which decreases with increasing strain. Figure 23(b) shows number of cycles to fatigue failure (defined in this test as 50% reduction of initial flexural stiffness). Flexural bending tests were conducted at room temperature. For this reason, the predicted fatigue life from the strain-controlled tests may not be transferrable to NAPTF traffic tests under a range of temperature conditions. Furthermore, peak tensile strains from asphalt strain gauges in LFC-5 were significantly higher than the fatigue test strains. Strain data from the traffic tests are presented in Section 5. .

The FAA Rigid and Flexible Iterative Elastic Layered Design (FAARFIELD) asphalt fatigue failure model makes use of the concept of dissipated energy, so a brief description of the ratio of dissipated energy change (RDEC) model follows. The flexural beam fatigue test is the basis of this model and yields the relevant properties. During repeated loading-unloading events, a time-temperature-dependent material (e.g., asphalt) responds with successive time delays following different trajectories, a phenomenon known as hysteresis loops (Carpenter and Shen, 2006). The area of each loop represents the energy dissipated during the loading-unloading event. Based on strain-controlled flexural beam fatigue tests, Carpenter and Jansen (1997) found a relationship between the relative change in dissipated energy and fatigue damage in the asphalt concrete.

Carpenter and Jansen (1997) identified three distinct stages of fatigue damage. Stage I is the initial change in dissipated energy at the beginning of load applications. Stage II corresponds to the plateau period at which the RDEC remains stable over many cycles. True fatigue failure of the asphalt material is marked by a steep increase in RDEC, designated as Stage III.

The stable RDEC in Stage II is defined as the plateau value (PV). Carpenter et al. (2003) reported a unique fundamental relationship between the PV and the number of cycles to 50% stiffness reduction. With further expansion of that work, Carpenter and Shen (2006) proposed a step-by-step procedure to estimate the PV where RDEC can be expressed as:

$$RDEC_a = \frac{DE_a - DE_b}{DE_a \times (b-a)} \quad (4)$$

where:

$RDEC_a$ = average ratio of dissipated energy at cycle a compared to cycle b,
DE_a, DE_b = dissipated energy produced at load cycles a and b, respectively.

For convenience, the difference in cycle counts (*b*-*a*) is generally taken as 100. The average RDEC per 100 cycles at cycle *a* can be computed using the following equation:

$$RDEC_a = \frac{1-\left(1+\frac{100}{a}\right)^f}{100} \quad (5)$$

Carpenter and Shen (2006) demonstrated that the parameter *f* can be computed as the slope of the power relation-based regression curve relating the dissipated energy to the number of load cycles until fatigue failure at 50% stiffness reduction. The term PV can thus be defined as:

$$PV = \frac{1-\left(1+\frac{100}{Nf_{50}}\right)^f}{100} \quad (6)$$

Shen and Carpenter (2007) developed a statistical correlation to predict the PV values using the initial flexural stiffness (S), gradation parameters (GP), and volumetrics (VP). The same equation was integrated into FAARFIELD 1.4 (FAA, 2017) as an asphalt fatigue failure model.

$$PV = 44.422\varepsilon^{5.140}S^{2.993}VP^{1.850}GP^{-0.4063} \quad (7)$$

where:

$VP = \frac{AV}{AV+V_b}$
AV = mixture air voids,
V_b = asphalt content by volume,
$GP = \frac{P_{NMS}-P_{PCS}}{P_{200}}$,
P_{NMS} = percent passing through nominal maximum sieve size,
P_{PCS} = percent passing through primary control sieve, and
P_{200} = percent passing through No. 200 (0.074 mm) sieve.

Figure 22(c) and (d) compare PV and number of cycles to failure for the PG 64-22 asphalt mix based on the FAARFIELD asphalt fatigue failure model to direct estimates from laboratory PV data. The FAARFIELD model underpredicted PV compared to the direct laboratory estimates (Figure 23(c)). Accordingly, FAARFIELD predicts a higher number of cycles to failure compared to fatigue life based on laboratory-determined PV (Figure 23(d)).

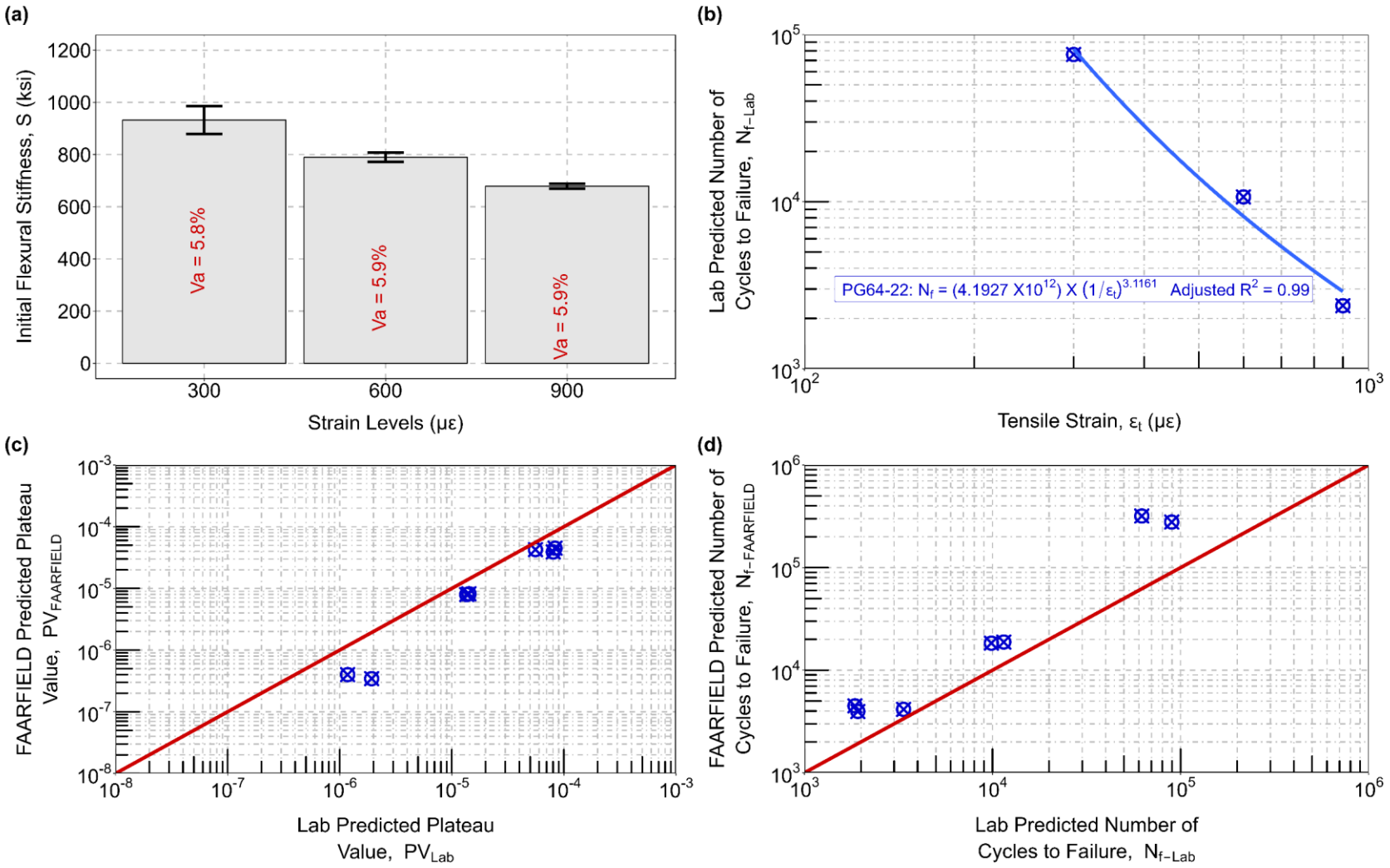

Figure 22. (a) Initial Flexural Stiffness, (b) Fatigue Life at Three Strain Levels, (c) Predicted Plateau Values, and (d) Predicted Fatigue Life of PG 64-22 Mix used in Overload Test Items

Figure 23 plots PV versus number of cycles to fatigue failure for various specimens from NAPTF CC9 and National Airport Pavement and Materials Research Center (NAPMRC) Test Cycles 1 and 2 (TC-1 and TC-2). PV correlated well with the fatigue life regardless of mix types or material sources, substantiating the findings of Carpenter et al. (2003).

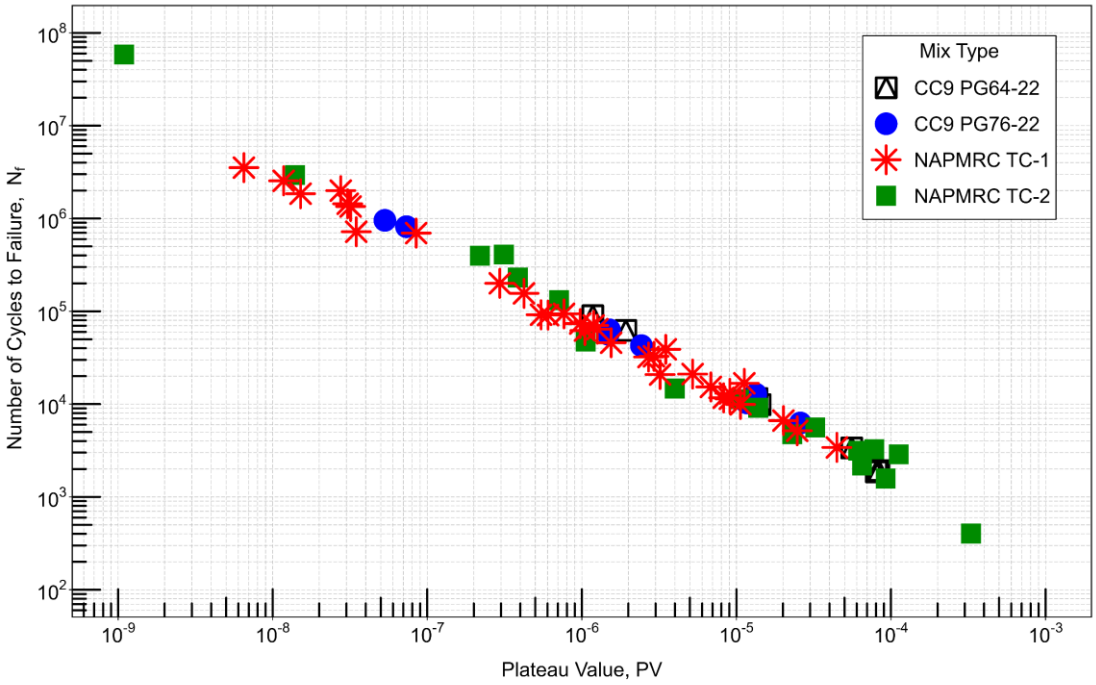

Figure 23. Correlation Between PV and Fatigue Life

3.2.3.2 Semi-Circular Bend and Disk-Shaped Compact Tension Tests

Figure 24(a) and (b) show fracture energy and flexibility index (FI) as determined by the semi-circular bend (SCB) test following AASHTO TP-124 (AASHTO, 2020), for three asphalt specimens prepared with the PG 64-22 mix. Al-Qadi et al. (2015) related pavement distresses from pavement condition index (PCI) surveys to SCB flexibility indices and developed three distinct categories of performance ranking for balanced mix design. According to that study, field sections having FI value greater than 6.0 exhibited minimal amount of fatigue damage. The PG 64-22 mix used in the overload test items satisfied that criterion. Influence of air voids was inconclusive.

Figure 25(c) shows fracture energy data for the same mixture obtained from disk-shaped compact tension (DCT) tests following ASTM D7313 (ASTM, 2021). The DCT tests were conducted at 50 ºF (10 ºC) above the 7-day minimum temperature of the performance grade (i.e., 10.4 °F) per the standard. Test temperature was selected based on the low-temperature performance grade (-7.6 ºF [-22 ºC]). All three replicates exhibited similar fracture energies irrespective of air voids. Based on the findings from a pilot project, Minnesota Department of Transportation (MnDOT) recommends a minimum of 37.2 Joules per square foot (J/ft^2) (400 Joules per square meter [J/m^2]) fracture energy to resist the low temperature cracking in asphalt concrete (Johanneck et al., 2015). The PG 64-22 mix performed satisfactorily by that metric.

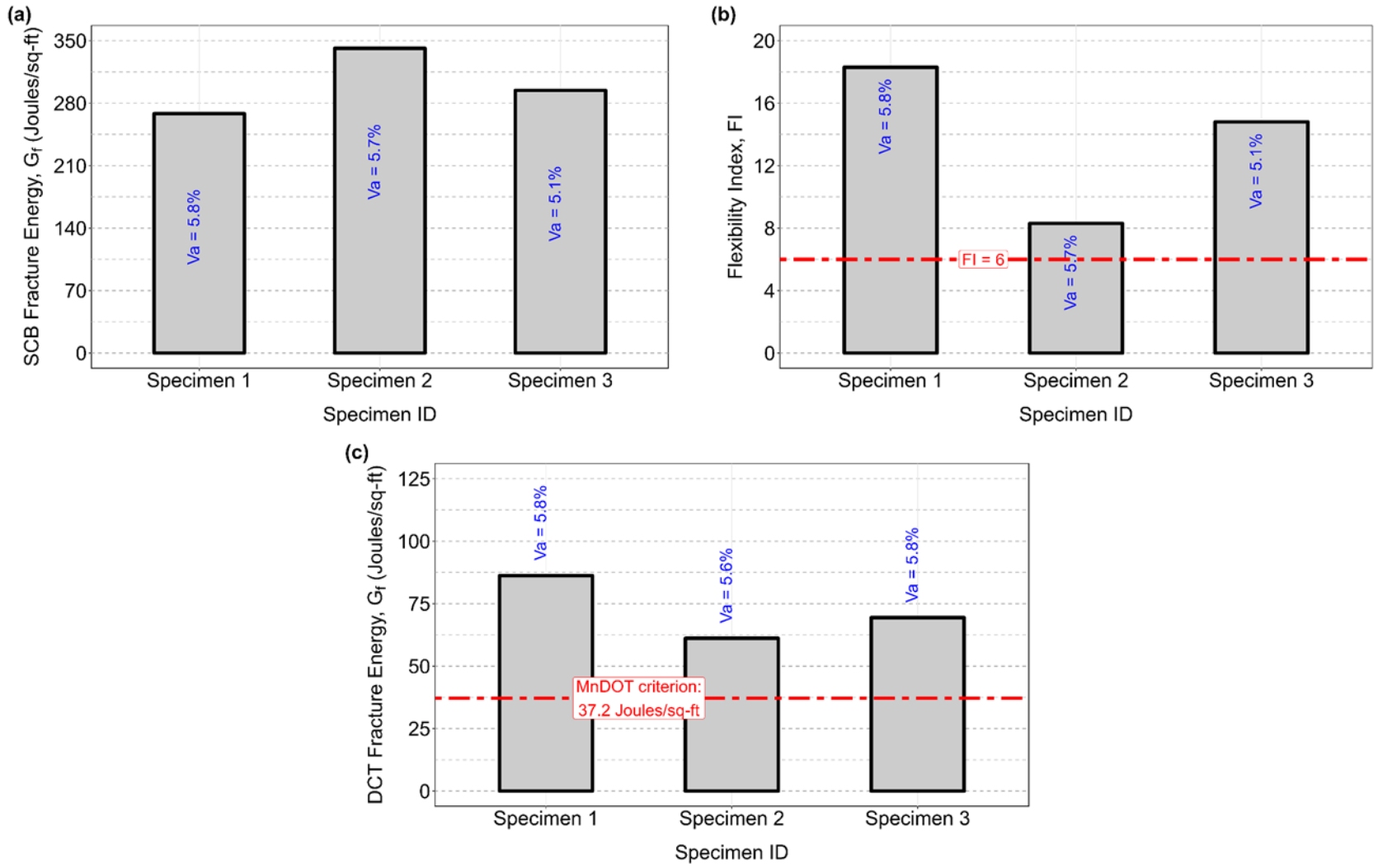

Figure 24. (a) Fracture Energies, (b) Flexibility Indices of SCB, and (c) Fracture Energies of DCT Specimens Consisting of PG 64-22 Mix Used in CC9 Overload Test Items

4. TRAFFIC TESTS ON OVERLOAD TEST ITEMS

4.1 OVERLOAD RATIO (ACR/PCR)

ICAO guidance on pavement overload evaluation accommodates occasional overload traffic with an ACR not exceeding 10% above the reported PCR (ICAO, 2022). The annual number of overload traffic operations is recommended to be less than 5% of the total annual traffic (excluding light aircraft).

Brill and Yin (2018) analyzed the performance of the CC7 overload test items. The CC7 overload tests were designed based on the ACN/PCN system in effect at the time. However, the results from CC7 can be extended to the successor ACR/PCR system. Brill and Yin noted that overloads of up to 50% (based on ACN) did not cause a significant reduction in inherent structural capacity. On the other hand, ACNs exceeding PCN by 90% contributed to accelerated failure. Therefore, they hypothesized the existence of a limiting ACN that separates "normal" performance (i.e., performance following the original design curve) from accelerated failure, which could fall anywhere from 50% to 90% above PCN. The gear configuration did not appear to influence the strain-versus-coverage relationship. The CC9 overload test was intended to supplement the earlier CC7 tests in the context of the newly adopted ACR/PCR system, by providing a controlled test of the limiting overload hypothesis. The overload in CC9 (approximately 75% above PCR) was selected to be in the mid-range of the gap identified in CC7. Appendix E gives ACN/PCN and ACR/PCR calculations for the overload test area.

Table 9 lists the ACR/PCR values applicable to the CC9 overload test area. As shown in Table 9, PCR for the test area was calculated as PCR 352.6/F/D, based on assumed lifetime traffic of 6,500 passes of a dual (D) gear at 36,000 lb per wheel and 200 psi nominal tire pressure. (This traffic likewise results in cumulative damage factor (CDF) = 1.0 for the given pavement structure.) The "normal" traffic load was chosen to be the same as was previously used in the CC7 overload tests for the same flexible pavement cross-section. The PCR computation was based on subgrade CBR 5, equivalent to E = 7500 psi, placing the structure in subgrade category D (very low strength). ACR/PCR ratios were calculated for overloads up to 65,000 lb/wheel at 255 psi tire pressure. Table 9 shows that a wheel load of 57,000 lb produces the target overload ratio of about 75%. Table 9 also reports corresponding values of computed vertical strain ε_{sg} at the top of the subgrade layer, as determined by the computer program LEAF (Layered Elastic Analysis—FAA). As will be shown in subsequent sections, the computed strains are considerably less than in situ peak strains under actual traffic load estimated from CS data.

Table 9. Summary of ACR/PCR Data for CC9 Overload Test Items

Wheel Load (kips)	Tire Pressure (psi)	CDF	PCR/F/D	ACR/F/D	ACR/PCR	ε_{sg} (με)
36	**200**	**1.00**	**352.6**	**352.6**	**1.00**	**1517**
40	255	–	352.6	404.2	1.15	1698
44	255	–	352.6	451.0	1.28	1858
46	255	–	352.6	474.9	1.35	1938
46.5	255	–	352.6	481.1	1.36	1958
48	255	–	352.6	500.0	1.41	2017
52	255	–	352.6	551.2	1.56	2174
56	255	–	352.6	603.7	1.71	2330
57	**255**	–	**352.6**	**616.9**	**1.75**	**2368**
65	255	–	352.6	724.8	2.06	2674

4.2 PRE-TRAFFIC TESTS

4.2.1 Slow-Roll Response Tests

The slow-roll response test was executed November 6–20, 2020, with some tests redone March 1–2, 2021. Pavement responses (stresses, strains, deflections) at relatively low loads were recorded for the following gear configurations: single (S), dual (D), two duals in tandem (2D), and three duals in tandem (3D). The response test variable matrix for LFC-5N/S (overload test area) was as follows:

- Vehicle speed (mph): 0.5, 1.6, 2.5
- Gear offset from centerline (ft): ±8.25, ±10.50, ±12.75, ±15.00, ±17.25, ±19.50
- Wheel Loads (lb): 8,000; 12,000; 16,000
- Tire Pressure: 255 psi
- Passes: two passes for each wheel load at each offset (one forward, one return).

Sensor functionality was assessed under various loads and speeds. Observations from the slow-roll response tests are discussed in the traffic testing summary report (CC9 Technical Report Vol. 1) (Kazmee et al., 2026).

4.2.1.1 Proof Roll

A proof-roll sequence was applied using the carriage positions in Table 10 and Figure 25. As expected, the magnitudes of peak stresses and strains decreased with increasing lateral distance between the embedded sensor and loading wheel. Proof-rolling used a D gear at 15,000 lb per wheel.

Table 10. Carriage Positions for Each Pass of Proof-Roll Wander

Pass Sequence	Direction	Carriage Centerline Location (ft)	
		North	South
1	W–E	-19.34	2.68
2	E–W	-19.34	2.68
3	W–E	-18.507	3.513
4	E–W	-18.507	3.513
5	W–E	-17.674	4.346
6	E–W	-17.674	4.346
7	W–E	-16.841	5.179
8	E–W	-16.841	5.179
9	W–E	-16.008	6.012
10	E–W	-16.008	6.012
11	W–E	-15.175	6.845
12	E–W	-15.175	6.845
13	W–E	-14.342	7.678
14	E–W	-14.342	7.678
15	W–E	-13.509	8.511
16	E–W	-13.509	8.511
17	W–E	-12.676	9.344
18	E–W	-12.676	9.344
19	W–E	-11.843	10.177
20	E–W	-11.843	10.177
21	W–E	-11.01	11.01

Pass Sequence	Direction	Carriage Centerline Location (ft)	
		North	South
22	E–W	-11.01	11.01
23	W–E	-10.177	11.843
24	E–W	-10.177	11.843
25	W–E	-9.344	12.676
26	E–W	-9.344	12.676
27	W–E	-8.511	13.509
28	E–W	-8.511	13.509
29	W–E	-7.678	14.342
30	E–W	-7.678	14.342
31	W–E	-6.845	15.175
32	E–W	-6.845	15.175
33	W–E	-6.012	16.008
34	E–W	-6.012	16.008
35	W–E	-5.179	16.841
36	E–W	-5.179	16.841
37	W–E	-4.346	17.674
38	E–W	-4.346	17.674
39	W–E	-3.513	18.507
40	E–W	-3.513	18.507
41	W–E	-2.68	19.34
42	E–W	-2.68	19.34

W = West, E = East

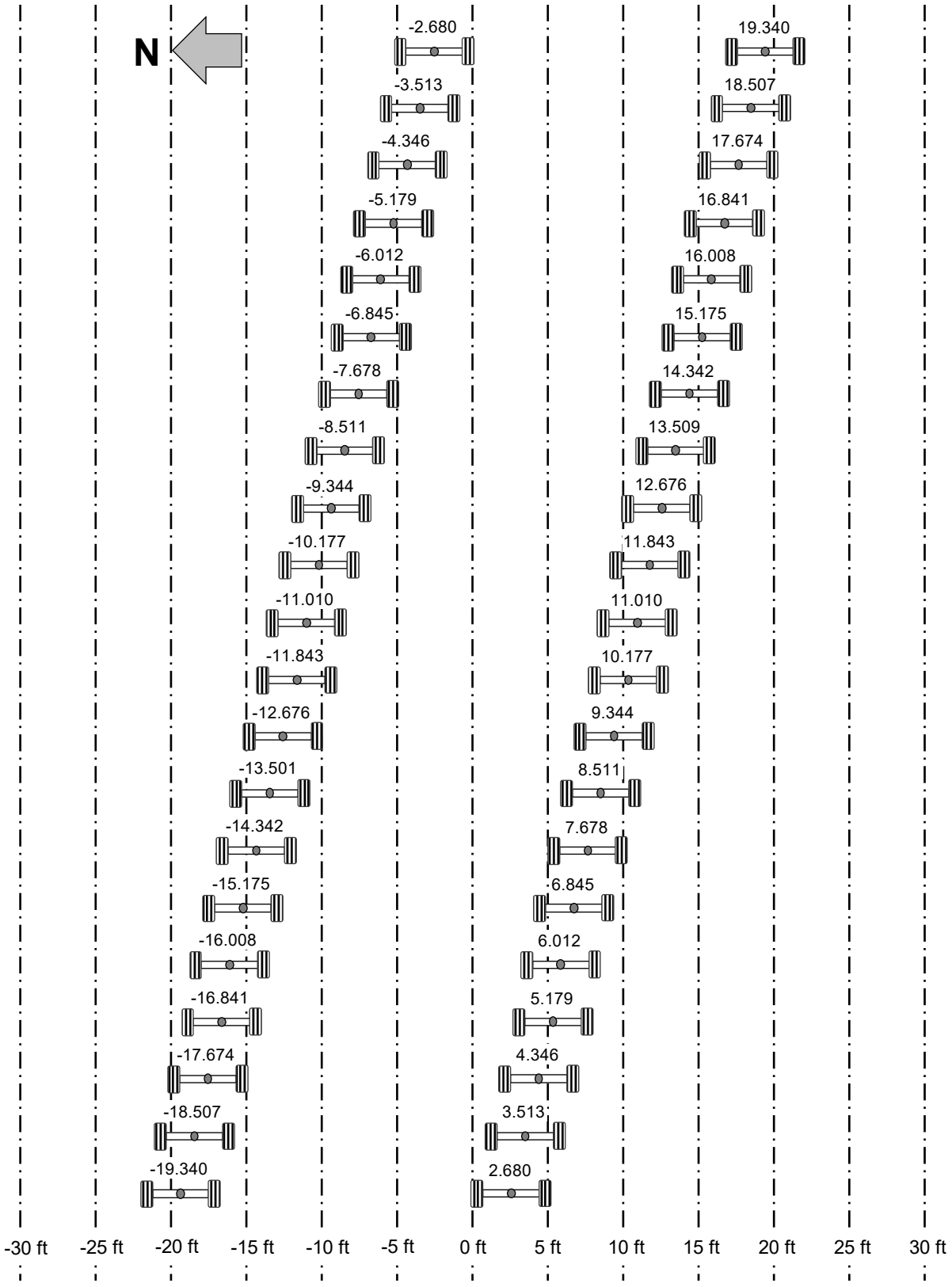

Figure 25. Carriage Positions for Each Pass of Proof-Roll Wander

4.2.2 Ramp-up Response Test

Following proof roll, a ramp-up response test was conducted on March 8, 2021. The purpose of the ramp-up test was twofold:

- Confirm the suitability of planned wheel loads to fail the test items within a reasonable time.
- Adjust planned wheel loads for the main traffic test in case of significant discrepancies between measured in situ and predicted responses.

The test was conducted on test item LFC-5N using a D gear configuration. The vehicle speed was 2.5 mph, and the nominal tire pressure was 255 psi throughout the test. The test was conducted using the following test procedure:

1. Traffic the entire length of the LFC-5N on Track 0 (test item center line at offset -15 ft) using the above parameters. Traffic in both directions ("west to east" and "east to west") at an initial wheel load of 16,000 lb.

2. After trafficking in both directions, check the test item for damage. Had any significant damage (e.g., surface rut and cracks) been observed at this stage, the ramp-up test would have been terminated. However, no damage was observed.

3. Monitor the total vertical strain from CS pair CS-LFC5N-3/4 for any indication of disproportionate damage to the subgrade. In addition, monitor unrecoverable strains (i.e., the difference between left and right offset on the response curve) between load increments.

4. Increase the wheel load in 5,000-lb increments. Repeat steps 2 through 4 until either (a) damage is observed in the CS pair response or (b) the wheel load reaches 56,000 lb. In execution, the load reached the target 56,000 lb with no damage observed.

4.2.3 Baseline Nondestructive Testing

Pre-traffic nondestructive testing (NDT) and characterization consisted of four elements:

1. HWD to obtain back-calculated layer moduli and verify construction uniformity;

2. PSPA measurements to obtain in situ HMA layer modulus;

3. Initial transverse profile measurements using a straight edge following ASTM E1703, to identify pre-existing surface ruts;

4. Laser scanning of the entire pavement surface using a Leica Model P20 360° laser scanner.

Four sets of HWD and PSPA tests were conducted on the untrafficked pavement surface, as follows:

- The initial set of baseline testing was conducted before any other pre-traffic activities. In addition to uniformity tests, HWD drops were conducted at selected sensor locations (PCs and CSs) to verify instrumentation response.

- Set No. 2 was performed during the slow-roll response test.
- Set No. 3 was conducted post-proof roll.
- Set No. 4 was conducted just before the start of the traffic test.

HWD and PSPA tests were conducted at six locations in each test item, as shown in Figure 26. Test locations were marked on two transverse lines located at the third points of the test item, so that the tests covered the instrumented area. The offsets 15 feet left and right of the facility centerline aligned with the center of traffic for the north and south test items, respectively. The ±5- and ±25-foot transverse offsets aligned with the untrafficked areas of the test items.

For test items LFC-5N and LFC-5S, HWD testing was conducted with a four-drop loading sequence beginning with an approximate 24,000-lb seating load. Subsequent loads were approximately 6,000 lb, 12,000 lb, and 24,000 lb.

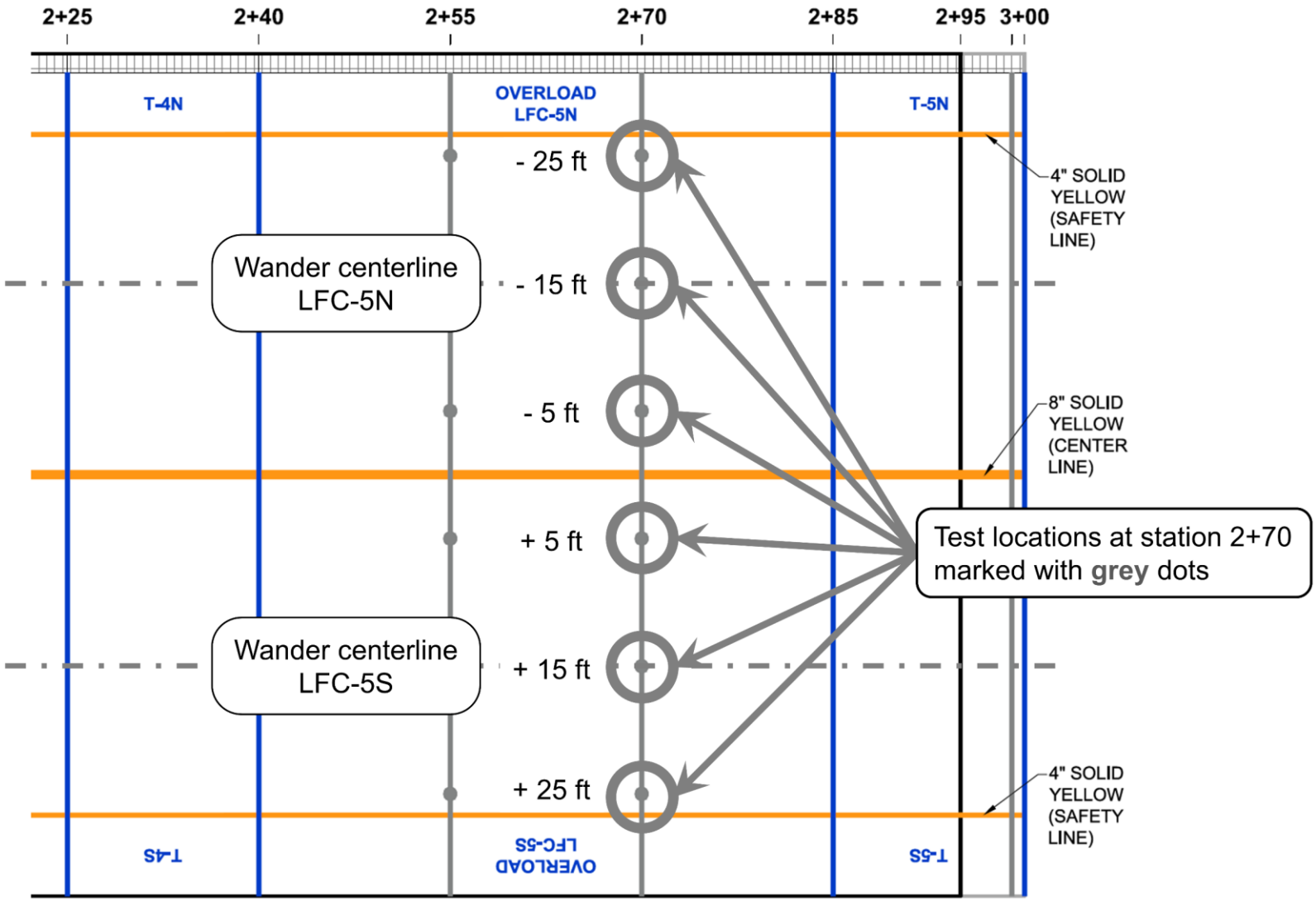

Figure 26. Heavy Weight Deflectometer and PSPA Test Locations in Overload Test Items

4.3 TRAFFIC TESTS

4.3.1 Traffic Loading Sequence

Wheel loads (normal and overload) were based on FAARFIELD computations as shown in Table 9. The vehicle speed was 2.5 mph for the duration of the test. Traffic testing followed the procedure below:

1. Apply overload to north test item. Traffic test item LFC-5N only for a full wander sequence (66 passes) using the D gear at a target wheel load of 57,000 lb and 255 psi tire pressure. Measure transverse profiles before and after the wander to determine the accumulated surface rut and any upheaval. Carefully monitor the vertical strains at the top of subgrade as measured by coil sensor pairs.

2. Apply normal loads to both test items. Upon completion of step 1, traffic test items LFC-5N and LFC-5S at the "normal" wheel load of 36,000 lb and 200 psi tire pressure. Continue traffic until pavement failure is observed in both test items. The failure criteria are discussed in Section 4.3.3 .

3. Intervals between rut measurements. During "normal" load traffic, determine the rate of surface rut and upheaval accumulation from transverse profiles. At the beginning of "normal," take physical straight edge measurements after every 66 passes (1 wander sequence), until the rate of rut accumulation stabilizes. After stabilization, reduce the frequency of rut measurements to the end of each day's trafficking. At intervals, compare physical straight edge measurements to laser scan data for quality control.

This procedure sequence was followed in practice; however, at the end of 16,500 passes, there was still no evidence of incipient failure as defined in Section 4.3.3 in either test item. Therefore, a second set of overload passes was applied to LFC-5N, followed by a resumption of normal traffic. Likewise, a third set of overload passes was applied after 24,288 additional passes, again followed by a resumption of normal traffic. The final traffic history including all overloads is given in Section 4.3.4 .

4.3.2 Wander Pattern

The wander pattern consists of 66 passes arranged in 9 wheel tracks, as shown in Table 11 and Figure 27. Passes were in both directions, west-to-east (odd) and east-to west (even). The even-numbered (return) pass is always along the same track as the preceding odd-numbered pass, but in the opposite direction. The complete wander pattern is detailed in Table 12.

Table 11. Construction Cycle 9 Traffic Wander Wheel Track Locations

Track No.	Carriage Centerline Location, ft	
	North	South
-4	-18.412	11.588
-3	-17.559	12.441
-2	-16.706	13.294
-1	-15.853	14.147
0	-15.000	15.000
1	-14.147	15.853
2	-13.294	16.706
3	-12.441	17.559
4	-11.588	18.412

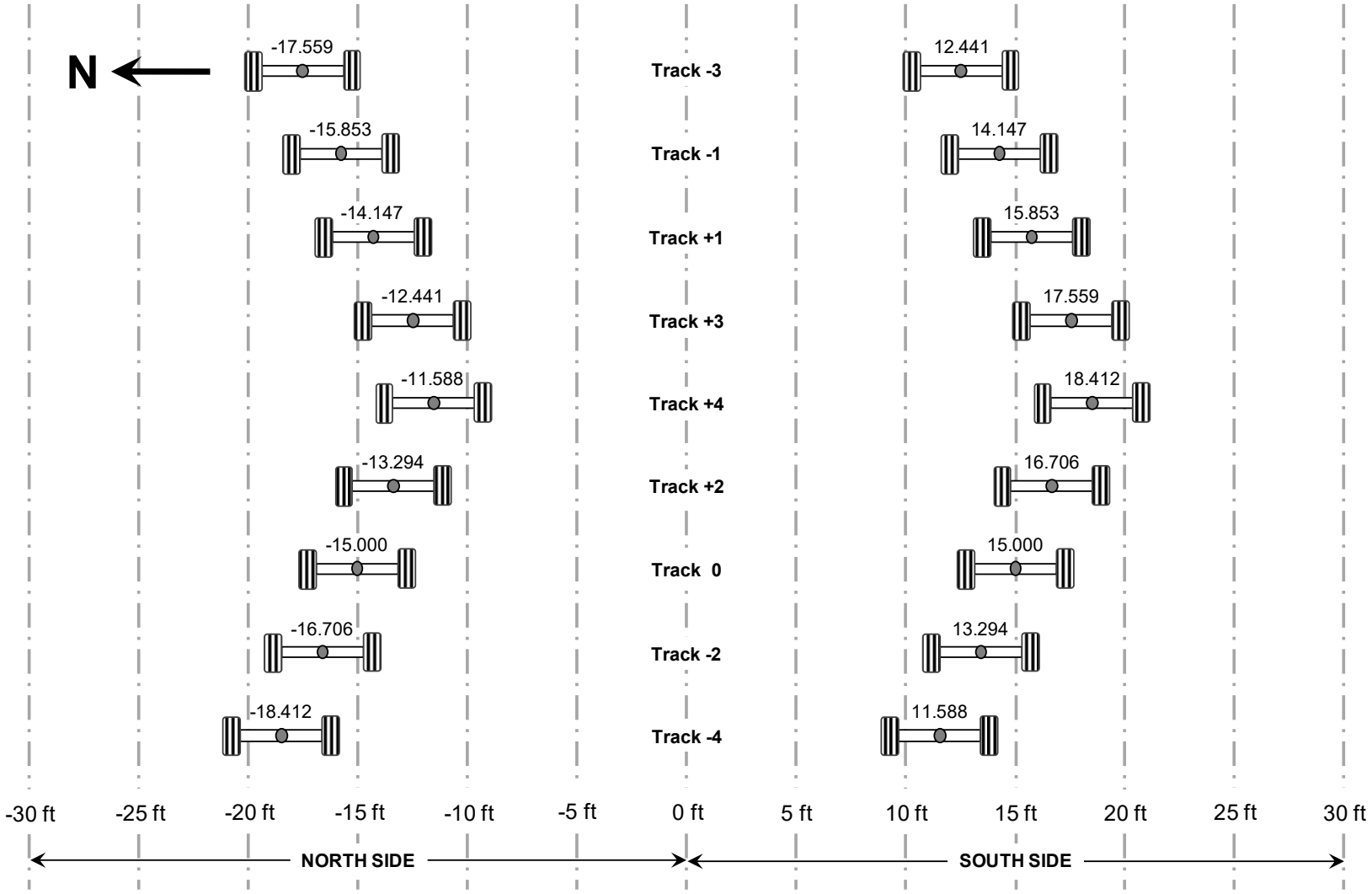

Figure 27. Construction Cycle 9 Traffic Wander Wheel Tracks

Table 12. Construction Cycle 9 Complete Wander Sequence

Pass Sequence	Direction	Track No.	Carriage Centerline Location (ft)	
			North	South
1	W–E	-4	-18.412	11.588
2	E–W	-4	-18.412	11.588
3	W–E	-2	-16.706	13.294
4	E–W	-2	-16.706	13.294
5	W–E	0	-15.000	15.000
6	E–W	0	-15.000	15.000
7	W–E	2	-13.294	16.706
8	E–W	2	-13.294	16.706
9	W–E	4	-11.588	18.412
10	E–W	4	-11.588	18.412
11	W–E	3	-12.441	17.559
12	E–W	3	-12.441	17.559
13	W–E	1	-14.147	15.853
14	E–W	1	-14.147	15.853
15	W–E	-1	-15.853	14.147
16	E–W	-1	-15.853	14.147
17	W–E	-3	-17.559	12.441
18	E–W	-3	-17.559	12.441
19	W–E	-4	-18.412	11.588
20	E–W	-4	-18.412	11.588
21	W–E	-2	-16.706	13.294
22	E–W	-2	-16.706	13.294
23	W–E	0	-15.000	15.000
24	E–W	0	-15.000	15.000
25	W–E	2	-13.294	16.706
26	E–W	2	-13.294	16.706
27	W–E	4	-11.588	18.412
28	E–W	4	-11.588	18.412
29	W–E	3	-12.441	17.559
30	E–W	3	-12.441	17.559
31	W–E	1	-14.147	15.853
32	E–W	1	-14.147	15.853
33	W–E	-1	-15.853	14.147
34	E–W	-1	-15.853	14.147
35	W–E	-3	-17.559	12.441
36	E–W	-3	-17.559	12.441
37	W–E	3	-12.441	17.559
38	E–W	3	-12.441	17.559
39	W–E	1	-14.147	15.853
40	E–W	1	-14.147	15.853
41	W–E	-1	-15.853	14.147
42	E–W	-1	-15.853	14.147
43	W–E	-3	-17.559	12.441
44	E–W	-3	-17.559	12.441
45	W–E	-2	-16.706	13.294
46	E–W	-2	-16.706	13.294
47	W–E	0	-15.000	15.000
48	E–W	0	-15.000	15.000
49	W–E	2	-13.294	16.706
50	E–W	2	-13.294	16.706
51	W–E	-2	-16.706	13.294
52	E–W	-2	-16.706	13.294
53	W–E	0	-15.000	15.000
54	E–W	0	-15.000	15.000
55	W–E	2	-13.294	16.706
56	E–W	2	-13.294	16.706
57	W–E	1	-14.147	15.853
58	E–W	1	-14.147	15.853
59	W–E	-1	-15.853	14.147
60	E–W	-1	-15.853	14.147
61	W–E	1	-14.147	15.853
62	E–W	1	-14.147	15.853
63	W–E	-1	-15.853	14.147
64	E–W	-1	-15.853	14.147
65	W–E	0	-15.000	15.000
66	E–W	0	-15.000	15.000

W = West, E = East

4.3.3 Failure Criteria

Ahlvin et al. (1971) defined failure as the earlier of:

(i) Surface upheaval of the pavement adjacent to the traffic wander exceeded 1 in. or
(ii) Surface cracking so severe that the pavement no longer remained waterproof.

The same failure criteria were adopted in all preceding construction cycles.

4.3.4 Traffic History

Table 13 lists the key events during CC9 trafficking with dates. Traffic on the overload test items LFC-5N/S is highlighted in yellow.

Table 13. Construction Cycle 9 Traffic Summary

Dates	Passes on Test Items			Load Description
	LFS-1/2	LFC-3/4	LFC-5	
4/5/2021–6/3/2021	5,544	5,544	0	Traffic test items 1-4
7/1/2021	0	0	66	1st Overload LFC-5N
7/1/2021–7/28/2021	0	0	5,478	Traffic LFC-5 only
8/2/2021–10/14/2021	7,066	7,066	7,066	Traffic all test items
10/15/2021–2/21/2022	0	0	0	Vehicle down for maintenance
2/22/2022–3/28/2022	3,956	3,956	3,956	Resume traffic all test items
3/29/2022	0	0	66	2nd overload LFC-5N
3/29/2022–10/5/2022	24,354	24,354	24,288	Traffic all test items
10/12/2022	0	0	396	3rd overload LFC-5N
10/13/2022–12/21/2022	0	0	15,312	Traffic LFC-5 only
1/3/2023–3/29/2023	13,728	0	0	Traffic test items LFS-1/2
1/25/2024–4/2/2024	204,60	0	0	Traffic test items LFS-1/2
Total	75,108	40,920	56,628	

4.3.5 Routine Monitoring and Testing

4.3.5.1 Dynamic Responses

Dynamic responses are sensor responses triggered by an NAPTV pass. Dynamic responses included

- horizontal strains (bottom of HMA layer);
- permanent deformations from CSs; and
- vertical stresses from PCs.

4.3.5.2 Static Responses

Static sensor responses were collected hourly. Static sensor responses included temperature and moisture data. Subgrade MS record volumetric MC. Volumetric MC measured with the embedded gauges may be converted to gravimetric moisture content using the formula:

$$w = M.C.\times \frac{\rho_{water}}{\rho_{soil}} \quad (8)$$

where:

w = gravimetric MC,
ρ_{water} = water density , and
ρ_{soil} = laboratory-determined dry density of subgrade soil (as listed in Table 7).

4.3.5.3 Manual Distress Survey

Visual distress surveys were performed daily in accordance with ASTM D5340 (ASTM, 2020), after each day's traffic. In addition to the standard survey data, researchers marked and measured very fine cracks (i.e., those that would be disregarded in a standard condition survey). All cracks were marked on the surface, and the beginning and end coordinates of the cracks were recorded to track their progression. Appendix E presents logs of observed cracks for the CC9 overload test items after the termination of traffic. Researchers prepared detailed reference maps for each inspection, in which the cracks were color-coded, identifying the date each crack was first observed and the associated number of passes. Thus, new crack initiation and propagation of existing cracks were tracked using color-coded maps.

- Crack maps prepared during manual distress surveys were reviewed to track the appearance and progression of cracks. For test items LFC-5N and LFC-5S, the types of cracking observed were alligator cracking in the traffic area and linear (longitudinal) cracking along the outer edges of the traffic area. Quantities of cracking for each test item were measured and added to a test item schematic as they appeared.

- Crack density (CD) is a metric for damage quantification and is defined as the portion of pavement surface that is occupied by distresses. A grid of uniform elements or units was established for each test item. If any portion of a unit is distressed, the entire unit area is considered distressed. The CD area is determined by counting for the number of units exhibiting distresses. Therefore, the accuracy of CD increases with the number of discrete units within the area of interest. Crack measurements with an adequately small unit size can ensure a true representation of the distressed surface. Following CC7 practices in Garg et al. (2020), the CDs of CC9 test items were computed using 1-ft by 1-ft unit size in the traffic area only.

4.3.5.4 Straightedge Rut Measurement

To monitor the accumulation of surface ruts, transverse surface profiles were measured with a 16-ft straightedge in accordance with ASTM E1703 (ASTM, 2015). The maximum rut depth

value along the full length of the beam was measured with a dial gauge and recorded. This measurement was performed at two stations within each test item. Ruts were measured at the end of each trafficking day.

4.3.5.5 Portable Seismic Pavement Analyzer and Heavy Weight Deflectometer Tests

HWD and PSPA tests were conducted at 2-week intervals during traffic to monitor structural changes. HWD testing was conducted with a four-drop loading sequence beginning with a nominal 36,000-lb seating load, followed by 12,000-lb, 24,000-lb, and 36,000-lb (nominal) loads. Deflection basin parameters were normalized to the 36,000-lb load level.

The analysis of HWD data in this report focused on the index called Area Under Pavement Profile (AUPP), alongside linear elastic analysis-based backcalculation. This deflection-based parameter (DBP) is known to correlate well with the temperature variation and increases with the increase in tensile strain beneath the asphalt concrete (Garg, 1997; Hoffman & Thompson, 1981; Kazmee et al., 2022). The AUPP parameter can be defined as follows:

$$AUPP = {}^{1}/_{2} \times \{11D_0 - 2(D_{12} + D_{24} + D_{36} + D_{48} + D_{60}) - D_{72}\} \quad (9)$$

where:

D_0, D_{12}, D_{24}, D_{36}, D_{48}, D_{60}, and D_{72} designate the deflections measured 0, 12, 24, 36, 48, 60, and 72 in. away from the center of HWD loading plate.

Overall, variation in AC temperature was uniform across the test items, as discussed in Section 5. . The ratio of AUPP indices between trafficked and non-trafficked areas should reveal the extent of damage in the individual test items.

4.3.5.6 Three-Dimensional Laser Scanning

Three-dimensional (3-D) laser scanning using a Leica ScanStation P20 was used to track the relative change in surface elevations over time. Light Detection and Ranging (LiDAR) scans were conducted prior to trafficking and during trafficking at a regular interval of 2 weeks to track changes in surface elevation with traffic. For each measurement set, a proprietary design and documentation software (AutoCAD® 3D) was used to generate the Cartesian coordinates from the random 3-D point-cloud elevations. The resulting 1-in. regularly spaced coordinates were then input into a C# programming language-based software (named SurfaceD) to compute a 3-D surface map, transverse profiles, and surface upheaval magnitudes.

5. TEST RESULTS AND DISCUSSION

5.1 SURFACE MONITORING DATA

5.1.1 Upheaval and Rutting

Upheaval is measured relative to the original surface profile. Positive upheaval values greater than approximately 1 in. outside of the trafficked area are associated with subgrade shear failure (Section 4.3.3). Figure 28 shows the evolution of surface upheaval in test items LFC-5N

(overload) and LFC-5S (control). The research team computed values of maximum upheaval at specific stations using an in-house program called the Virtual Upheaval Calculator (VUC), as discussed in Mazzotta et al. (2024). Appendix B gives the computed upheavals and offsets. Figure 28 is annotated to show significant events that affected the observed upheaval trend. The first two overload events (66 passes each) had no discernable influence on upheaval in LFC-5N relative to LFC-5S. The third overload sequence (396 passes) coincided with a marked increase in surface upheaval at STA 2+55 in LFC-5N, but a much smaller increase at STA 2+70.

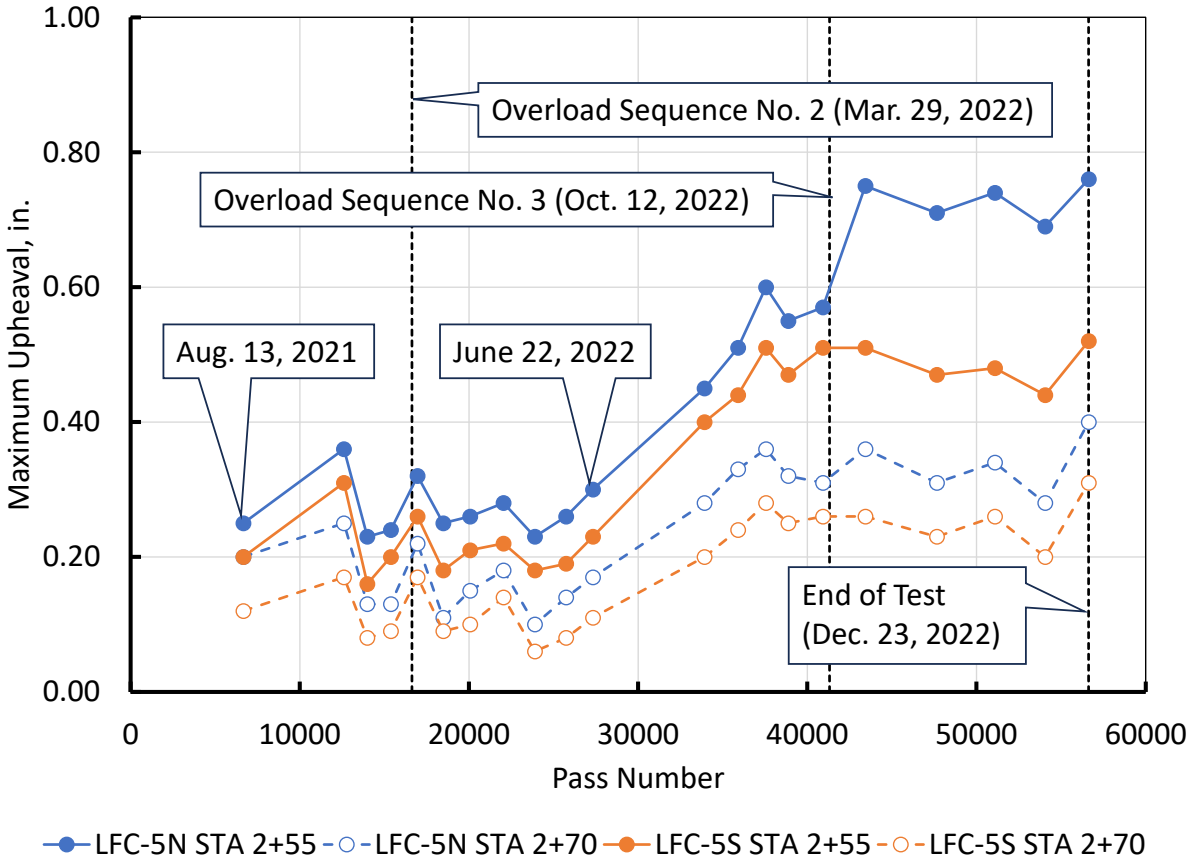

Figure 28. Evolution of Surface Upheaval in Overload Test Items

Ultimately, neither test item reached the 1-in. upheaval threshold for failure. As shown in Figure 28, the largest observed increase in upheaval coincided with higher ambient temperatures during the summer 2022 season. Up to about 25,000 passes, the generally low values of computed upheaval (less than 0.25 in.) can be ascribed to noisy data, or to displacement of asphalt material away from the trafficked area.

Figure 29 shows the growth in accumulated rut with traffic in test items LFC-5N (overload) and LFC-5S (control). The straightedge rut is measured from peak (or more precisely, from a point on a straight line connecting two peaks) to trough in the deformed section. Figure 29 is annotated to show significant events that affected rutting. Neither the first nor the second event of overload wander contributed to more rutting in the north. Up to 40,920 passes, the rutting in LFC-5N was

consistently lower than in LFC-5S. However, following the third overload sequence, the accumulated rut in LFC 5N increased and exceeded that in LFC-5S. Despite this one-time increase in rut depth, the rate of rutting remained unchanged after the third overload. Increased rutting in both test items coincided with the summer 2022 season and higher temperatures. Furthermore, extensive cracking damage in both test items adversely affected the structural integrity of the pavements, which accelerated rutting.

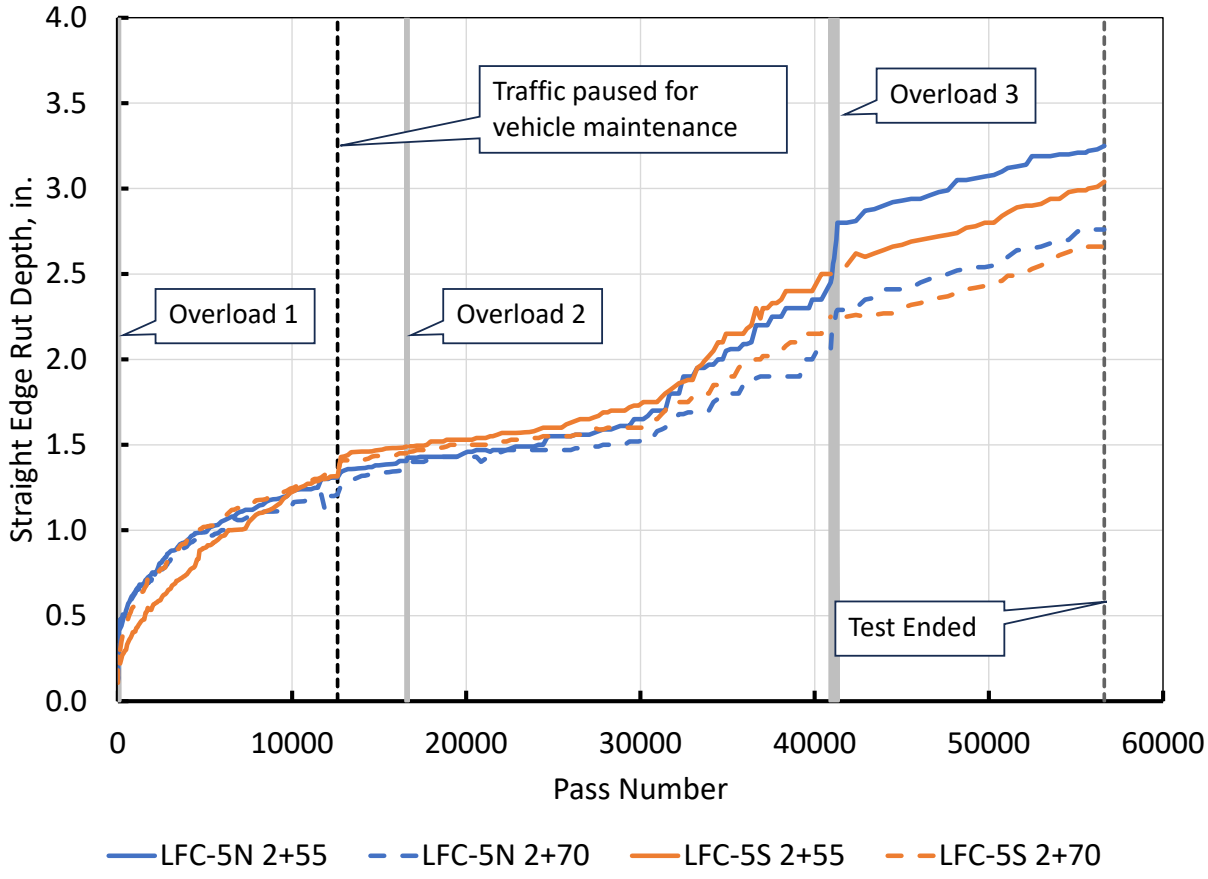

Figure 29. Rut Accumulation in the Overload Test Items Measured with Straightedge

5.1.2 Cracking

Figure 30 plots the cracked surface area versus traffic passes. Areas of alligator cracking and longitudinal/transverse (L/T) cracking were counted. No significant areas of cracking were observed until after the second overload event. Substantial increases in CDs occurred in both test items after the second overload. Although CD after the second overload was not greater for LFC-5N, the overload possibly contributed to higher crack severity in the overloaded test item, as discussed below. After about 27,000 passes, monitoring was primarily for loose aggregates, as the cracked area remained nearly constant. Following the third overload, the cracked area in LFC-5N increased relative to LFC-5S. (Note: Figure 30 shows a drop in the distressed area in

LFC-5N at about 43,000 passes. This anomaly is attributed to a change in visual inspection personnel that took place at that time and shows how human factors can influence the analysis.)

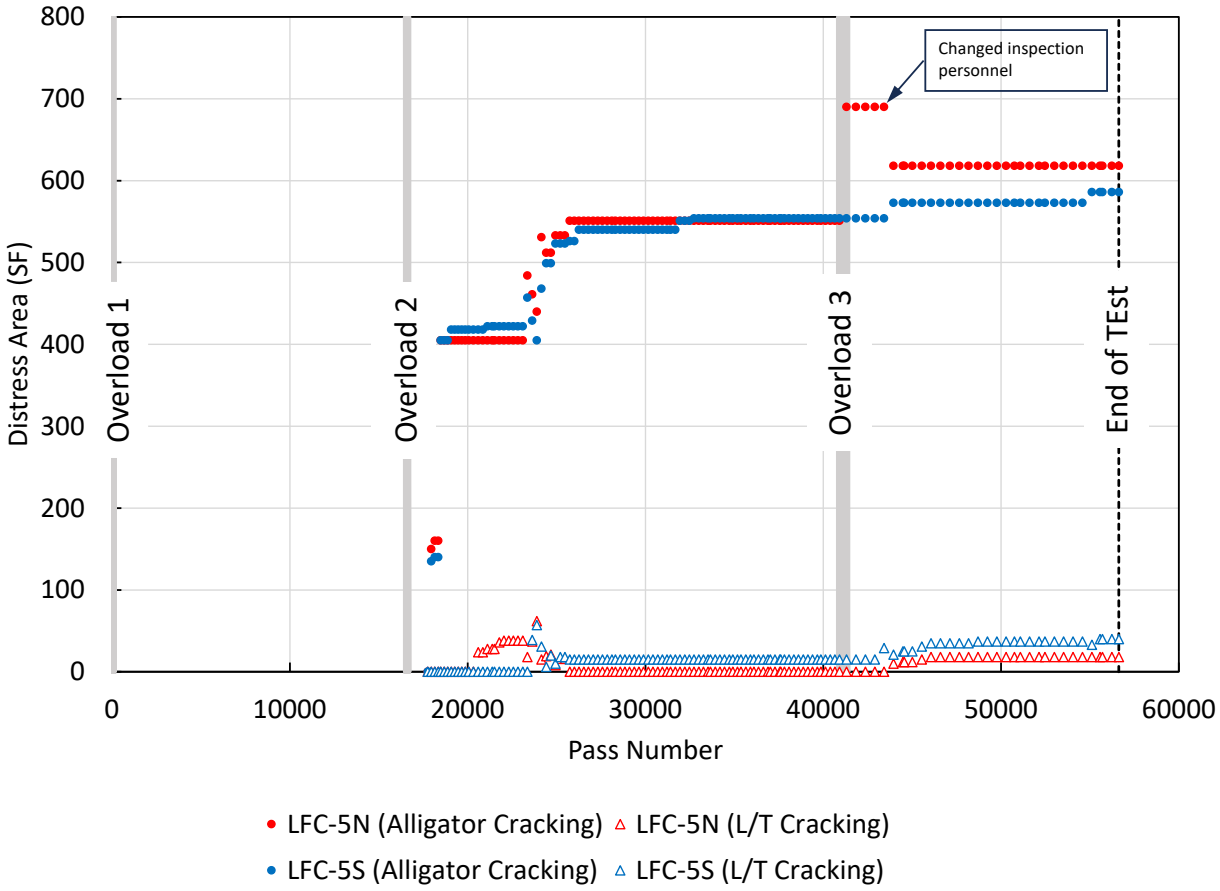

Figure 30. Variation of Crack Densities with Traffic in Test Items LFC-5N and LFC-5S

Figure 31 and Figure 32 show cracking distresses in LFC-5N and LFC-5S respectively at 18,480 passes (after the application of the second overload on LFC-5N). Different colors represent different severity levels. As shown in Figure 30, CDs in both test items increased significantly after the second overload as the distress evolved from a hairline pattern to fully discernible alligator cracking, but the appearance of cracking was different in the two test items. LFC-5S (no overload) had interconnected longitudinal cracks distributed over the full traffic width. In contrast, LFC-5N (overload) had a higher density of alligator cracks in the corresponding area.

Due to extensive surface cracking, neither test item would have remained waterproof after only 18,480 passes. Both test items could be presumed to fail by the criterion of loss of waterproofing (see Section 4.3.3).

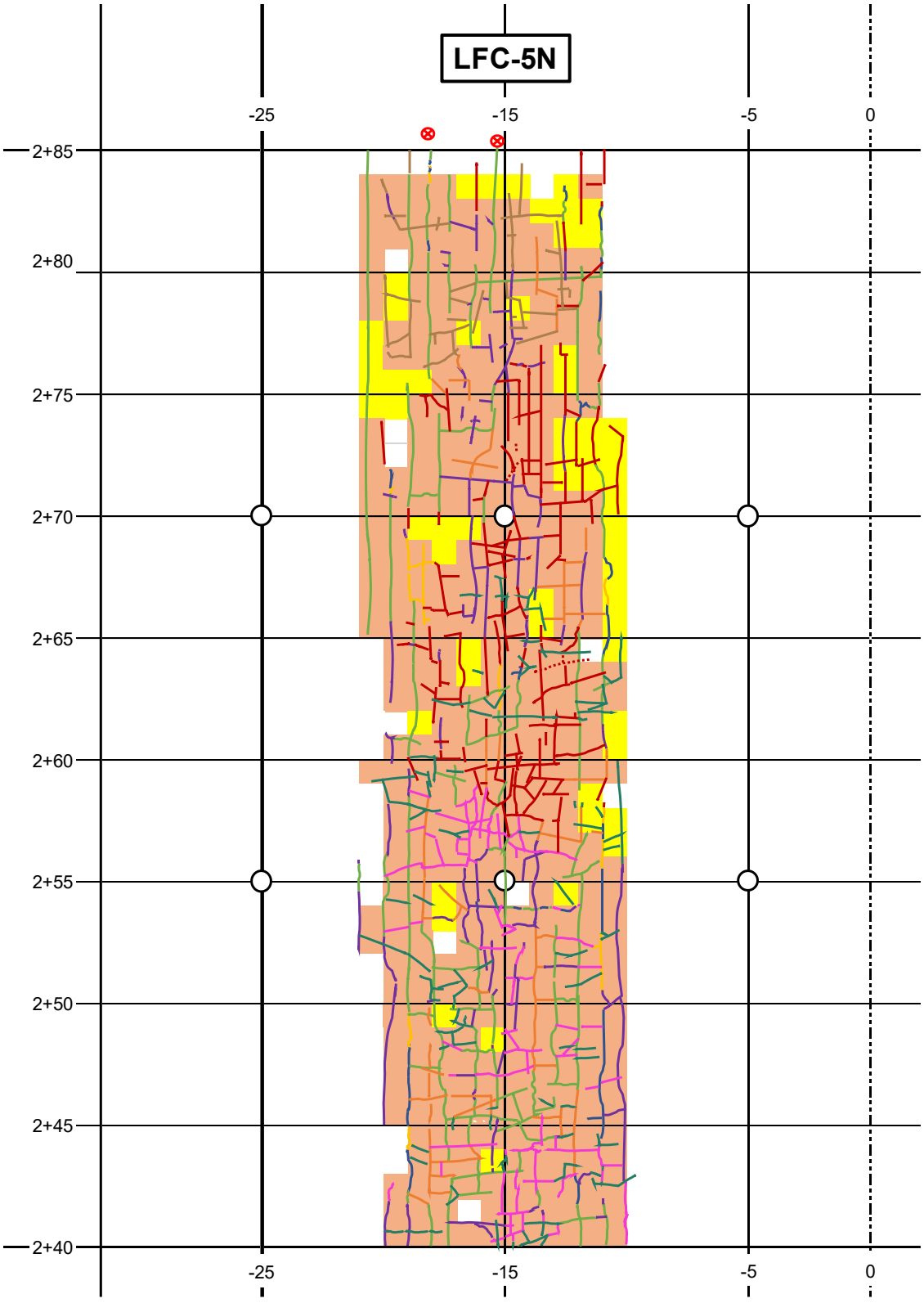

Figure 31. Cracking Densities in Overload Test Item LFC-5N at 18,480 Passes
(Brown represents areas of medium severity; yellow represents high severity.)

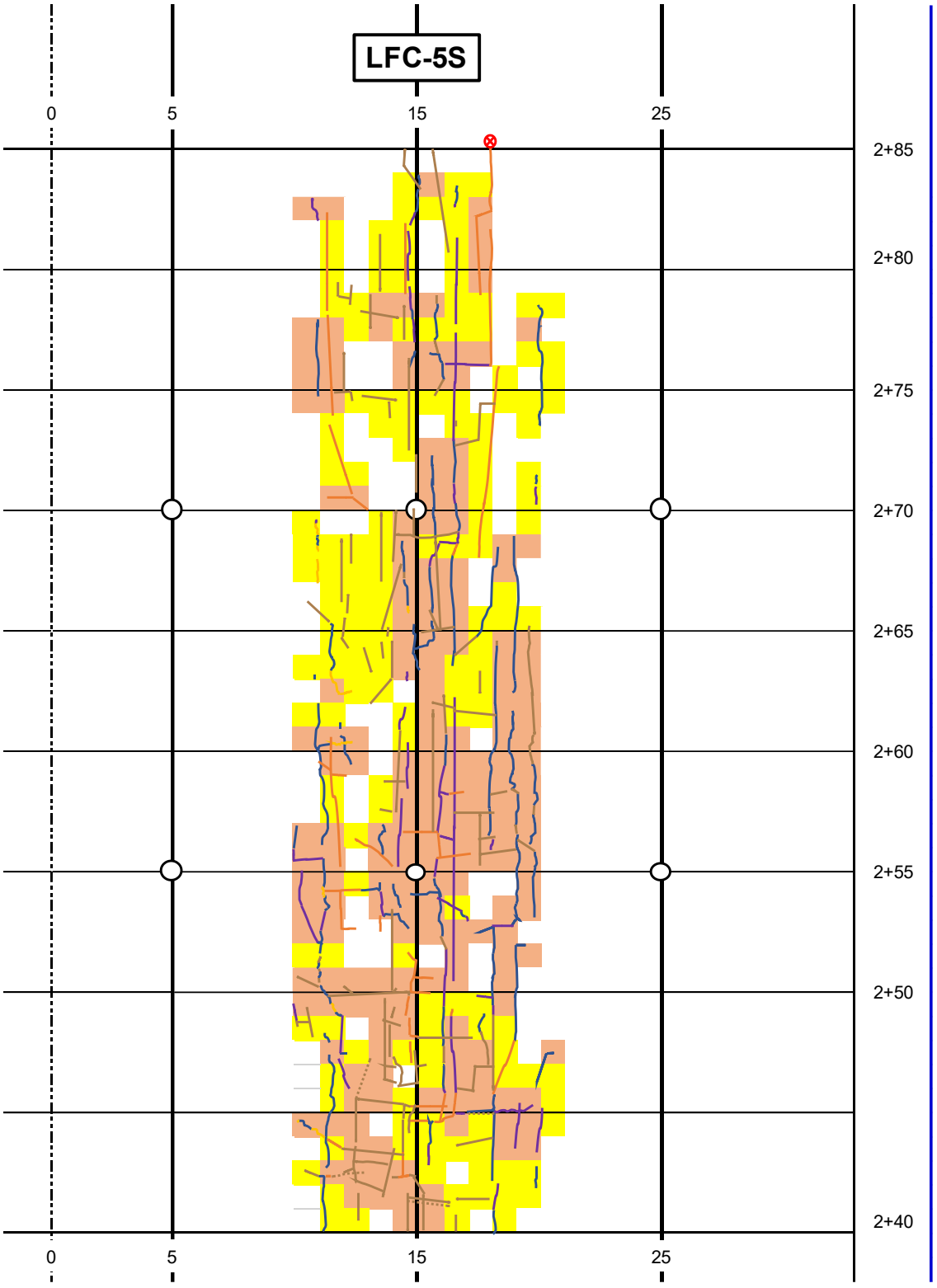

Figure 32. Cracking Densities in Control Test Item LFC-5S at 18,480 Passes
(Brown represents areas of medium severity; yellow represents high severity.)

5.2 SENSOR RESPONSE DATA

5.2.1 Asphalt Sensors

Asphalt instrumentation consisted of longitudinal strain gauges (LSGs), transverse strain gauges (TSGs), and thermocouples. Figure 33 shows the difference in peak tensile strain (TSG-LFC5N-2), depending on whether the vehicle was moving from east to west (E→W) or from west to east (W→E). The phenomenon of higher peak strain on W→E passes versus E→W was consistent for all functional ASGs in both test items and was expected because of how peak load-induced strains are computed. Peak strains are calculated relative to the average value of unloaded strain just before the wheel loading event (the "left offset"). Because the return (E→W) pass immediately follows and is always on the same path as the W→E pass, the baseline strain has not had time to recover fully to a preload state, as it has for the W→E pass (which is never on the same track as the previous pass). Considering this, the following discussion on strain focuses only on the W→E passes.

Figure 34 through Figure 37 show peak strain at the bottom of the asphalt as a function of test item pass number and asphalt temperature. Figure 34 and Figure 35 show LSG, and Figure 36 and Figure 37 show TSG. All strain gauges exhibited high variability, which can be attributed to many factors including temperature, load history (wander), and sensor damage. In general, peak tensile strains are expected to increase with temperature. The lower plots in Figure 34 through Figure 37 confirm that this is generally the case for LSGs. However, TSGs in LFC-5N exhibited a small decreasing trend in response to increasing temperature, while peak strains in LFC-5S were essentially constant with respect to asphalt temperature. However, these trends were small compared to the overall variability in peak strain gauge responses.

Thermocouple trees consisting of four temperature probes at various depths were installed in LFC-5N. Figure 38 plots asphalt temperature versus number of passes for LFC-5N. The plot shows the strong seasonal variation in asphalt temperature at all embedment depths. The temperature gradient through the asphalt thickness was small.

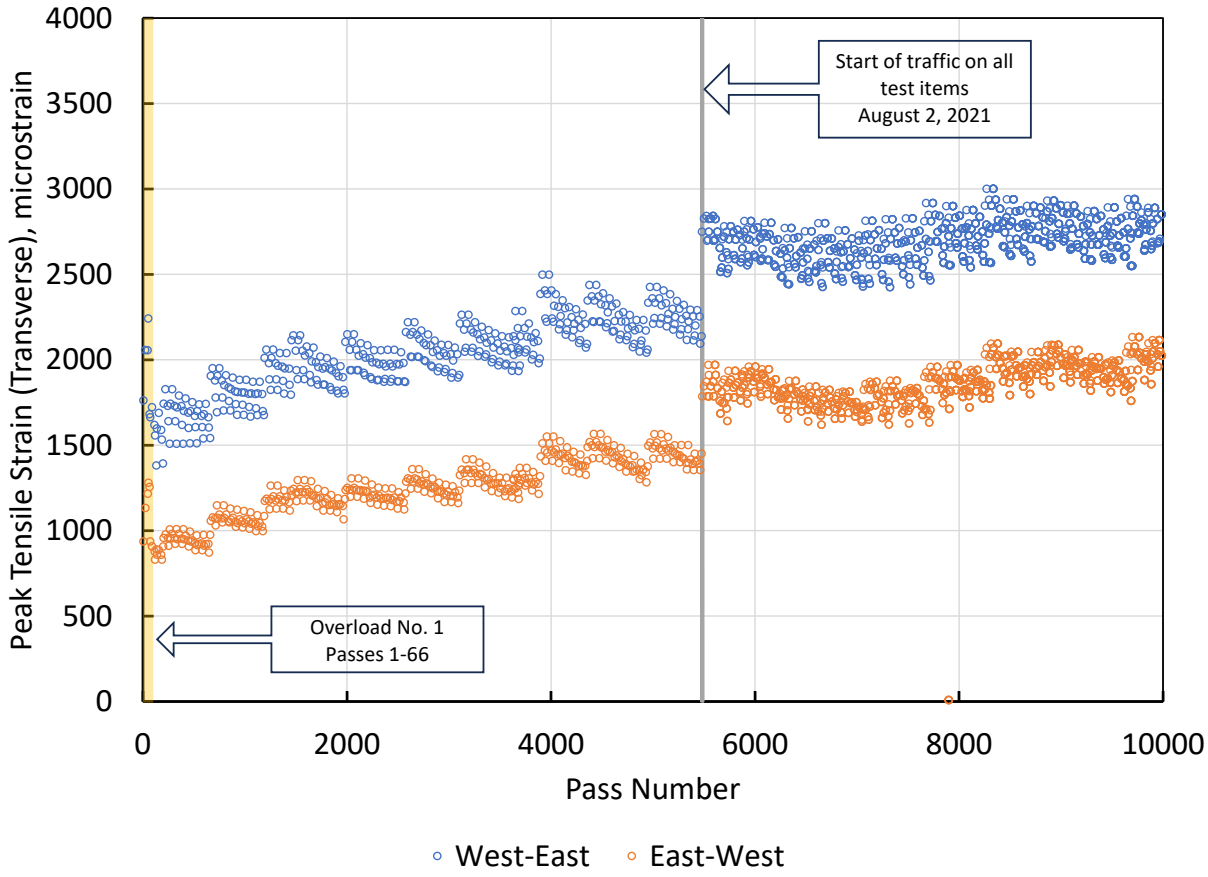

Figure 33. Peak Transverse Tensile Strain Response by Direction of Traffic (TSG-LFC5N-2)

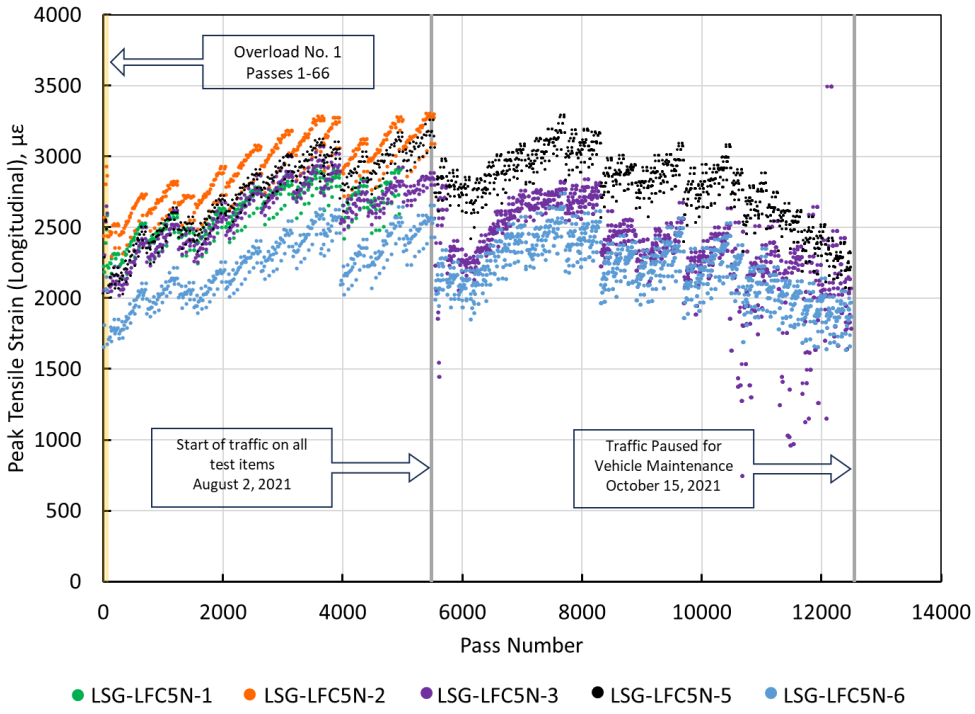

(a)

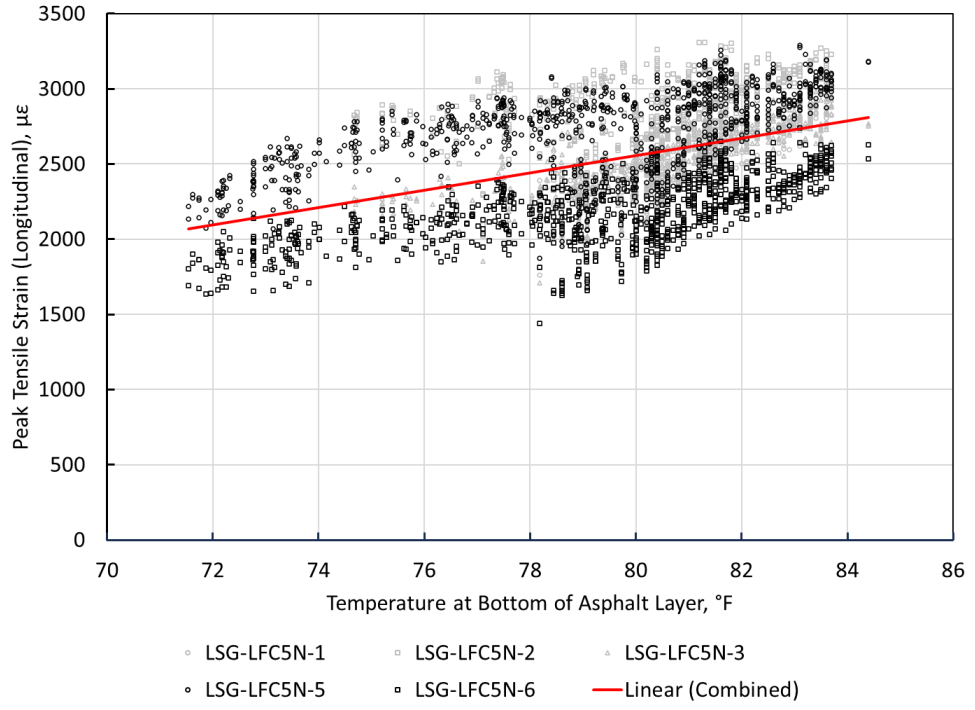

(b)

Figure 34. Variation of Peak Longitudinal Tensile Strain in Test Item LFC-5N with (a) Pass Number and (b) Asphalt Temperature

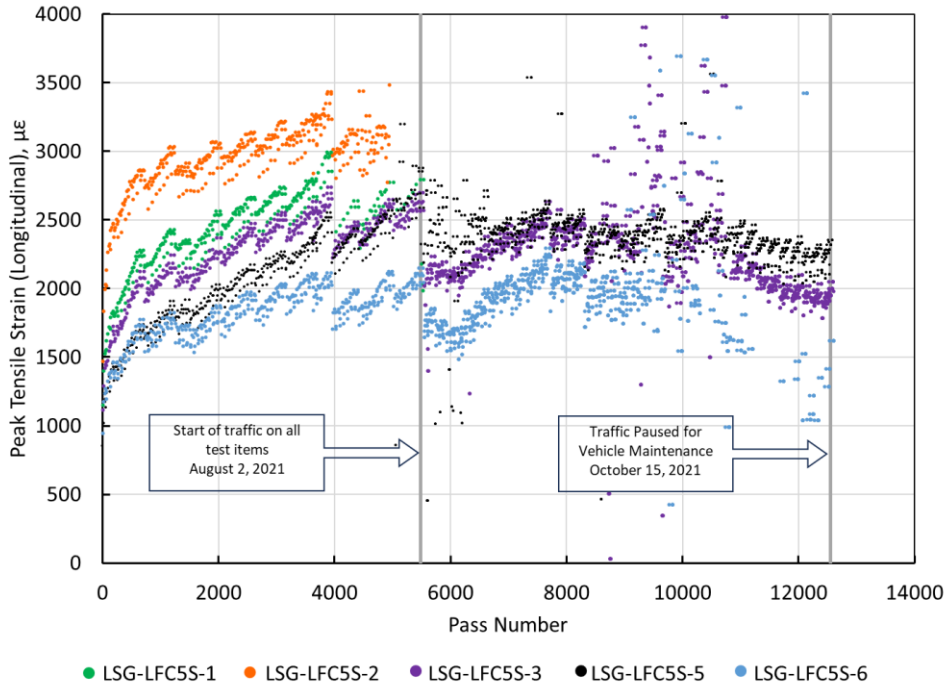

(a)

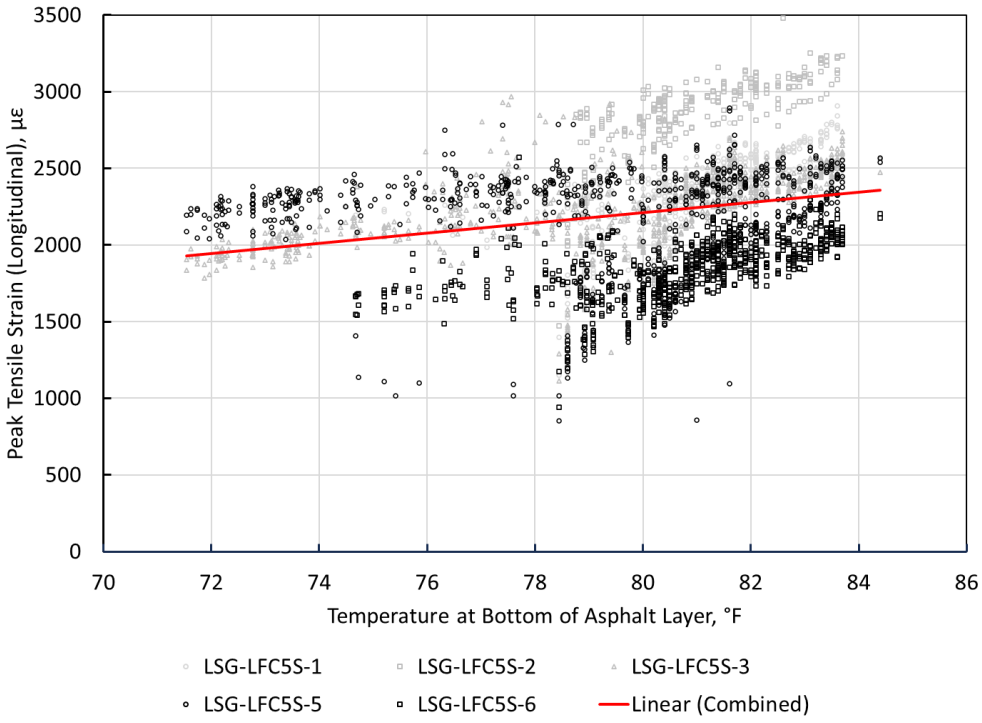

(b)

Figure 35. Variation of Peak Longitudinal Tensile Strain in Test Item LFC-5S with (a) Pass Number and (b) Asphalt Temperature

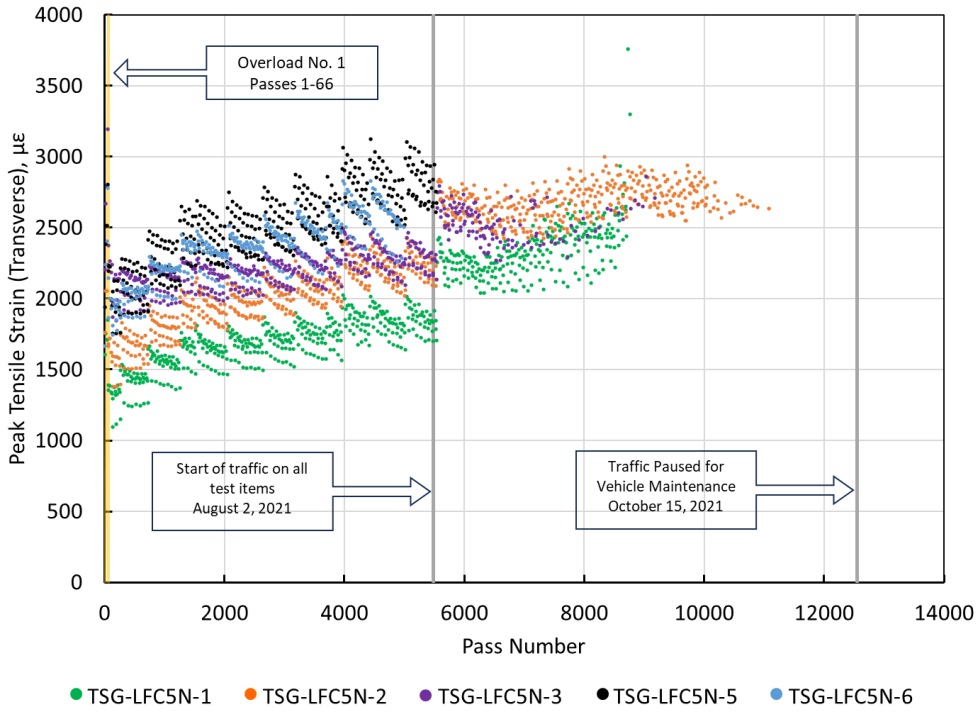

(a)

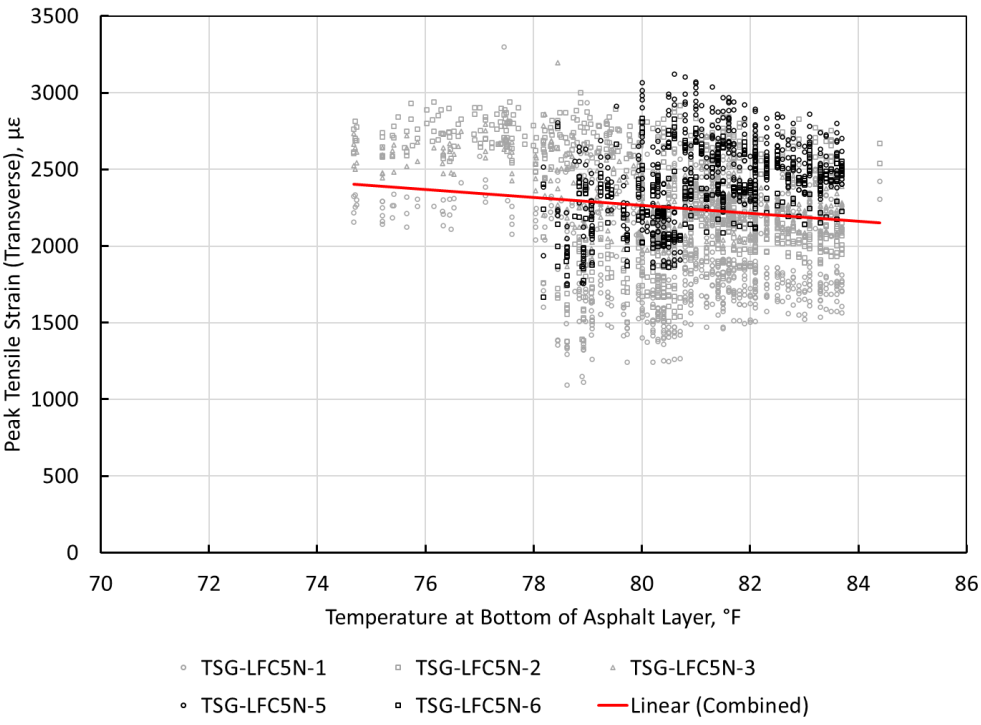

(b)

Figure 36. Variation of Peak Transverse Tensile Strain in Test Item LFC-5N with (a) Pass Number and (b) Asphalt Temperature

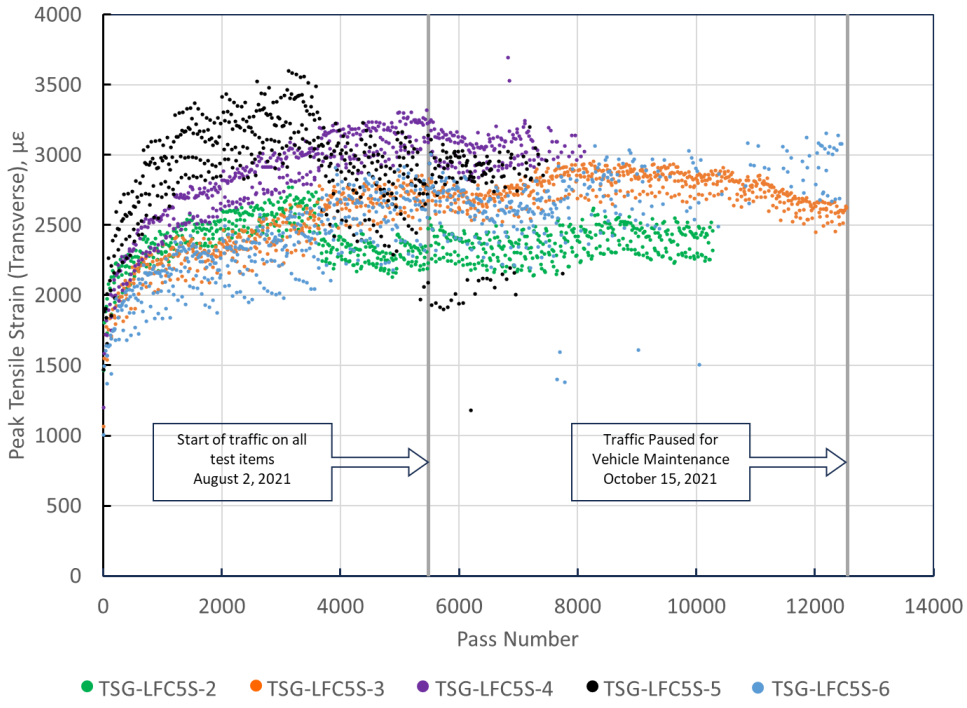

(a)

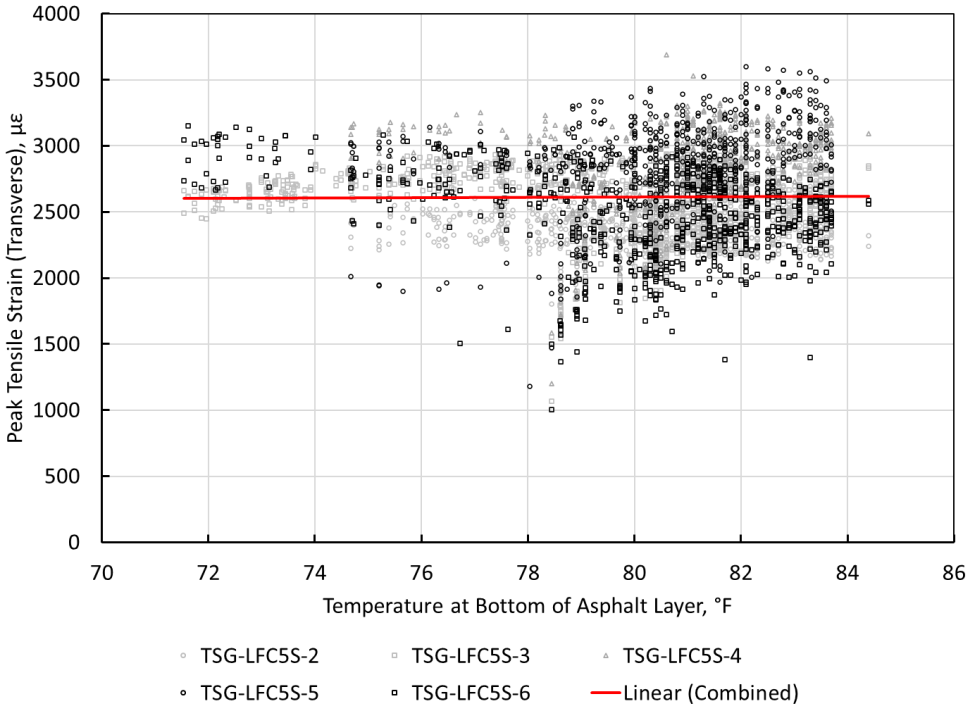

(b)

Figure 37. Variation of Peak Transverse Tensile Strain in Test Item LFC-5S with (a) Pass Number and (b) Asphalt Temperature

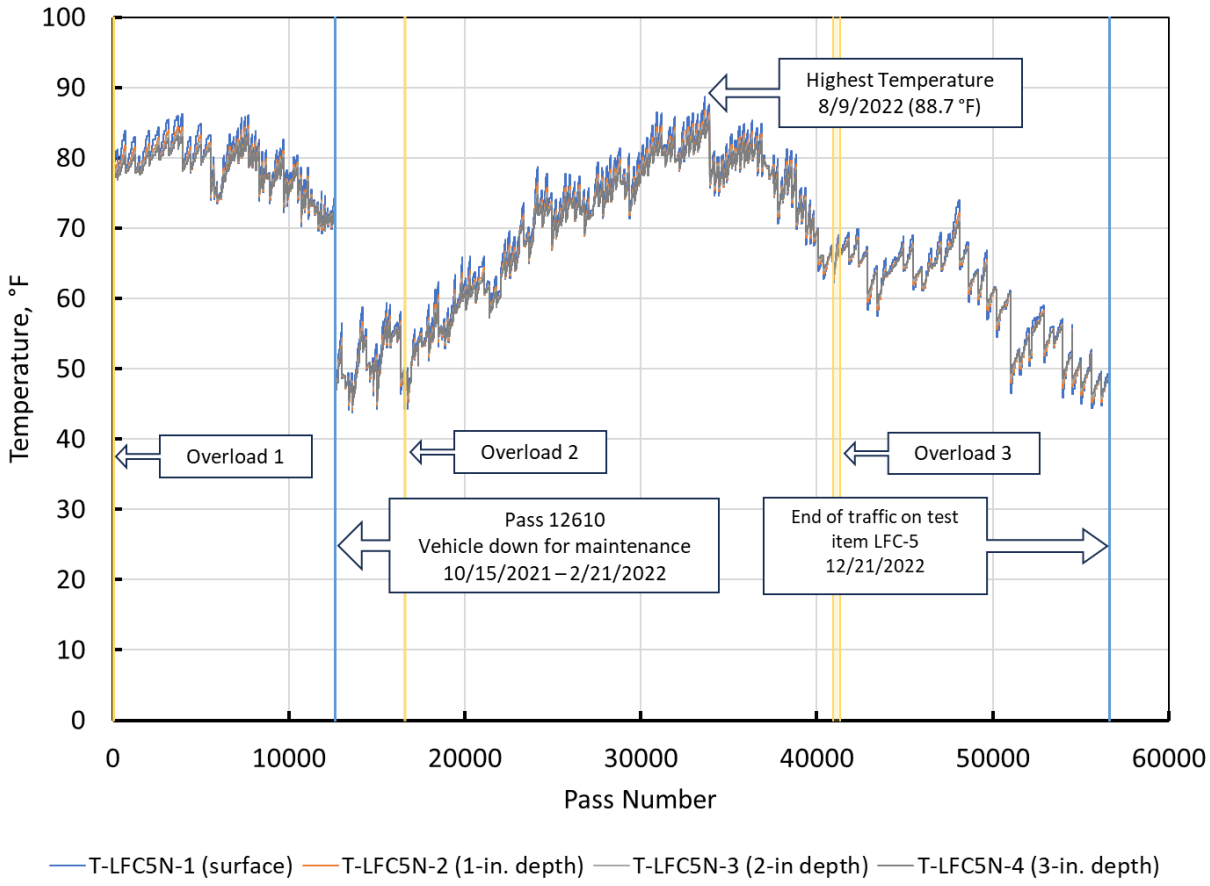

Figure 38. Variation of Asphalt Concrete Temperature with Pass Number for Test Item LFC-5N

5.2.2 Subbase Sensors

Two PCs (one in each test item) recorded vertical compressive stress at the top of the P-154 subbase. Figure 39 shows peak stress versus pass number. The effect of overload could not be determined since the PC on the south test item (PC-LFC5S-1) failed after about 32,500 passes. PC-LFC5N-1 continued to record data until the end of the test. As shown in Figure 39, PC-LFC5N-1 showed a noticeable increase in load-induced stress during the third overload sequence, but only for Track 3. PCs were rated for 55 psi and were expected to accommodate stresses up to 50% higher (83 psi). Figure 39 shows that the PCs experienced actual peak stresses up to 90 psi; however, no evidence of saturation was seen in the peak PC responses. Nevertheless, overstressing could have contributed to the failure of PC-LFC5S-1.

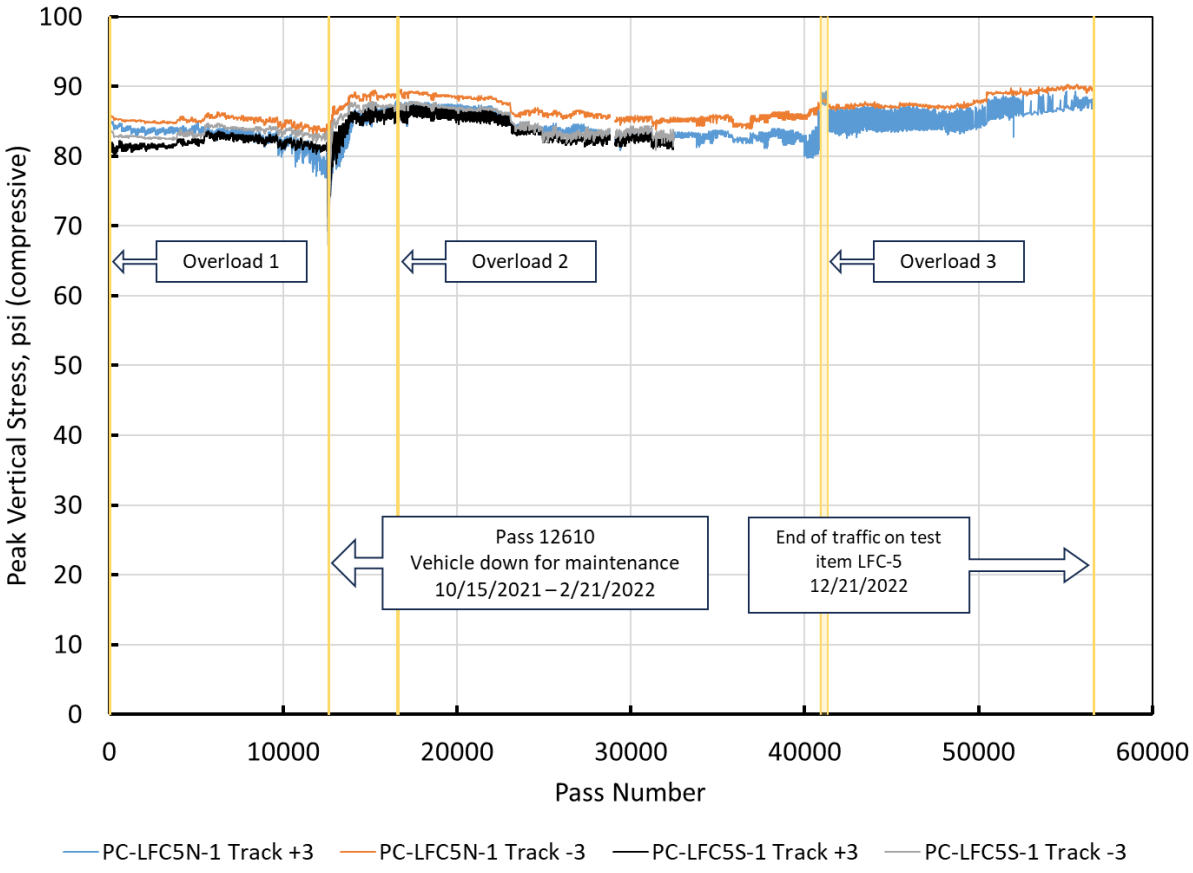

Figure 39. Peak Vertical Compressive Stress at Top of P-154 Subbase

5.2.3 Subgrade Sensors

Subgrade instrumentation consisted of PCs, CS pairs, and MS. Two PCs (one in each test item) recorded vertical compressive stress at the top of the clay subgrade. Figure 40 shows peak stress versus pass number. The period between Overload 2 and Overload 3 corresponded to the summer season, where higher asphalt temperatures could have been expected to result in higher subgrade stresses under load. However, subgrade stresses gradually decreased between about 27,000 and 41,000 passes. PC responses did not reveal any damaging effect from the applied overload. PC-LFC5N-2 peak responses increased significantly (approximately 25%) during Overload 3 but returned to the pre-overload values when normal traffic resumed. Peak stresses on the non-overload side (LFC5S) began to drop after about 48,000 passes and were lower than LFC5N for the remainder of the test.

Appendix F includes LEAF stress computations performed in support of the PCR analysis. LEAF predicts a maximum vertical stress at the top of the LFC-5 subgrade under the 36,000-lb D gear normal load of 11 psi. For comparison, this is about half of the recorded peak PC response in Figure 40. Reasons for the difference in maximum stress are still being investigated but may include a significantly higher stress concentration in the real subgrade soil (i.e., a narrower stress bulb) than assumed by the linear elastic LEAF model.

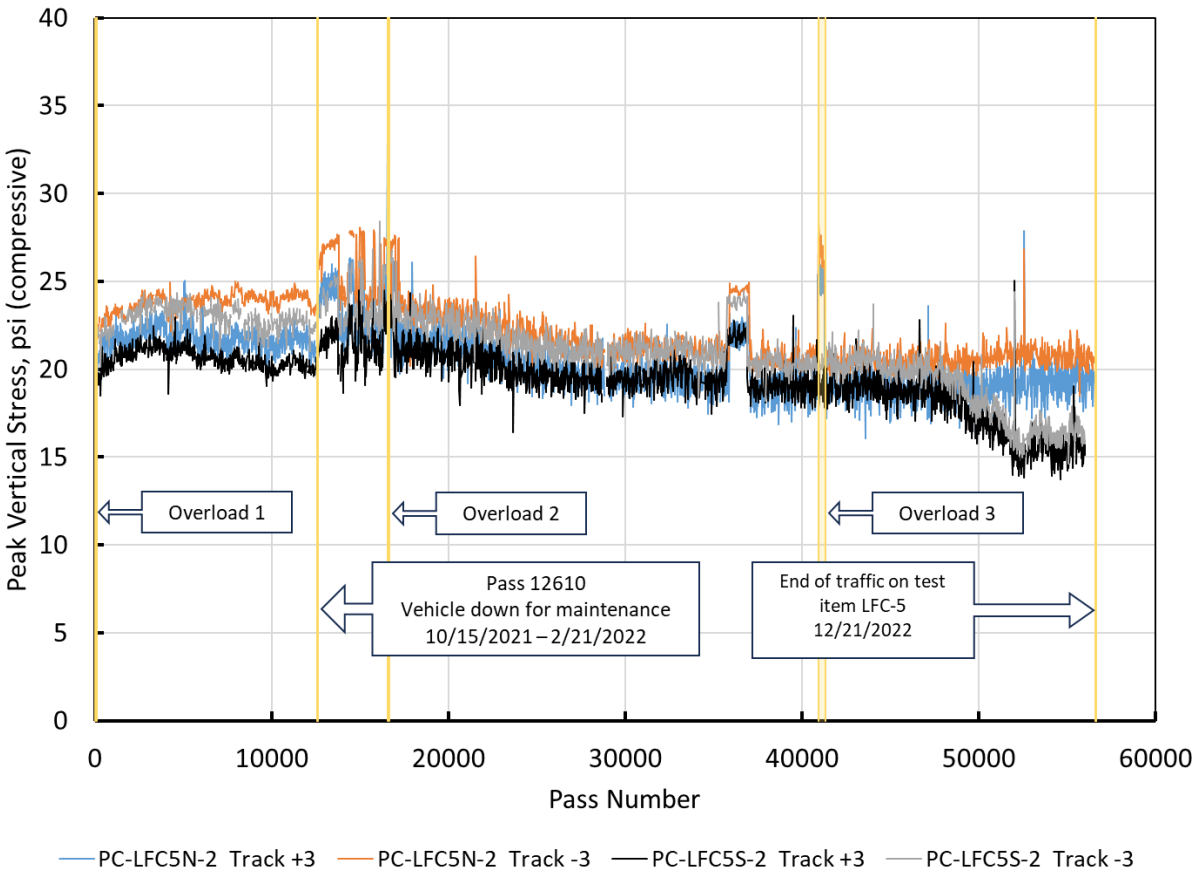

Figure 40. Peak Vertical Compressive Stress at top of Clay Subgrade

Figure 41 plots subgrade permanent deformation against pass number. The permanent deformation as measured by a CS pair is the change in the unloaded (static) coil separation distance from the start of traffic. The first two overload events had no discernable effect on permanent deformation of the subgrade. However, the third overload event produced a noticeable increase in permanent deformation in the north test item as indicated by CS-LFC5N-1/2. (CS-LFC5N-3/4 failed just prior to Overload 3.) Figure 41 also shows a significant increase in permanent deformation in test item LFC5S (non-overload) compared to LFC5N, after about 27,000 passes. Possible reasons for this increase are examined in Section 5.5 . Also, Figure 41 shows that CS-LFC5N-3/4 (orange dashed line) began to show signs of malfunctioning at about 31,000 passes. Nevertheless, the responses are shown for the analytical value they provide.

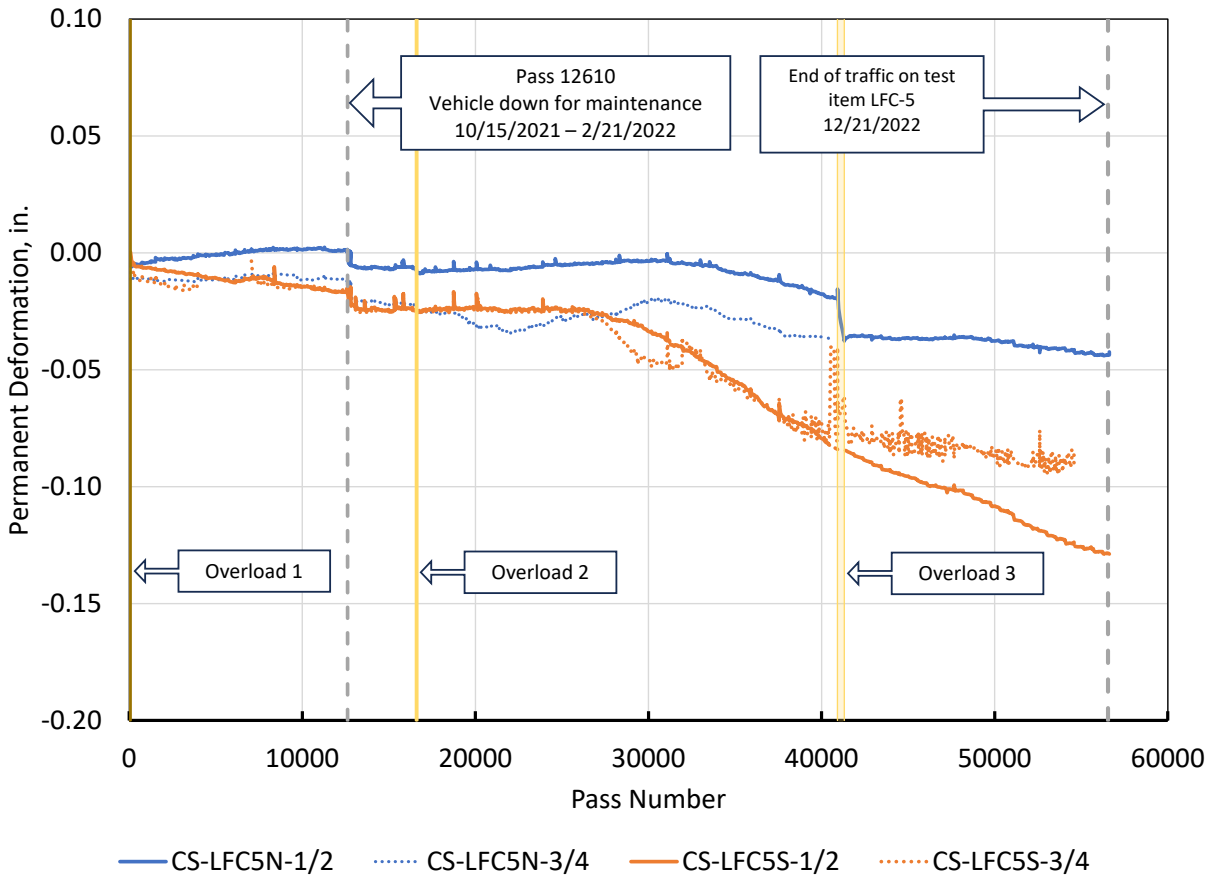

Figure 41. Permanent Deformation of Subgrade from CS Data

Figure 42 plots peak vertical subgrade compressive strains with respect to pass number for the life of the test. Strains were obtained from CS pairs at the top of the subgrade, by dividing the maximum vertical displacement under load (Track 0) by the unloaded (static) coil separation distance at the end of the previous wander sequence. Both CS pairs on the north test item (CS-LFC5N-1/2, CS-LFC5N-3/4) exhibited steep strain increases under overload that returned to their usual values upon resumption of normal loads. CS-LFC5N-3/4 failed before the third overload event, at about 37,000 passes. All CS responses show that repeated passes led to a large increase in the magnitude of subgrade strain, independent of overload, which eventually reached a stable value. At Pass 12,610, there was an unplanned pause in traffic due to vehicle maintenance, which lasted for approximately 4 months (see Table 13). After this vehicle down time, the strain recovered to pre-traffic levels in both test items but increased again (and leveled off again) with further traffic. Possible reasons for the gradual increase in subgrade strain responses are analyzed in greater detail in Section 5.5 .

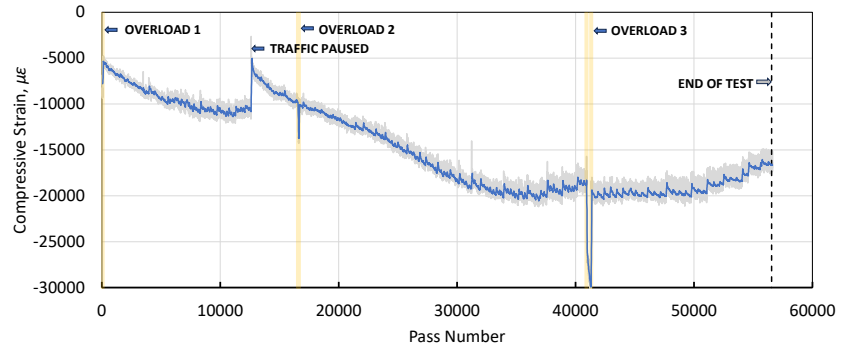

(a) CS-LFC5N-1/2 (North)

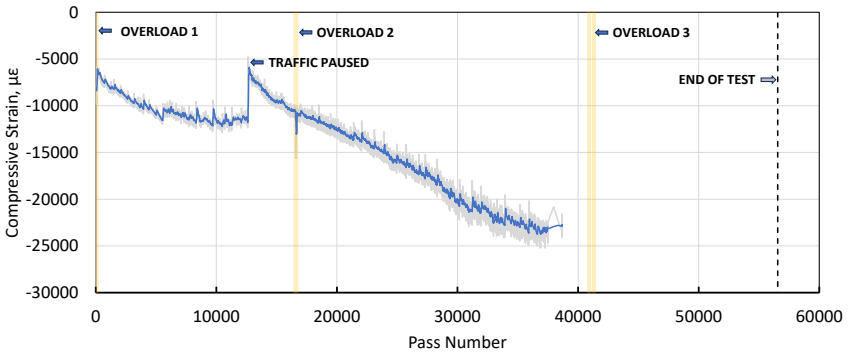

(b) CS-LFC5N-3/4 (North)

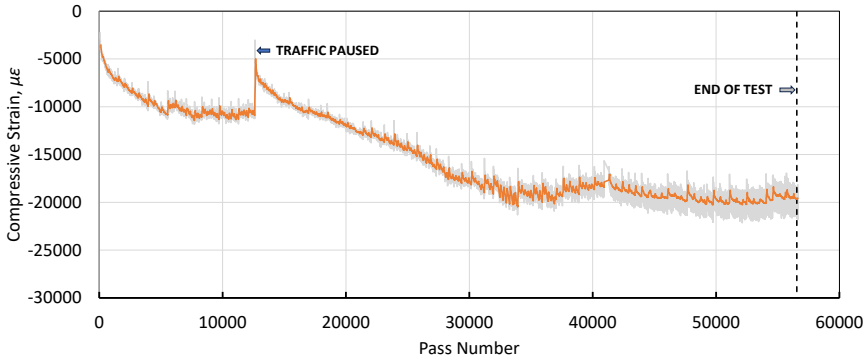

(c) CS-LFC5S-1/2 (South)

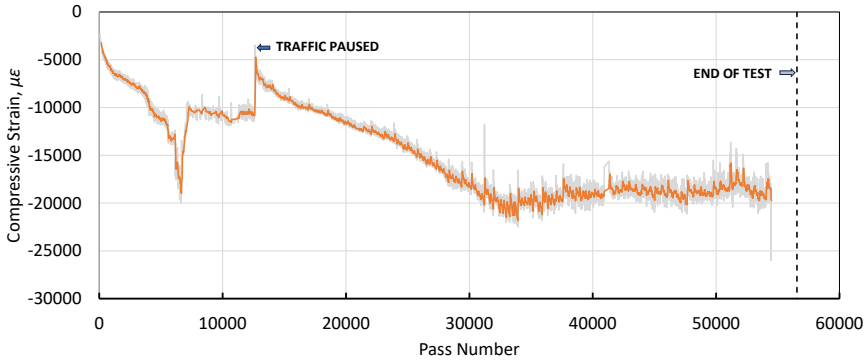

(d) CS-LFC5S-3/4 (South)

Figure 42. Peak Compressive Strain at Top of Clay Subgrade from CS Pairs

Figure 43 plots gravimetric MC *w* in the clay subgrade as a function of pass number. Gravimetric moisture content was determined from volumetric moisture content using the formula in Section 4.3.5.2 and the hourly readings of subgrade MS. In situ MC was highest in the summer months and lowest in the winter, with the lowest value of *w* recorded just before the resumption of traffic following maintenance down time. Higher moisture contents are associated with lower soil strength due to inability of the clay soil to rapidly dissipate excess pore water pressure induced by loads. While it is notable that LFC-5S experienced a higher rate of permanent deformation than did LFC-5N, although only the latter received overloads, this may be due to the higher MC in the LFC-5S subgrade.

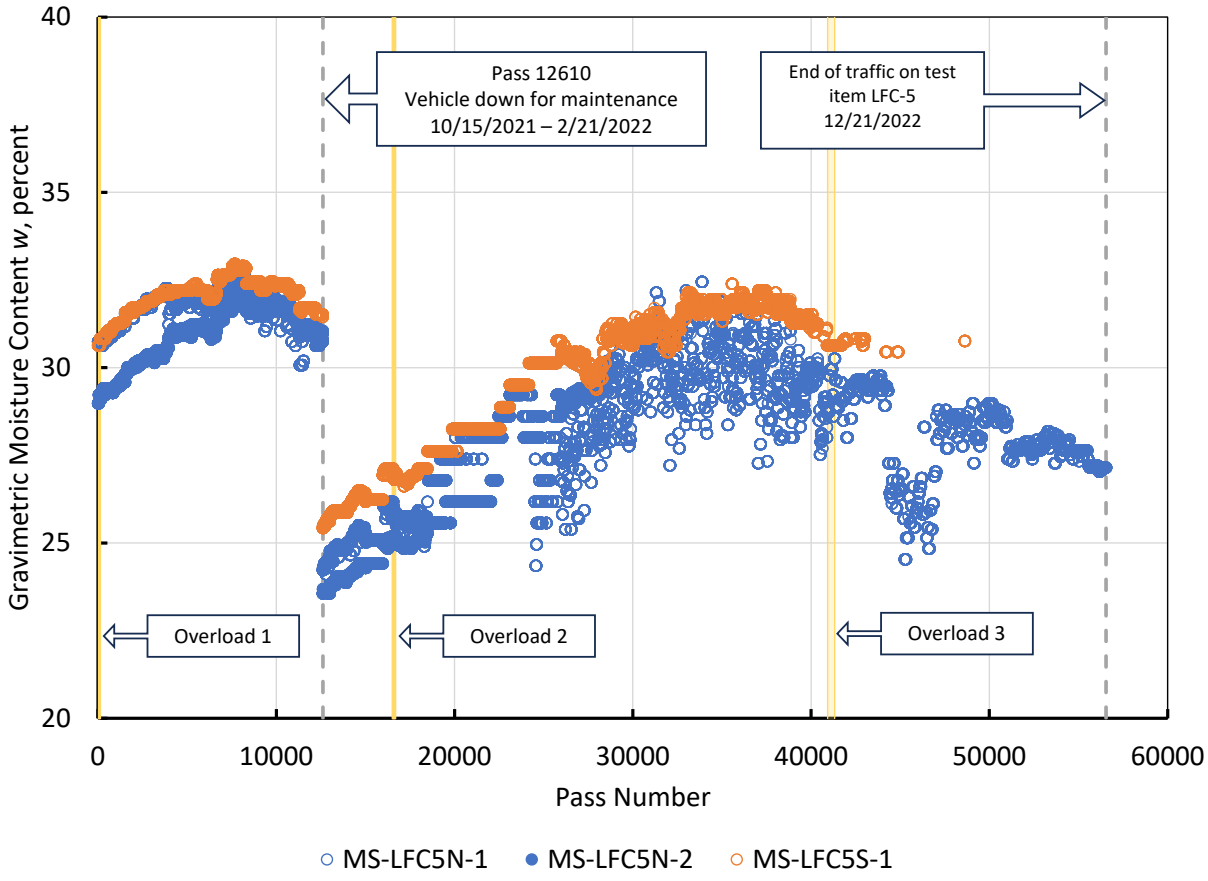

Figure 43. Gravimetric Moisture Content in Clay Subgrade

5.3 NONDESTRUCTIVE TESTING ANALYSIS

Section 4.3.5.5 discusses the ratio of AUPP indices between trafficked and non-trafficked areas as an indicator of structural damage due to traffic. Figure 44 plots this ratio as a function of pass number. In these plots, AUPP for the trafficked lane is measured at offsets -15 and +15 ft (center of traffic), while AUPP for non-trafficked areas is measured at offsets -25, -5, +5, and +25 ft. The ratios generally followed the same trend, reaching a peak value in mid-spring in 2022, and decreasing with higher temperatures during the summer. However, after approximately 35,000 passes, fatigue cracking in both test items was severe enough that the AUPP ratios began to

increase again and continued to increase until the end of the test. AUPP ratios in LFC-5N were somewhat higher than those in LFC-5S, which could be attributed to overload-induced damage in LFC-5N.

In situ layer moduli were determined by backcalculation from HWD test data. Figure 45 plots the backcalculated modulus values for all structural layers against vehicle pass number. In each plot, the solid markers represent trafficked areas and the hollow markers untrafficked areas of LFC-5N and LFC-5S. For both the P-401MR and P-209MR layers, the trafficked area moduli were lower than the corresponding untrafficked moduli, indicating traffic-induced structural deterioration. LFC-5N exhibited a significant decrease in asphalt layer stiffness following the first overload wander, but not after the second, and an increase after the third. Extensive cracking of the AC resulted in lower modulus values at the end of the test for both test items. For most of the test, and for both test items, the backcalculated subbase layer (P-154MR) moduli were noticeably lower for the trafficked than for the untrafficked sections. Compared to the upper structural layers, the P-152MR subgrade modulus exhibited less variation. In both test items, modulus values varied over a wider range in the trafficked areas than in the untrafficked areas.

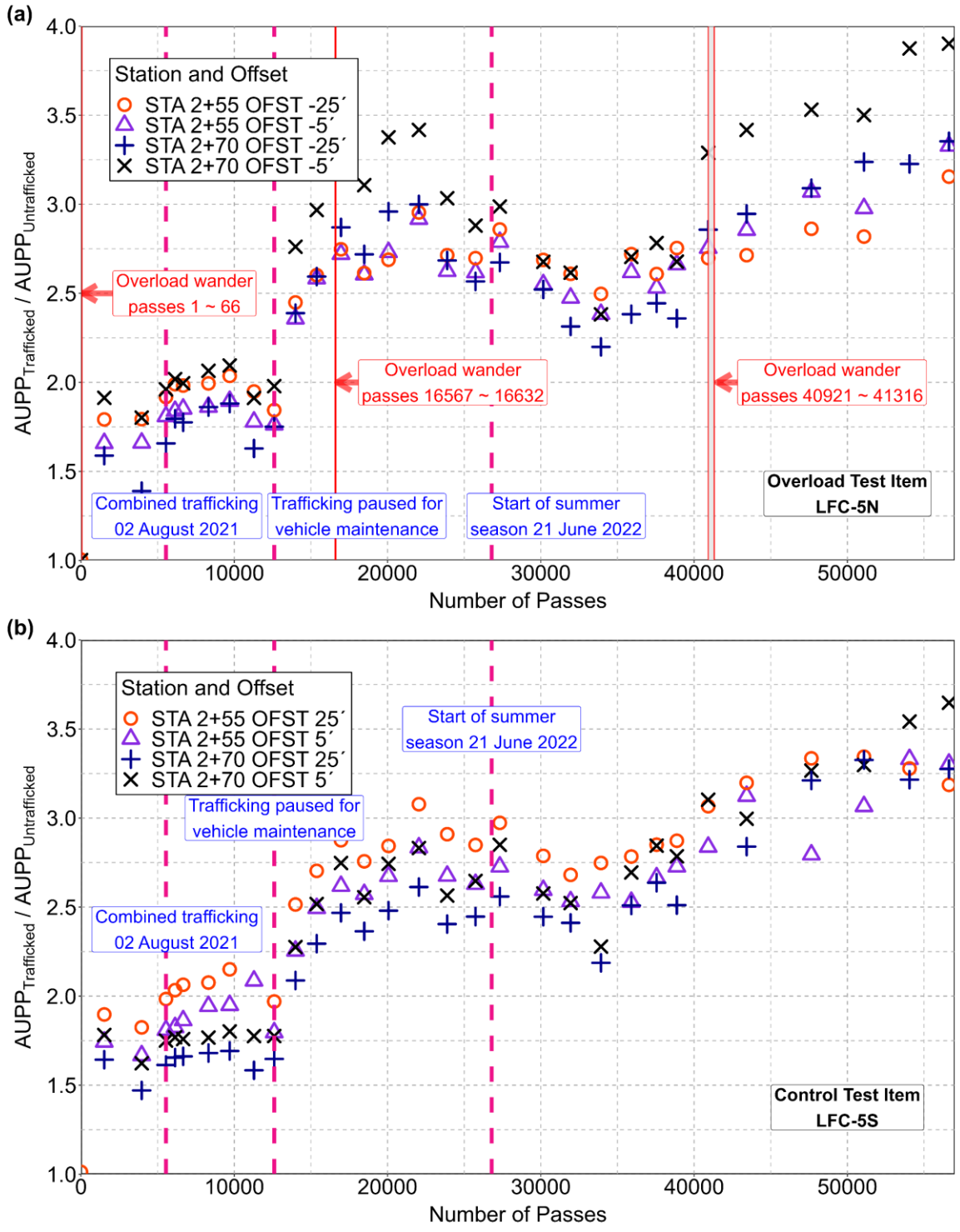

Figure 44. Change in AUPP Ratios (trafficked to non-trafficked areas)

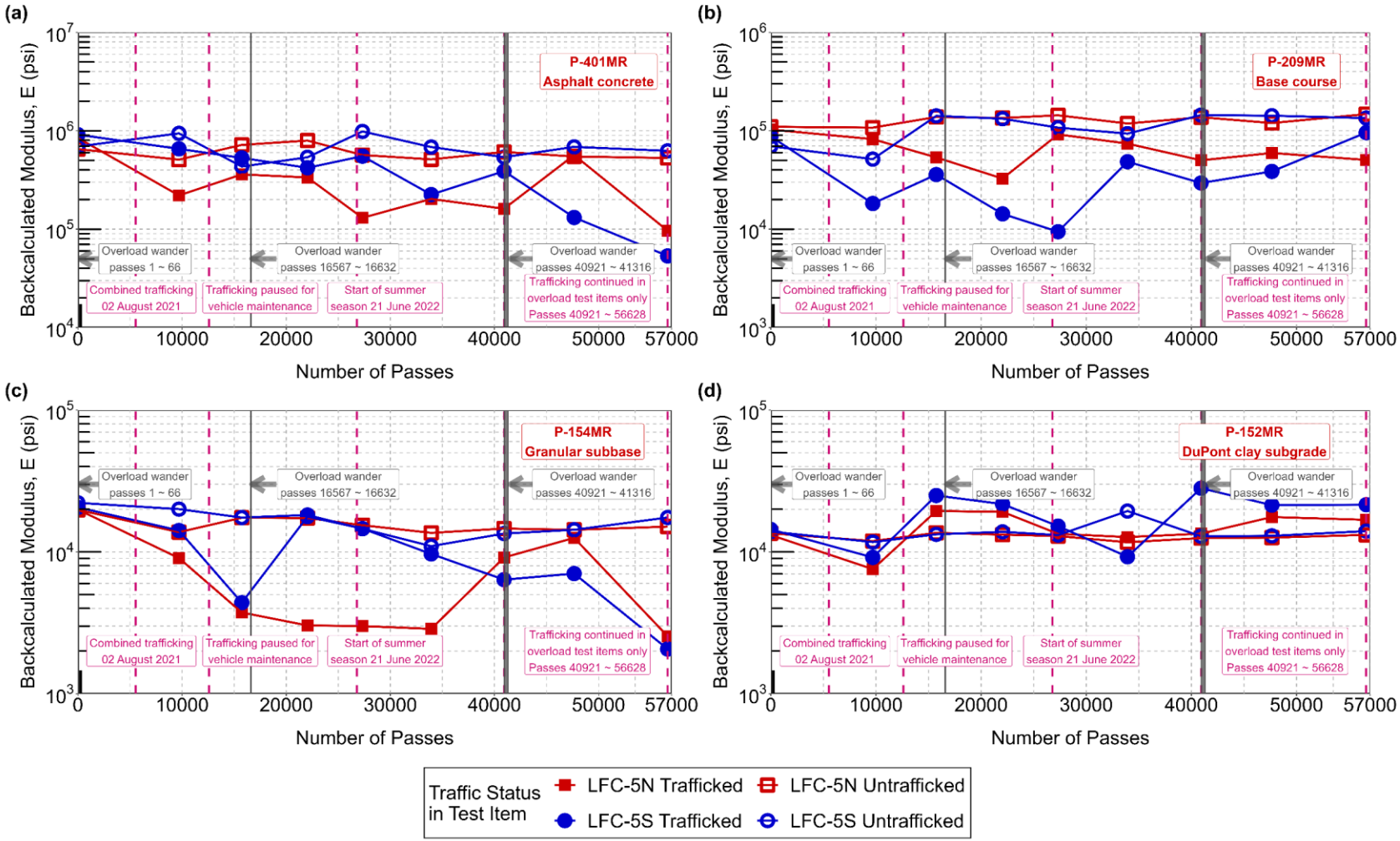

Figure 45. Backcalculated Modulus Values of (a) P-401MR Asphalt Concrete, (b) P-209MR Base Course, (c) P-154 Granular Subbase, and (d) P-152MR Clay Subgrade

Several ground-penetrating radar (GPR) datasets were analyzed for the overload test area, as listed in Table 14. Data were collected prior to, during, and after trafficking. The date of the "during trafficking" dataset corresponds to the start of a large increase in rutting seen over the summer of 2022.

Table 14. Ground-Penetrating Radar Datasets Analyzed for the CC9 Overload Test

Dataset Name and Date	Passes	Notes
2021-June-24 Pre-traffic baseline (Test Item 5)	0	Baseline, summer
2022-June-13 Trafficking	26,004	Prior to large increase in surface rutting, summer
2022-Dec-05 Post-traffic	54,582	Close to end of traffic, winter

Figure 46(a) and (b) show pre-traffic longitudinal profiles of layer interfaces as determined by GPR. The heavy vertical lines (dash-dot lines) mark the station (STA 2+55) for the transverse profiles in Figure 47.

Figure 47 combines data from surface elevation surveys (based on laser scanning) and GPR to show the deformed transverse profile of three surfaces: (a) asphalt surface (grade), (b) asphalt-base interface, and (c) base-subbase interface. Transverse profiles clearly show the progression of layer deformation with traffic. Rutting occurred in all structural layers (asphalt, base, subbase). The upper layers (P-401MR and P-209MR) deformed without significant loss of thickness. The deformed profiles indicate possible cracking of the asphalt layer and/or intrusion of base material into the surface layer at offsets -8 and +22 ft. There was some upheaval in all layers adjacent to trafficked areas, the magnitude of which varied from layer to layer. The 2.6 GHz GPR did not penetrate to the top of the subgrade, so it is impossible to determine from these data the extent of subgrade surface deformation.

Layer thicknesses for the asphalt (Table 15) and base (Table 16) courses were estimated from GPR. Asphalt thickness was generally uniform in both test items with little difference between trafficked and untrafficked areas outside of normal tolerance. Table 16 shows what may be evidence of a small amount of densification of the base layer under traffic (0.3–0.4 in.) on the LFC-5N side. However, this difference is well within the measurement uncertainty for GPR, so it cannot be clearly linked to normal traffic or overloading.

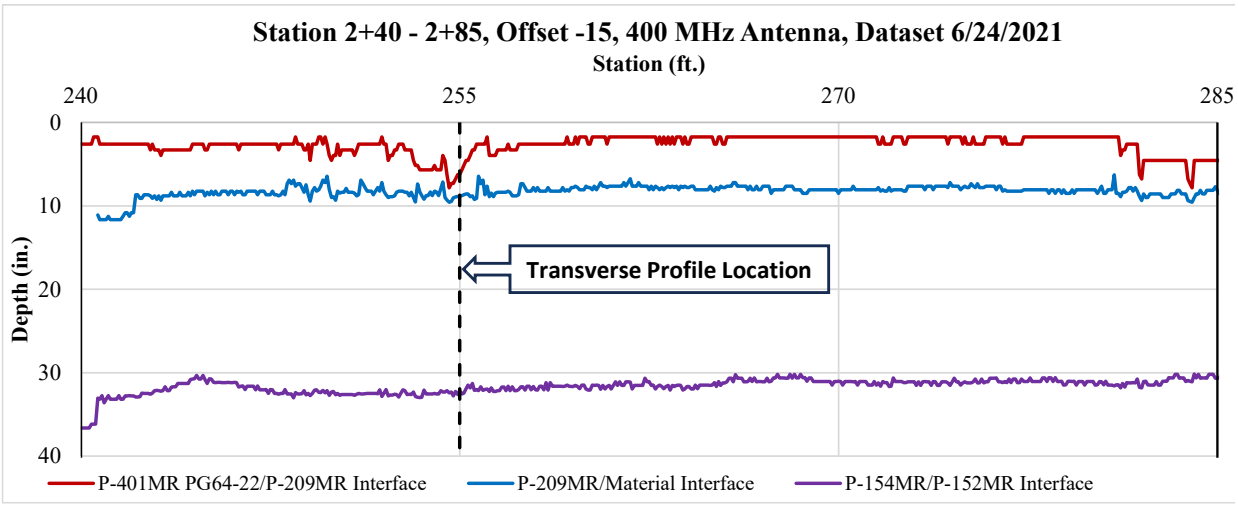

(a) Offset 15 ft left (LFC-5N centerline)

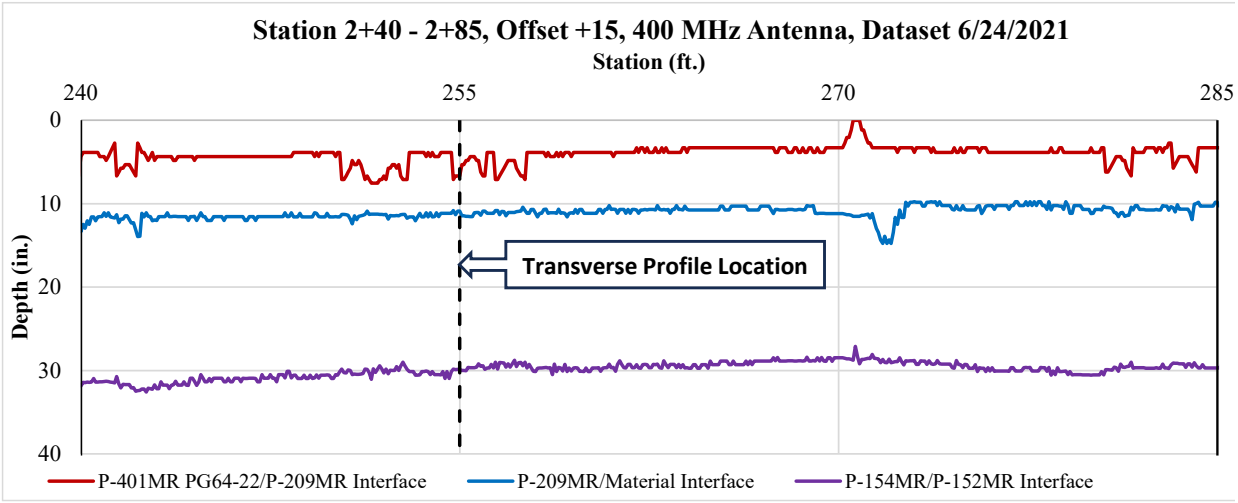

(b) Offset 15 ft right (LFC-5S centerline)

Figure 46. Longitudinal Profiles (baseline, pre-traffic)

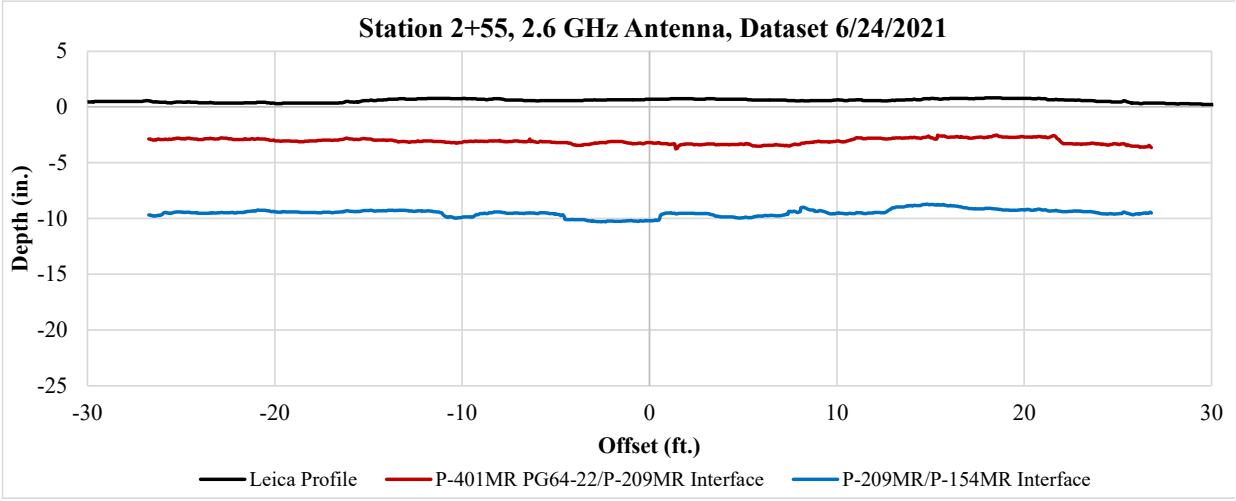

(a) Profile at start of traffic test

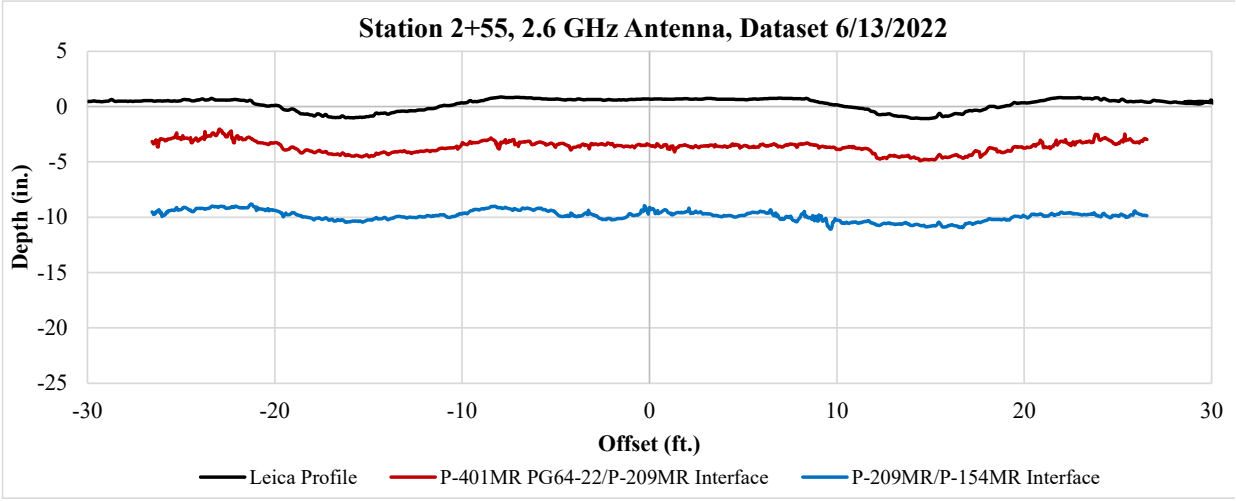

(b) Profile after 26,004 passes

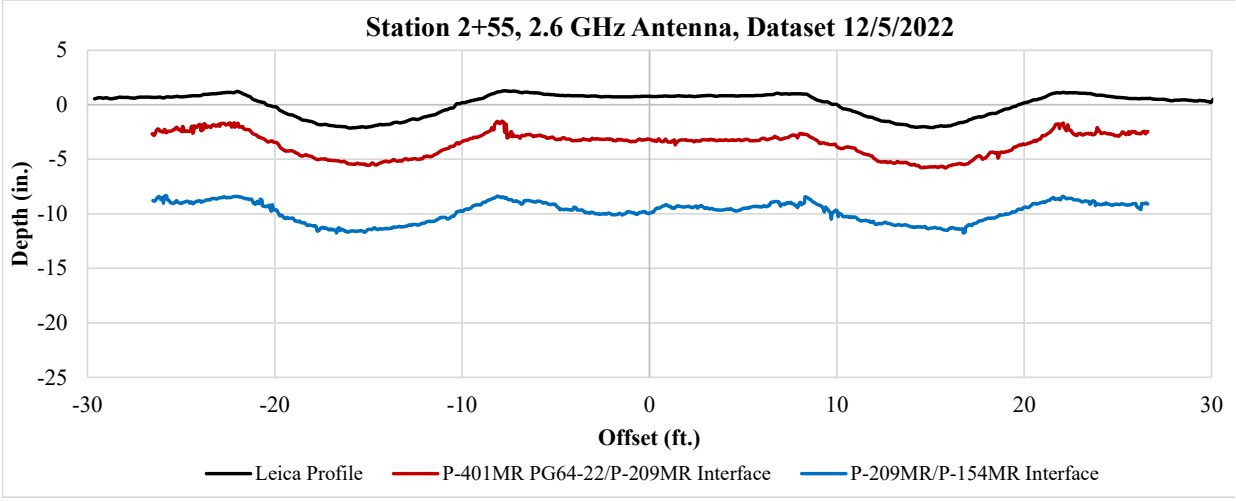

(c) Profile close to end of traffic test (54582 passes)

Figure 47. Transverse Profiles, STA 2+55

Table 15. Estimated Thickness (GPR) of Asphalt Layer

Pass No.	LFC-5N thickness (in.)		LFC-5S thickness (in.)	
	Traffic	Non-traffic	Traffic	Non-traffic
As-Built	3.3	3.3	3.3	3.3
0	3.3	3.2	3.6	4.0
27,324	3.3	3.2	3.6	3.6
56,628	3.5	3.2	3.5	3.5

Table 16. Estimated Thickness (GPR) of Base Layer

Pass No.	LFC-5N thickness (in.)		LFC-5S thickness (in.)	
	Traffic	Non-traffic	Traffic	Non-traffic
As-Built	6.0	6.0	6.1	6.1
0	6.3	6.7	6.2	5.3
27,324	5.9	6.7	6.2	6.5
56,628	6.0	7.1	6.1	6.3

Rutting of up to 2.5 in. was observed in the trafficked areas of both test items. Because no significant thickness change was detected in either the asphalt or base layers, it can be concluded that the rutting was concentrated in the subbase and/or clay subgrade layers. As indicated above, the GPR equipment cannot accurately determine the deformed shape of the subgrade surface, so the exact amount of subbase deformation must be determined by destructive investigation.

One notable anomaly in the data was the apparent increase in LFC-5N asphalt thickness at the end of traffic. Variability in the data accounts for some anamolies, but because thickness estimates are affected by each step of GPR data acquisition and processing, it was not possible to assign definite variability and standard deviation values. The following is a list of possible sources of variability:

- Not all GPR data were available for each layer and for each dataset, due to equipment limitations or equipment issues preventing data collection.
- GPR data processing requires assumptions for each dataset and for specific layers (e.g., assigning dielectric values), which adds to the variability.
- The thickness values shown for each dataset (pass number) are the result of averaging the data from multiple antennas and locations (average trafficked versus average untrafficked) and the performance of an outlier analysis.
- When analyzing data from trafficked locations, analysts generally considered thickness variations in the range 0.3–0.4 in. to be normal and reasonable, as that was the observed variability in the untrafficked data.

Additional information and analysis regarding NDT data collected in CC9, including the overload test, is found in Mazzotta et al. (2024).

5.4 FAILURE CONDITION ANALYSIS

Neither LFC-5N nor LFC-5S reached failure criterion (i) in Section 4.3.3 , defined as surface upheaval of 1 in. or more. At the end of the test (>56,000 passes), the maximum surface upheaval and rutting in LFC-5N were 0.75 in. and 3.0 in., respectively. Both test items exhibited extensive cracking damage, and so were considered failed by criterion (ii). As expected, the actual number of passes to failure, including overload passes, was far higher than the FAARFIELD design prediction (about 6,500 passes based on the subgrade failure criterion). Distress surveys found that alligator cracking was the primary mode of distress in both test items.

The flexible ACR/PCR procedure outlined in ICAO (2020, 2022) depends only on the subgrade failure criterion and has no ability to consider HMA fatigue. FAARFIELD PCR computations (Section 4.1) projected that the CC9 overload test item could tolerate 6,500 passes of the NAPTF D gear at the normal wheel load of 36,000 lb. Including 2% overload traffic at ACR 75% above PCR (i.e., 132 passes of the 57,000-lb D gear) reduces the predicted structural life by about half to 3,250 passes. In the actual test, overload test item LFC-5N exhibited significant alligator cracking at 18,480 passes, after experiencing two overload events totaling 132 passes, while the control test item also experienced significant alligator cracking under normal traffic only. Following the design theory, both test items should have failed in subgrade rutting, as computed HMA CDF was less than 1% of subgrade CDF. However, in the current test as well as in the previous CC7 overload tests, the asphalt fatigue mode was significant. In CC7, where test item cross sections and traffic loading mirrored the current test, four out of the six CC7 test items failed in fatigue (extensive alligator cracking). In the remaining two CC7 test items, subgrade shear failure occurred simultaneously with HMA fatigue failure. CC9 test items showed the same trend of surface cracking failure preceding failure in subgrade shear.

A main goal of this research was to evaluate the hypothesis, based on the results of CC7, that there exists a threshold level of subgrade strain that when exceeded (i.e., during an overload event) leads to damage causing accelerated failure. Compressive strains from CS pairs placed at the top of the subgrade were monitored for any indication of disproportionate damage during the test, especially during the ramp-up response test (Section 4.2.2) and the three overload applications. Figure 48 shows the compressive strains at the top of the subgrade during the ramp-up response test from CS-LFC5N-3/4. Of the two CS pairs on the north test item, CS-LFC5N-3/4 provided the better data quality during the ramp-up test. The FAARFIELD-computed strains corresponding to the 36,000-lb D gear normal load and to the 57,000-lb D gear overload are also indicated. While the FAARFIELD strain response curve (based on LEAF) is linear with respect to increasing load, the in situ strain response curve from the ramp-up tests was noticeably nonlinear. The discrepancy becomes very significant beyond about 26,000 lb-wheel load. Thus, at the target overload, the peak vertical strain experienced in the subgrade soil under the wheel was about 50% greater than the strain predicted by FAARFIELD analysis (2,400 με) for the same load. Furthermore, as shown in Section 5.2.3 , the peak strain magnitude at the subgrade level continues to grow with additional traffic passes. Thus, estimating a true compressive strain from a given overload level is difficult to determine, because it requires knowledge of both nonlinear soil behavior and loading history.

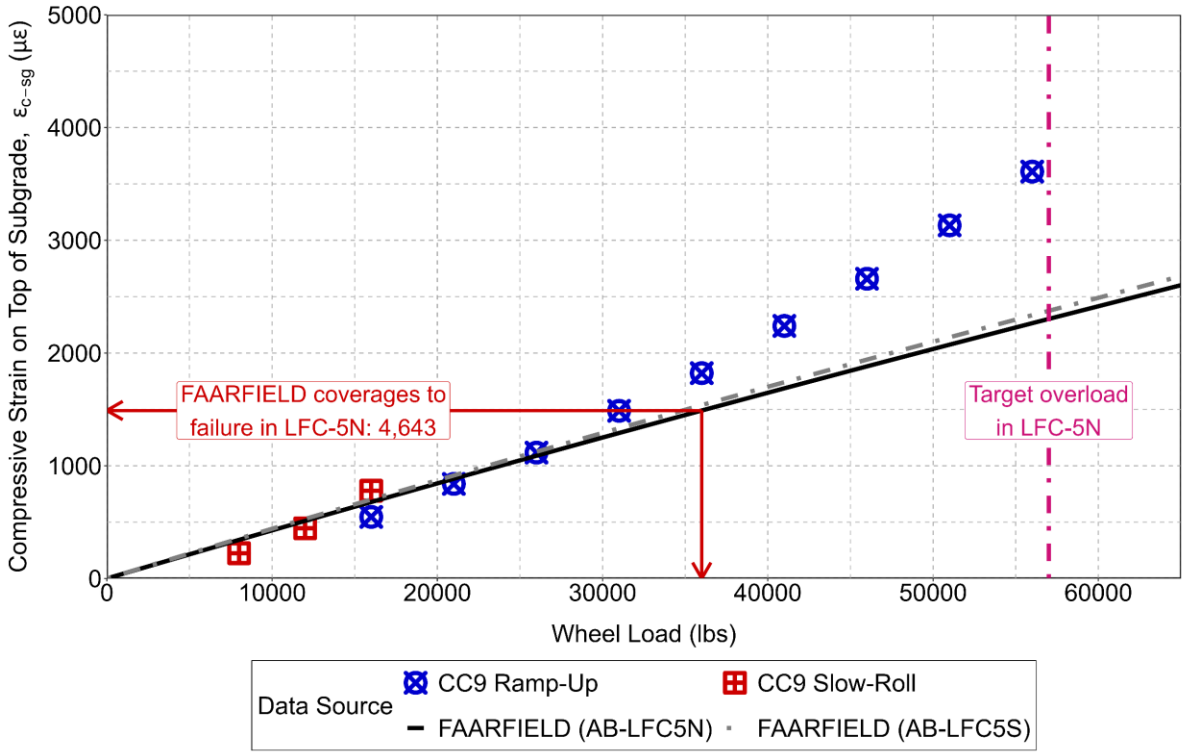

Figure 48. Compressive Strains Recorded at the Top of Subgrade During the Ramp-Up Response Test in Overload Test Item LFC-5N

Because both test items manifested significant fatigue distress, researchers also examined tensile strains at the bottom of the asphalt layer. Because of ASG failures early in the test, the usable ASG data only cover the first overload event (66 passes) and the first normal wander pattern (66 passes) immediately following it. Figure 49(a)**Error! Reference source not found.** and (b)**Error! Reference source not found.** show the mean peak strains in the longitudinal and transverse directions, respectively, for overload and for normal load (Tracks +3 and -3, W→E). As expected, the peak strain decreased when normal loading resumed after the overload. The following are key observations from Figure 49(a) **Error! Reference source not found.**and (b)**Error! Reference source not found.**:

- LSG-LFC5N-2 had the highest decrease (15.6%) in average longitudinal tensile strain following resumption of normal load.
- TSG-LFC5N-3 had the highest decrease (22.8%) in average transverse tensile strain.
- The coefficient of variation for strains at the same wheel load (indicated by error bars) was generally higher than the mean strain difference due to load.
- No critical threshold for asphalt tensile strain could be determined from these data because all ASGs failed before the second overload event; that is, before the onset of fatigue failure was observed.

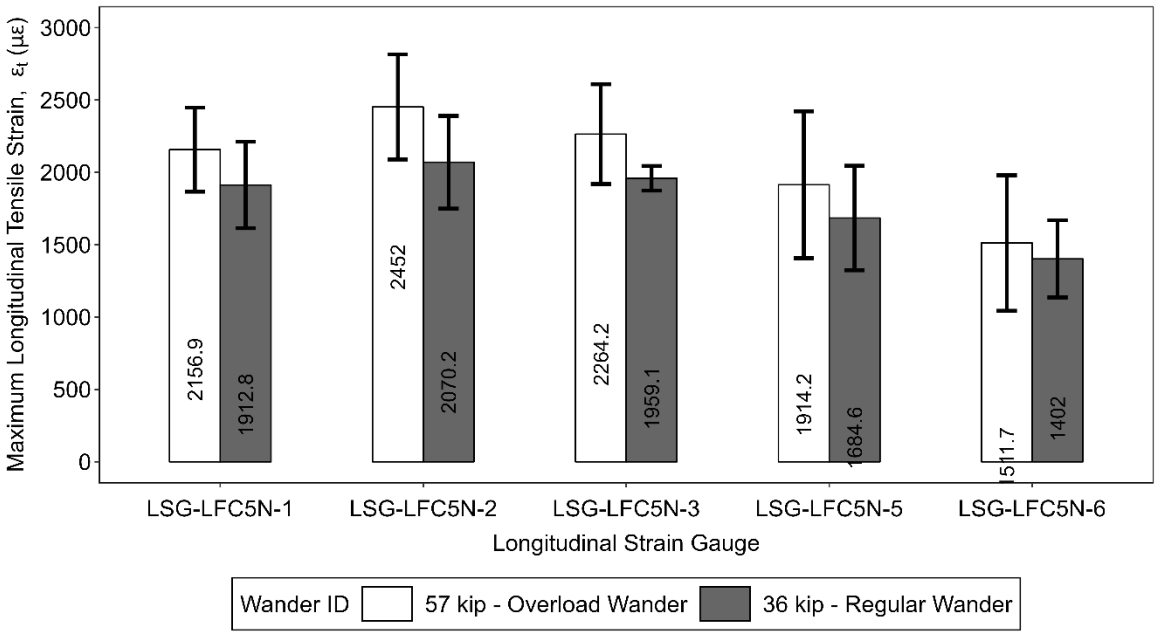

(a) LSG readings

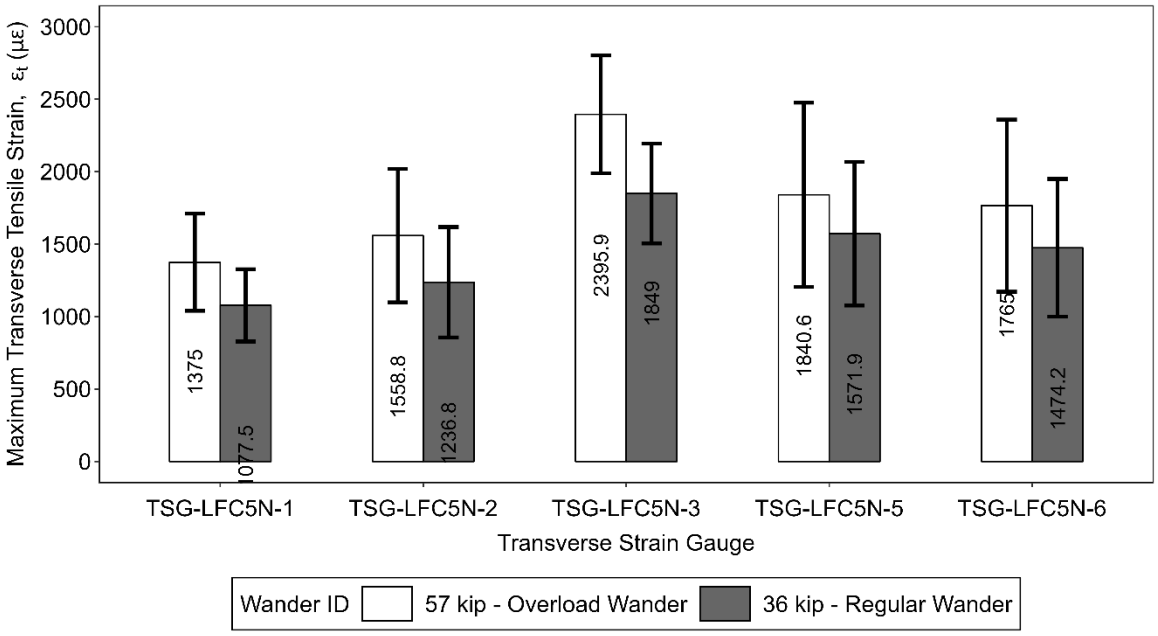

(b) TSG readings

Figure 49. Variability in Peak Asphalt Strain Readings Following First Overload Event

5.5 SUBGRADE RESPONSE ANALYSIS

Section 5.2 presented subgrade sensor responses from PC and CS pairs. It was observed that sensor readings over time deviated significantly from the design assumptions. Researchers analyzed the mechanical behavior of the clay subgrade to explain the observed sensor responses. The main goals of this analysis were to

- evaluate the load- and environmental-related contributions to subgrade responses during trafficking;
- compare the vertical deflections at the top of the subgrade under varying environmental conditions; and
- identify any subgrade behavior or relationships that bear on airport pavement overload criteria.

Preparing the data for this analysis required two additional steps. The first step was to merge the traffic- and environmental-related data. This was necessary because these data were collected at different times (i.e., triggered by a traffic event versus regular hourly collection). The second step was to develop a method to minimize the effects of bias, drift, and permanent deformation from each signal, resulting in a clean signal reflecting only the subgrade response to the vehicle. These steps are described in detail below.

Combining Traffic-Related and Static Data Sources:
Sensors used for this analysis operated in either static (MS) or dynamic (CS and PC) mode. The MS recorded data periodically, typically at the start of every hour, independent of traffic events. Dynamic sensors collect data during each vehicle pass and are triggered by vehicle movement. Each dynamic sensor data file includes a timestamp indicating the start time, which generally does not coincide with static data collection. Merging these two datasets was the first step in the detailed analysis of subgrade data. During processing, each dynamic data file was aligned with the nearest static data file (nearest hour). For example, if dynamic data were recorded at 10:52:33, then the static data from 11:00:00 was used as the representative static measurement.

Separating Subgrade Load-Related Response from Permanent Deformations:
This phase of the analysis focused on the load-related responses in the subgrade. Isolating the load-related part poses a challenge because the sensor responses can include built-in readings after construction, biased readings due to permanent deformation, sensor creep or drift, and many other considerations. Furthermore, CS pairs measure only the distance between the coils, not subgrade deflection or strain directly. To remove the accumulated deflection or creep response, all data points in a dynamic response history were normalized by the average of the first 20 data points recorded. The normalization process translates the CS spacing into a measurement of vertical deflection at the subgrade as illustrated in Figure 50. (Figure 50 also depicts the lower coil as stationary, but this is unnecessary.)

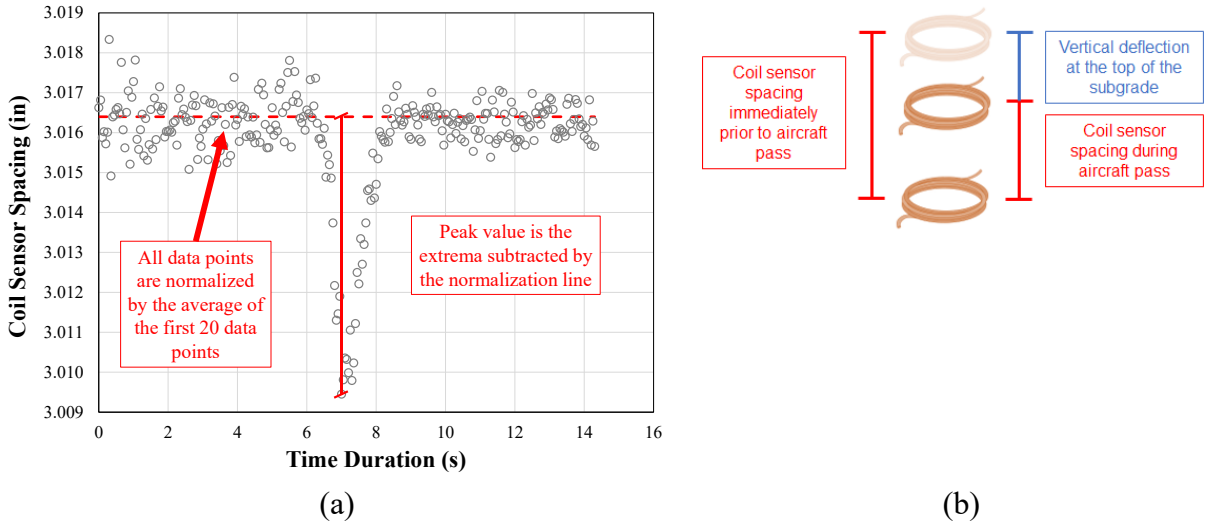

Figure 50. Signal Normalization Process Using (a) CS Data and (b) an Illustration of its Physical Interpretation

Figure 51(a) and (b) refer to LFC-5S and show the load-induced (a) peak vertical deflections and (b) peak vertical stress readings at the top of the subgrade, for the critical tracks. The critical tracks for PC and CS are Tracks ±3 and 0, respectively. For clarity, Figure 51 plots the peak sensor data with a 10-point moving average. Both sets of CS pairs show that the top-of-subgrade deflection increased over the duration of the test, with an initial average deflection of 0.0072 in. (0.183 mm) at the first pass along the critical track, and a maximum average deflection of approximately 0.057 in. (1.45 mm). As discussed above, Figure 51(a) excludes the effect of permanent deformation in the subgrade, thus the overall increasing trend is not explained by permanent deformation of the subgrade. Furthermore, the vertical deflections returned to near the initial state after the conclusion of the 5-month break in trafficking, then progressively increased after traffic resumed. Compared to the CS, the peak vertical PC response remained relatively constant throughout the test, although with an overall slight downward trend.

Figure 52 plots (a) the MS readings in the subgrade and (b) temperature measured in the asphalt layer against pass number (temperature data are from LFC-5N). Like Section 5.4 , volumetric MC was measured by the MS and converted to gravimetric moisture content (w) using the formula in section 4.3.5.2. Figure 52(a) shows that gravimetric moisture content initially increased, then dropped in a discontinuous manner, followed by a general increasing trend. The discontinuous drop observed in Figure 52(a) corresponds to the approximately 5-month pause in traffic. Though it might seem intuitive to expect moisture changes over a 5-month period, in this case the moisture is in a slow-draining material (i.e., CH), and the NAPTF is an enclosed facility that is not exposed to any additional sources of moisture. Under such conditions, the properties of the clay control the moisture migration in the subgrade. Jumikis (1977) has noted "In such soils [silts and clays], there exist all conditions for soil moisture migration along the thermal gradient, resulting in considerable soil moisture redistribution," giving a reason for the observed change in moisture. Although thermocouples were not installed in the subgrade, the temperature

in the asphalt mixture fluctuated seasonally as would be expected in an environment that is not temperature controlled (Figure 52(b)).

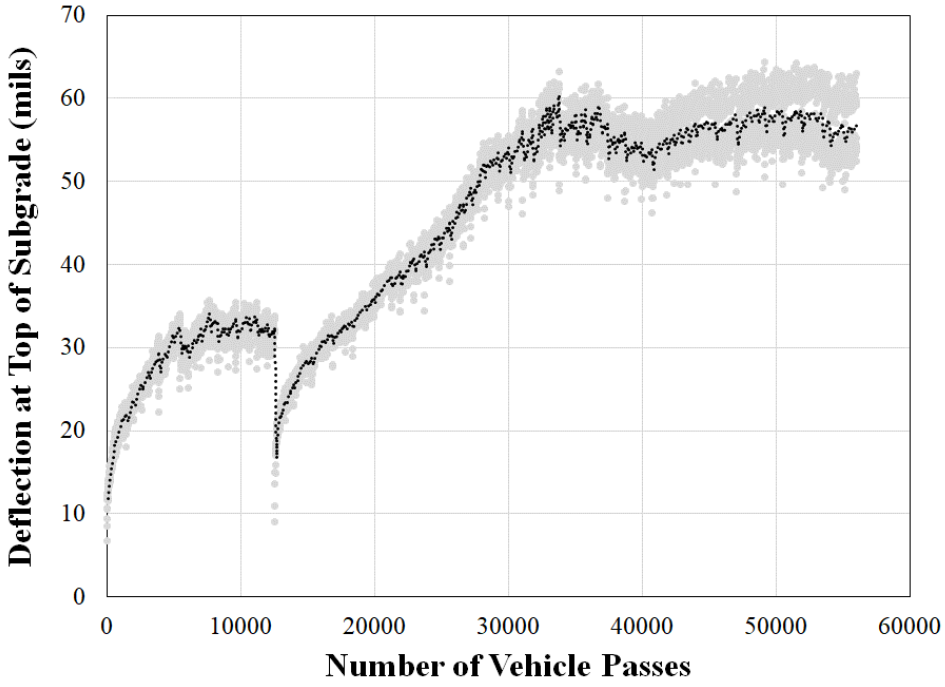

(a)

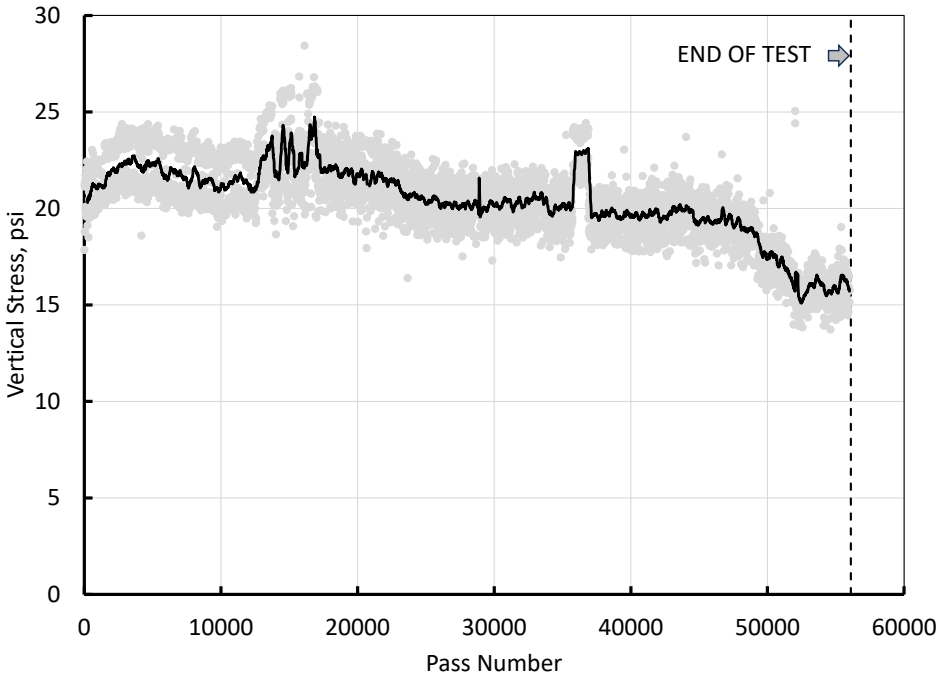

(b)

Figure 51. Critical Responses During CC9 Trafficking for (a) CS and (b) PC

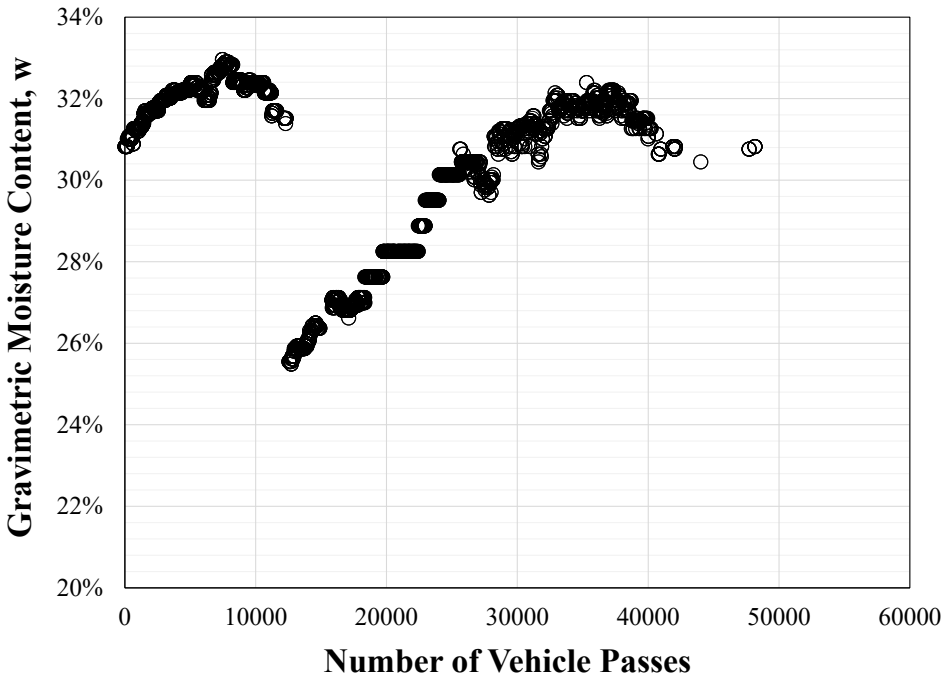

(a)

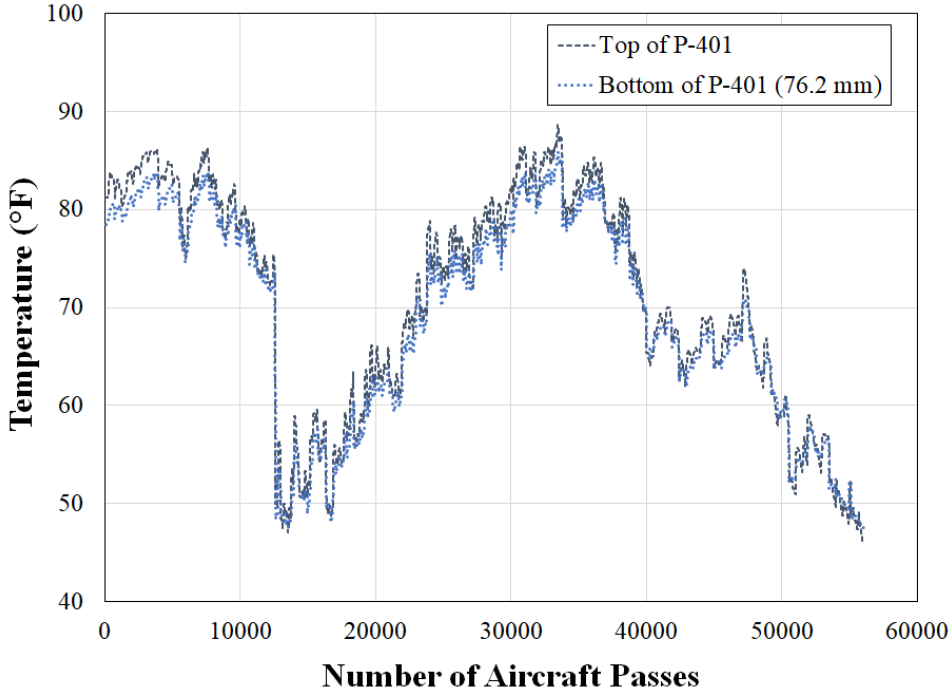

(b)

Figure 52. Environmental Responses During CC9 Trafficking for (a) MS and (b) LFC-5N Thermocouples

To further understand the moisture behavior in the subgrade, the moisture data were ordered by timestamp rather than by vehicle pass. This change allowed for the assessment of subgrade moisture during both the trafficking and non-trafficking periods. Figure 53 plots moisture data

against time, with annotations denoting key data points and periods during trafficking. Figure 53 shows *w* was cyclic throughout the course of trafficking. The cyclic nature of the MC indicates that the clay was not fully saturated throughout the test period, but the cause of the variation remains unclear. Further, the recorded *w* at the resumption of trafficking (February 22, 2022) was substantially different from the *w* at the start of trafficking. The MS began malfunctioning toward the end of the traffic period; nevertheless, the overall trend is consistent and believed to be accurate.

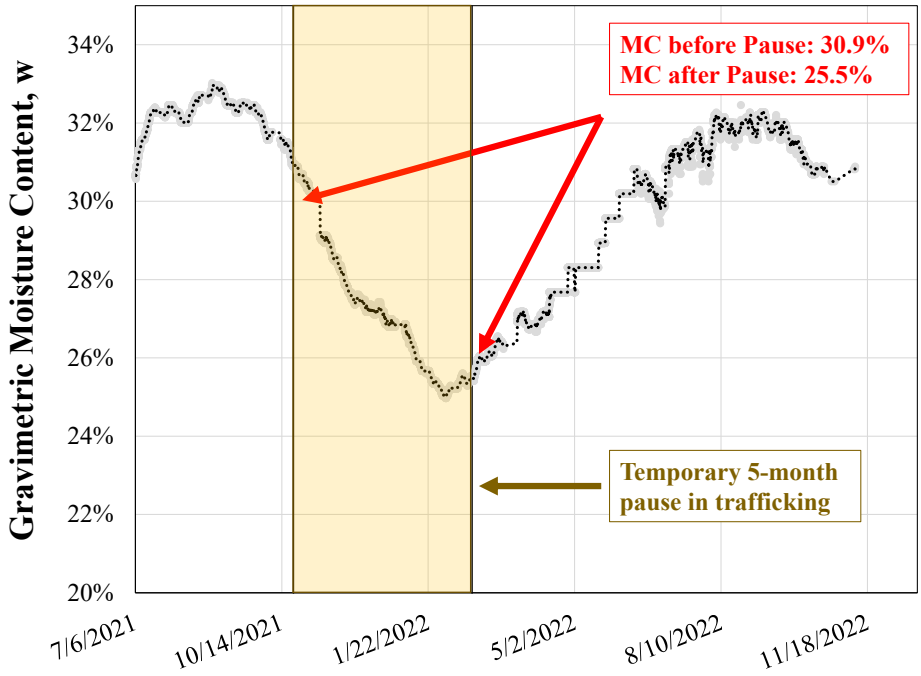

Figure 53. Gravimetric Moisture Content *w* Versus Time (including the traffic pause)

Without a specific cause (e.g., increase in aircraft load or moisture intrusion), the subgrade modulus is not expected to change significantly. Therefore, the large increase in load-induced deflections was unexpected, as was the observed recovery with paused traffic. The large cyclic moisture changes in the subgrade were also unexpected. As clay behavior is known to be highly susceptible to changes in moisture content, researchers assumed a relation between the vertical deflection behavior in the subgrade and the *w*. Figure 54 plots the average top-of-subgrade vertical deflection versus *w*. Although there is no unique correlation between these variables, Figure 54 reveals two distinct data clusters. The two data clusters correspond to the periods before and after the pause in trafficking. Furthermore, both data clusters follow similar trends, suggesting that there is a predictable subgrade behavior in this dataset.

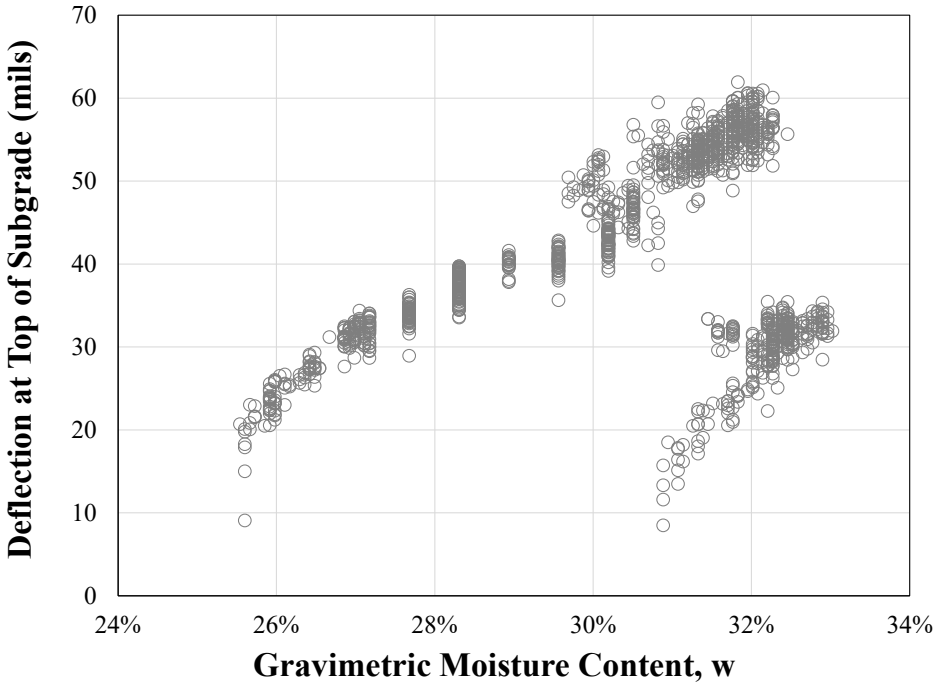

Figure 54. Top-of-Subgrade Average Deflection Versus *w*

To further evaluate the clay behavior, researchers split the dataset into two parts, corresponding to the periods before and after the 5-month pause. For each part, researchers computed the change in gravimetric MC (Δw) using as a baseline the initial *w* reading for each traffic period. Figure 54 plots the vertical top-of-subgrade deflection against Δw for both datasets. Figure 55 shows that Δw is a strong predictor of deflection throughout the test, and the relationship between Δw and peak deflection is nearly the same before and after the pause. This analysis illustrates how the vertical deflection (hence the load-induced strain) in clay depends on, and is sensitive to, the initial *w*.

When load-induced deflections increase with no change in load-induced vertical stress, this indicates an effective decrease in modulus. Researchers estimated the in situ modulus as the ratio of vertical stress to vertical strain at the top of the subgrade. The vertical compressive strain from CS is the measured vertical deflection divided by the initial spacing of the coils at construction (nominally 3 in.) (see Figure 42). Figure 56 presents the calculated modulus for LFC-5S as a function of traffic passes. The initial modulus for the initial 10 passes was estimated as 7,830 psi (54 MPa) from Figure 56. By comparison, the modulus measured using the LWD during construction was approximately 7,100 psi (49 MPa) (Tomlinson et al., 2022), which is sufficiently close to the sensor-measured modulus so that it may be considered validated. The sensor-measured modulus fell by approximately 72% during the first trafficking period and 80% in the second trafficking period. Figure 56 shows a recovery in modulus after the traffic pause to approximately 80% of the initial modulus.

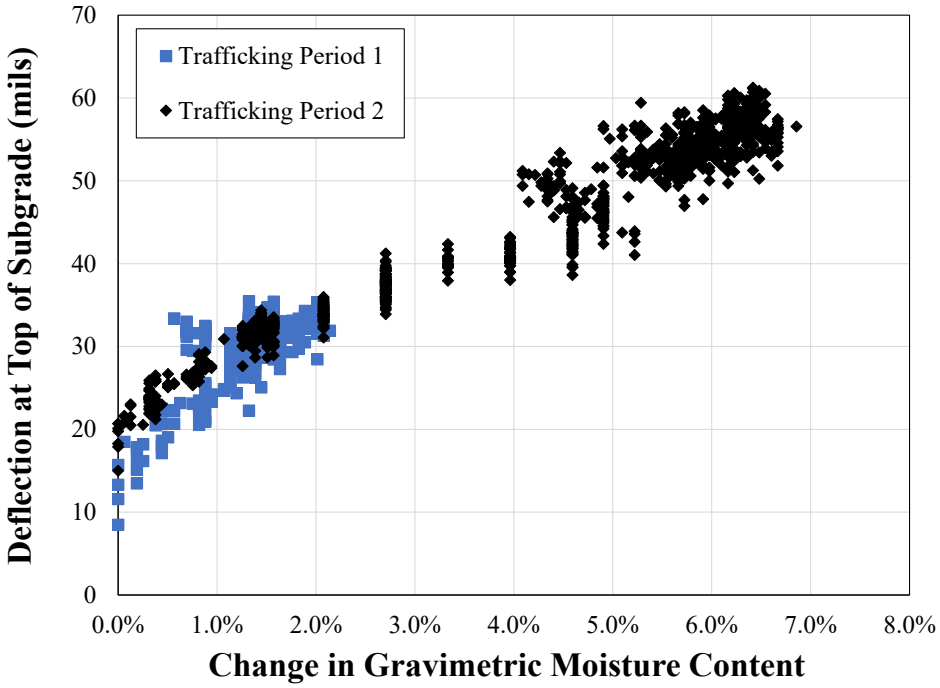

Figure 55. Top-of-Subgrade Average Deflection Versus Δw

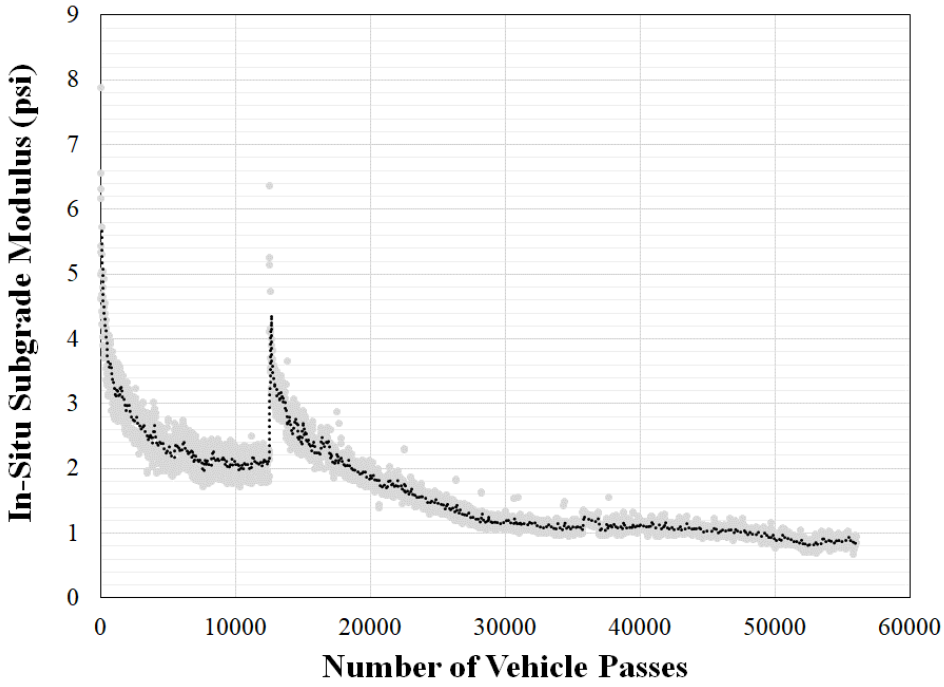

Figure 56. Change in Computed Subgrade Modulus During Traffic

Similar modulus decreases and recoveries for clay soils have been documented in the geotechnical literature, but in the context of soil shear strength under repetitive loading. White

and Hodder (2010) reported a cyclic T-bar penetrometer test where a cyclic load was applied in three separate phases. There was a 3.5-hour rest period between phases. The researchers found that the operative soil shear strength reduced under cyclic loading, attributing this behavior to several potential causes including excess pore pressure (White & Hodder, 2010). Later research attributed the shear strength reduction to excess pore pressure accumulation (White et al., 2022). This theory concurs with some of the CC9 observations. However, it is only one possible scenario, and it remains unclear if the dynamic nature of the MC in the clay subgrade is related to the environment, loading conditions, or some combination.

The key findings from the subgrade response analysis were as follows:

- During traffic, the peak vertical deflection under the wheel load at the top of the subgrade increased under repeated vehicle passes, while the corresponding peak vertical stress at the top of the subgrade remained relatively constant. Minimal change in the vertical stress indicated that the change in vertical deflection was not associated with permanent deformation or material changes above the subgrade.

- The magnitude of vertical deflection in the subgrade decreased after the 5-month pause in traffic compared to immediately prior. The peak load-induced vertical deflection in the subgrade after the traffic pause was similar to the deflection at the start of traffic (approximately 0.05 mm difference), indicating recovery in the subgrade.

- The moisture content fluctuated throughout the course of the experiment (in the range of 26% to 33%), even though the test section was covered and not exposed to any external sources of moisture.

- There was a strong correlation between Δw (referenced to w at the start of traffic) and vertical deflection in the subgrade. The initial w is an important factor for predicting vertical deflection of clay soil.

- No correlation was found between the measured absolute w and the load-induced vertical deflection in the subgrade. Obtaining a relationship between vertical deflection and moisture content required separating the traffic periods (before and after the pause in traffic) and treating them as separate events.

- In situ modulus measurements showed a decrease during traffic and recovery (during a pause in traffic) that paralleled the trend in the vertical deflection measurements. Similar clay behavior was reported in literature pertaining to soil shear strength under repetitive loading.

5.6 OVERLOAD CRITERIA BASED ON SHEAR STRESS RATIO

Section 1.1 noted that the CC7 test identified limiting subgrade vertical strain as a possible basis for allowable overloads of flexible airport pavements. It seems logical to relate allowable overloads to the same mechanistic strain response used to calculate flexible ACR, i.e., vertical strain at the top of the subgrade. However, the results presented in Sections 5.2 and 5.5 demonstrate that the actual vertical strain at the top of the subgrade is highly variable and

strongly dependent on factors other than the aircraft load, in particular the MC and history of traffic loading (including rest periods). Moreover, the linear elastic response model used in ACR computations (LEAF) does not capture the highly nonlinear and moisture-dependent strain response of the clay material. Therefore, it is difficult to establish a repeatable, realistic vertical strain value that corresponds to an allowable overload.

By contrast, the in situ measurements of top-of-subgrade vertical stress were relatively stable and relatable to the computed stress. Previous research by Bejarano and Thompson (1999, 2001), found that the ratio of computed subgrade shear stress to unconfined shear strength, designated shear stress ratio (SSR), is a suitable mechanistic predictor of rutting performance of flexible pavements on clay subgrades. They proposed a design model based on SSR in lieu of subgrade strain for flexible pavements. The discussion that follows shows that SSR is a useful quantity for explaining the failure (or lack of failure) of individual overload test items in CC7 and CC9. The full-scale test results suggest that an SSR-based overload criterion is feasible and would have advantages over both an alternative criterion based on LEAF-computed vertical strain and the current default criterion allowing 10% ACR above published PCR. However, an SSR-based model requires the additional input of laboratory-determined shear strength, which is not part of the current PCR computation. Furthermore, its application in practice would be restricted to flexible pavements on cohesive subgrades for which a reliable value of unconfined shear strength can be determined.

The limiting SSR method is premised on preventing shear failure in an unbound layer. The Mohr-Coulomb plasticity model is one model for evaluating shear failure in unbound materials. The Mohr-Coulomb model relates the normal and shear stresses at failure to the cohesion and angle at which the shear failure occurs (friction angle). In many cases, it is convenient to express the Mohr-Coulomb failure model as a function of the major and minor principal stresses (Equation 10).

$$\sigma_1 \left(\frac{1+\sin(\varphi)}{2c\cos(\varphi)}\right) - \sigma_3 \left(\frac{1-\sin(\varphi)}{2c\cos(\varphi)}\right) = 1 \quad (10)$$

where:

σ_1, σ_3 = major and minor principal stresses
c = soil cohesion
φ = friction angle

Equation (10) represents a critical yield surface in which any combination of principal stresses and material properties that causes the left-hand side to exceed 1.0 indicates soil failure. For CC7 and CC9, the subgrade was assumed to be fully (or close to fully) saturated cohesive soils where the friction angle is equal to 0°. With this assumption, Equation (10) simplifies to Equation (11). Equation (11) is in the form of a critical SSR where the maximum shear stress, defined as one-half the difference between principal stresses, is related to the ultimate cohesive strength of the soil.

$$\left(\frac{\sigma_1-\sigma_3}{2c}\right) = 1 \quad (11)$$

The left-hand side of Equation (11) is one form of SSR, in which cohesion *c* measures unconfined shear strength. In theory, initiating failure requires satisfying the condition SSR = 1.0, as shown in Equation (11). In practice, inherent variability during construction, averaging of material property values, and other heterogeneities create the potential for premature failure. To determine a suitable SSR for overload conditions, researchers performed both layered elastic analysis (LEA) and finite element analysis (FEA) to compute the pavement responses associated with the CC7 and CC9 overload test items. FEA was included because, although LEA is used in FAARFIELD for design and ACR/PCR calculations, it may not accurately capture shear stress from wheel load interactions due to gear load superposition. LEA and FEA were performed using FAARFIELD (LEAF) and ABAQUS (a commercial FEA software), respectively. In this analysis, SSR is more conveniently defined as the ratio of computed maximum shear stress τ_{Max} at the top of the subgrade to unconfined shear strength s_u determined from the QS test at zero confining pressure following the AASHTO T 307 procedure (AASHTO, 2021):

$$SSR = \tau_{Max}/s_u \tag{12}$$

The pavement structure for the stress analysis was an idealized representation of the CC7 and CC9 test items. As noted in Section 2. , the same design was used for the CC7 and CC9 overload test items, consisting of 3-in. P-401 asphalt, 6-in. crushed aggregate base, and 20-in. aggregate subbase on CBR 5 clay subgrade. In both tests, the assumed normal (non-overload) traffic was a D aircraft gear at 36,000 lb per wheel. Assuming 6,500 total passes, the FAARFIELD-computed PCR was 352.6/F/D (see Section 4.1). Table 17 summarizes the critical overload conditions for each test item in CC7 and CC9. Brill and Yin (2018) gave details and analysis of the CC7 overload tests based on ACN/PCN. For comparison with CC9, the CC7 percent overloads in Table 17 have been recalculated using the ACR/PCR system.

Table 17. Critical Gear Loads on CC7 and CC9

Test Item	Gear Type	Gear Load, lb	Wheel Load, lb	ACR/F/D	Percent Overload
CC7 LFC-1S	D	100,000	50,000	517.1	46.7
CC7 LFC-2S	2D	176,000	44,000	564.5	60.2
CC7 LFC-3S	3D	252,000	42,000	621.4	76.3
CC7 LFC-4S	3D	300,000	50,000	882.9	150.5
CC7 LFC-5S	2D	218,000	54,500	799.0	126.7
CC7 LFC-6S	D	125,000	62,500	680.2	93.0
CC9 LFC5N	D	114,000	57,000	616.2	74.9
CC9 LFC5S	D	72,000	36,000	352.4	none

A finite element (FE) model was constructed such that ABAQUS and LEAF give nearly equal responses for a single wheel load of 50,000 lb. The model details are provided in Appendix F. FE and LEA models incorporated the same material and interface assumptions, but the FEA model relaxes the LEA limitations to allow simultaneous multiple loads. Figure 57 shows example input to the models for a 3D overload gear.

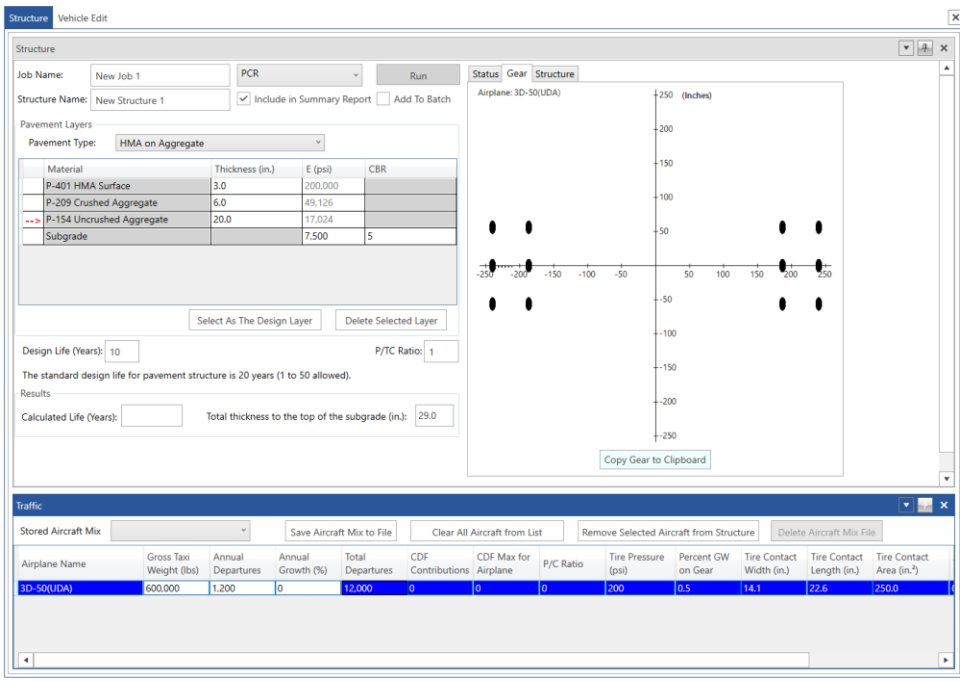

(a)

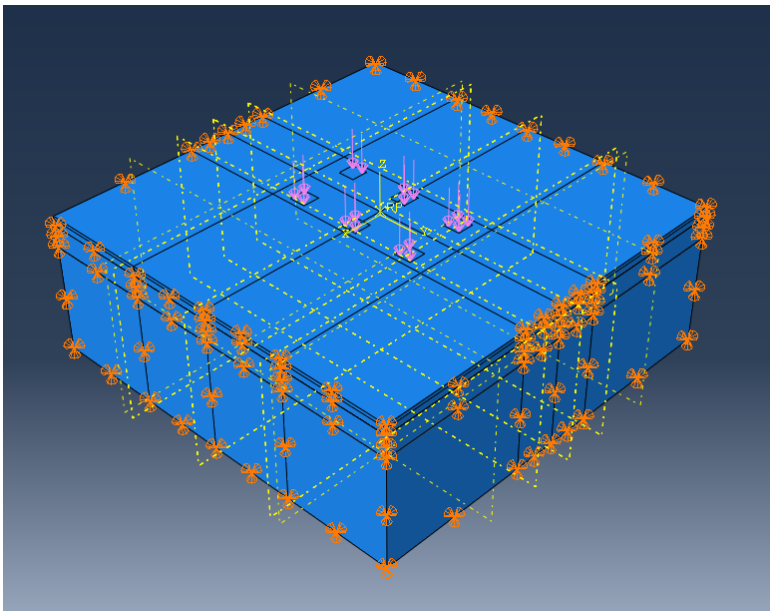

(b)

Figure 57. Overload Aircraft Gear Load Simulations Using (a) FAARFIELD and (b) ABAQUS

Table 18 shows the computed output for the cases in Table 17. In Table 16, the columns for w and s_u correspond to the data in Table 7 for the two CC9 test items. Similar laboratory tests were performed on Shelby tube samples retrieved from CC7

test items, and the data are provided here. For unconfined test conditions, the unconfined shear strength may be taken as one-half the maximum compressive strength from the QS test:

$$s_u = q_u/2 \tag{13}$$

Table 18. Maximum Shear Stress and SSR for CC7 and CC9 Overload Test Items

Test Item	Moisture Content w, %	Unconfined Shear Strength s_u, psi	FAARFIELD (LEAF)		ABAQUS	
			τ_{oct}, top of subgrade, psi	SSR	τ_{oct}, top of subgrade, psi	SSR
CC7 LFC-1S	27.1	11.5	8.30	0.721	8.23	0.715
CC7 LFC-2S	27.0	13.0	7.49	0.576	7.36	0.566
CC7 LFC-3S	26.6	8.0	7.52	0.940	7.44	0.930
CC7 LFC-4S	28.0	7.5	8.86	1.181	8.78	1.171
CC7 LFC-5S	27.4	11.0	9.21	0.837	9.04	0.822
CC7 LFC-6S	27.5	10.0	10.17	1.017	10.12	1.012
CC9 LFC-5N	23.5	16.8	9.36	0.557	9.23	0.549
CC9 LFC-5S	25.4	13.0	6.11	0.470	6.00	0.462

Although SSRs were computed for a range of overload levels (as shown in Table 17), it remains unclear what is and is not a safe and allowable SSR. Initially, researchers compared the SSR from Table 18 with the CC7 test results. Brill and Yin (2018) reported that LFC-3S and LFC-6S failed first when using 1.0 in. (25 mm) of surface upheaval as the failure criteria. From Table 18, LFC-3S and LFC-6S both had SSR near the Mohr-Coulomb yield surface, indicating that an SSR overload criteria of 1.0 may be adequate for predicting subgrade shear failure for saturated clays. However, previous studies pointed to a more conservative SSR threshold considering the instability of saturated clays. Bejarano and Thompson (1999, 2001) proposed limiting SSR to between 0.50 and 0.60 for design because the laboratory-measured permanent deformation of clay subgrades remains stable when SSR is below this range.

Bejarano and Thompson (1999, 2001) sought to establish a design methodology rather than a criterion for short-term operations, making their SSR criterion overly conservative for overload evaluations. CC7 and CC9 test results suggest that a reasonably limiting overload criterion, considering the behavior of saturated clays, is SSR = 0.75. Equation (14) directly incorporates this criterion in the traditional Mohr-Coulomb failure model through a factor of safety:

$$\sigma_1 \left(\frac{1+\sin(\varphi)}{2c\cos(\varphi)}\right) - \sigma_3 \left(\frac{1-\sin(\varphi)}{2c\cos(\varphi)}\right) = {}^{1}/_{\beta} \tag{14}$$

where:

β = factor of safety, 1.33

To demonstrate the possible application, Table 19 is a re-creation of Table 17 with the maximum allowable aircraft weight determined according to the limiting criterion SSR = 0.75. To determine the maximum loads from the model, gear loads were increased in 5,000-lb increments

until the maximum FAARFIELD-computed τ_{oct}, or they exceeded s_u. Table 17 also shows ACR determined for this gear and weight, and the percentage overload as computed by ACR/PCR procedures. Clearly, the SSR method does not correlate with the current overload evaluation method or the Annex 14 standard of 10% overload allowance.

Table 19. Maximum Allowable Overload for CC7 and CC9 Test Items Using SSR = 0.75

Test Item	Gear Type	Gear Load, lb	Unconfined Shear Strength s_u, psi	ACR/F/D	Percent Overload
CC7 LFC-1S	D	115,000	11.5	614.0	74.2
CC7 LFC-2S	2D	230,000	13.0	874.5	148.2
CC7 LFC-3S	3D	195,000	8.0	392.1	11.3
CC7 LFC-4S	3D	185,000	7.5	361.1	2.5
CC7 LFC-5S	2D	195,000	11.0	666.5	89.1
CC7 LFC-6S	D	95,000	10.0	485.9	37.9
CC9 LFC5N	D	175,000	16.8	1032.9	193.1
CC9 LFC5S	D	130,000	13.0	713.8	102.6

SSR is appealing as a technical overload criterion because it has physical meaning and is easily interpreted in terms of strength of materials. It requires knowledge of additional information that is not part of the ACR/PCR evaluation procedure, i.e., a value of the unconsolidated-undrained (UU) strength of cohesive materials in place, and this property is dependent on in-place moisture. However, the laboratory tests to determine the UU strength are relatively quick and inexpensive. Applicable tests in the United States include ASTM D2166 (*Standard Test Method for Unconfined Compressive Strength of Cohesive Soil*) (ASTM, 2024), AASHTO T 208 or the QS test provided under AASHTO T 307, *Standard Method of Test for Determining the Resilient Modulus of Soils and Aggregate Materials* (AASHTO, 2025). Alternatively, ASTM D2850 (ASTM, 2026) can be used to estimate the UU strength under in situ confinement.

In practice, the criterion of 0.75 SSR can serve as an upper limit for one-time or very occasional overload events. In cases where the overload ACR exceeds 10% over PCR but the SSR is less than an appropriate threshold (0.5–0.6, based on Bejarano & Thompson, 1999), this information may be used by engineers to justify more frequent overload operations.

6. CONCLUSIONS

The following are key observations from the CC9 overload test.

- Overloads up to 75% above PCR did not noticeably affect flexible pavement life.
- Neither test item reached the preset failure condition of 1-in. surface upheaval after more than 56,000 passes. However, both test items exhibited significant rutting combined with extensive interconnected (alligator) cracking by the end of the test.

- The overload test item exhibited higher cracking severity after the second overload. However, at the end of the test, conditions were nearly equal.

- Subgrade compressive strains as measured by CSs were much higher than LEAF strains at the start of the test and continued to increase with traffic. Strains increased sharply under overload but returned to usual values with the resumption of normal traffic.

- Relatively higher MC in the subgrade layer of LFC-5S might have contributed to the increased accumulation of permanent deformation compared to LFC-5N.

- The subgrade failure criterion, central to the ACR/PCR system, does not accommodate fatigue distresses and associated failure of the asphalt concrete in overload test items.

- Many factors in addition to load magnitude may affect the critical strain in situ, including soil moisture variation, variation of asphalt stiffness with temperature, and diminishing structural capacity due to damage under load. Without additional information concerning nonlinear soil properties and the load history at the time of overload, development of specific critical strain thresholds to govern allowable overloads is not feasible.

- Full-scale test results on overload test items did not justify a technical overload criterion based on subgrade vertical strain, because of the highly nonlinear and moisture-dependent strain response of the subgrade clay material.

- An alternative technical overload criterion based on SSR is feasible for cohesive subgrades. However, it requires an estimate of the unconfined shear strength, which is not part of current practice for reporting pavement strength.

7. REFERENCES

American Association of State Highway and Transportation Officials (AASHTO). (2008). *Mechanistic- empirical pavement design guide—A manual of practice* (AASHTO MEPDG-1). American Association of State Highway and Transportation Officials, Washington, DC.

AASHTO. (2021). *Determining the resilient modulus of soils and aggregate materials* (AASHTO T 307-99). AASHTO, Washington, DC.

AASHTO. (2019). *Standard method of test for determining dynamic modulus of hot mix asphalt (HMA)* (AASHTO T 342-11). AASHTO, Washington, DC.

AASHTO. (2020). *Standard Method of Test for Determining the Fracture Potential of Asphalt Mixtures Using the Illinois Flexibility Index (I-FIT)* (AASHTO TP 124-20). AASHTO, Washington, DC.

AASHTO. (2021). *Determining the resilient modulus of soils and aggregate materials* (AASHTO T 307-99). AASHTO, Washington, DC.

AASHTO. (2025). *Standard Method of Test for Unconfined Compressive Strength of Cohesive Soil* (AASHTO T 208M/T 208). AASHTO, Washington, DC.

Ahlvin, R. G., Turnbull, W. J., Sale, J. P., & Maxwell, A. A. (1971). *Multiple-wheel heavy gear load pavement tests. Volume 1* (Technical Report No. AFWL-TR-70-113). Air Force Weapons Laboratory: Kirkland, New Mexico. https://apps.dtic.mil/sti/pdfs/AD0889705.pdf.

Al-Qadi, I. L., Ozer, H., Lambros, J., El Khatib, A., Singhvi, P., Khan, T., Rivera-Perez, J., & Doll, B. (2015). *Testing protocols to ensure performance of high asphalt binder replacement mixes using RAP and RAS* (Research Report No. FHWA-ICT-15-017). Illinois Center for Transportation, Springfield, IL. https://www.ideals.illinois.edu/items/89996

ASTM. (2015). *Standard test method for measuring rut-depth of pavement surfaces using a straightedge* (ASTM E1703/E1703M-10(2015)). ASTM International, West Conshohocken, PA.

ASTM. (2020). *Standard test method for airport pavement condition index surveys* (ASTM D5340-20). ASTM International, West Conshohocken, PA.

ASTM. (2021). *Standard Test Method for Determining Fracture Energy of Asphalt Mixtures Using the Disk-Shaped Compact Tension Geometry* (ASTM D7313-20). ASTM International, West Conshohocken, PA.

ASTM. (2024). *Standard Test Method for Unconfined Compressive Strength of Cohesive Soil* (ASTM D2166/D2166M-24). ASTM International, West Conshohocken, PA.

ASTM. (2026). *Standard Test Method for Unconsolidated-Undrained Triaxial Compression Test on Cohesive Soils* (ASTM D2850-26). ASTM International, West Conshohocken, PA.

Batioja-Alvarez, D., Garg, N., & Kazmee, H. (2024, December 24). High-temperature Indirect Tensile Test to Assess Asphalt Rutting Performance in Airfield Mixes. In Carter, A., Vasconcelos, K., & Dave, E. (Eds.), *14th International Conference on Asphalt Pavements ISAP2024 Montreal. ISAP APE 2024.* Springer, Cham. https://doi.org/10.1007/978-3-031-67252-1_116

Bejarano, M. O., & Thompson, M. R. (1999). *Subgrade soil evaluation for the design of airport flexible pavements*. Center of Excellence for Airport Pavement Research (COE) Report No. 8, University of Illinois at Urbana-Champaign, Urbana, Illinois.

Bejarano, M. O., & Thompson, M. R. (2001). Subgrade damage approach for the design of airport flexible pavements. in *Advancing Airfield Pavements, Proceedings of the 2001 Airfield Pavement Specialty Conference*, ASCE, pp. 45-58. https://doi.org/10.1061/40579(271)4

Bilodeau, J. P., & Doré, G. (2014). Stress distribution experienced under a portable light-weight deflectometer loading plate. *International Journal of Pavement Engineering*, *15*(6), 564–575. https://doi.org/10.1080/10298436.2013.772612

Brill, D. R., & Yin, H. (2018). Full-scale tests of aircraft overloads on airport flexible pavements. In Wang, Y., & McNerney, M. T. (Eds.), *International Conference on Transportation and Development 2018: Airfield and Highway Pavements—Selected Papers from the International Conference on Transportation and Development 2018*, 66–77. American Society of Civil Engineers. https://doi.org/10.1061/9780784481554.008

Carpenter, S. H., Ghuzlan, K. A., & Shen, S. (2003). Fatigue endurance limit for highway and airport pavements. *Transportation Research Record: Journal of the Transportation Research Board*, *1832*(1), 131–138. National Research Council. https://doi.org/10.3141/1832-16

Carpenter, S. H., & Jansen, M. (1997, August 17–20). Fatigue behavior under new aircraft loading conditions. *Proceedings of the 1997 Airfield Pavement Conference: Aircraft/Pavement Technology In the Midst of Change*. Seattle, Washington. 259–271. American Society of Civil Engineers.

Carpenter, S. H., & Shen, S. (2006). Dissipated energy approach to study hot-mix asphalt healing in fatigue. *Transportation Research Record: Journal of the Transportation Research Board*, *1970*(1), 178–185. https://doi.org/10.1177/0361198106197000119

Dawson, A. 1994. *The ε-mu System, User's Manual* (Second Edition). Nottingham, UK: University of Nottingham.

FAA. (2017). *FAARFIELD 1.42 Help File*. U.S. Department of Transportation. Retrieved from https://www.airporttech.tc.faa.gov/Products/Airport-Safety-Papers-Publications/Airport-Safety-Detail/faarfield-142

FAA. (2018). *Standards for Specifying Construction of Airports Part 6—Flexible Pavement, Item P-401 Asphalt Mix Pavement* (Advisory Circular 150/5370-10H), 263–292. U.S. Department of Transportation, Federal Aviation Administration. https://www.faa.gov/documentLibrary/media/Advisory_Circular/150-5370-10H.pdf

Garg, N. (1997). *Mechanistic-empirical evaluation of the Mn/ROAD low-volume road test sections* (Doctoral dissertation, University of Illinois at Urbana-Champaign). http://hdl.handle.net/2142/83443

Garg, N., Li, Q., & Brill, D. (2020). Accelerated pavement testing of perpetual pavement test sections under heavy aircraft loading at FAA's National Airport Pavement Test Facility. *Journal of Testing and Evaluation*, *48*(1), 107–119. ASTM International. https://doi.org/10.1520/JTE20180906

Hall, J. (1998). *National Airport Pavement Test Facility Test Pavement, 100% Submittal* [Unpublished report]. Prepared by DMJM/Cornell, A Joint Venture, for U.S. Army Corps of Engineers, August 28, 1998.

Hoffman, M. S., & Thompson, M. R. (1981). *Mechanistic interpretation of nondestructive pavement testing deflections*. Civil Engineering Studies, Transportation Engineering Series No. 32, University of Illinois at Urbana-Champaign.

ICAO. (2020). Amendment 15 to Annex 14 — Aerodromes, Volume 1 — Aerodrome Design and Operations Doc 9157, Aerodrome Design Manual, Part 3 – Pavements. *Aerodrome design manual*.

ICAO. (2022). Annex 14 to the Convention on International Civil Aviation – Aerodromes. Volume I, *Aerodrome design and operations* (9th ed.).

Johanneck, L., Geib, J., Van Deusen, D. Garrity, J., Hanson, C., & Dave, E. V. (2015). *DCT Low Temperature Fracture Testing Pilot Project* (Research Report No. MN/RC 2015-20). Minnesota Department of Transportation, St. Paul, MN.. https://mdl.mndot.gov/items/201520

Jumikis, A. R. (1977). *Thermal geotechnics*. Rutgers University Press, New Brunswick, NJ.

Kazmee, H., Garg, N., & Ricalde, L. (2022). Estimating asphalt concrete strains in airport pavements using geometric property of the pavement surface deflection basin from heavy weight deflectometer tests. In Hoff, Saba, I. R., & Mork, H. (Eds.), *Proceedings of the Eleventh International Conference on the Bearing Capacity of Roads, Railways and Airfields, Volume 3*, 22–32. https://doi.org/10.1201/9781003222910-3?urlappend=%3Futm_source%3Dresearchgate.net%26utm_medium%3Darticle

Kazmee, H., Garg, N., Tomlinson, C., Ricalde, L., & Myriam, L. (2019). Warm mix asphalt (WMA) for airport pavements—Relating laboratory test results to performance under accelerated pavement testing (APT). *Journal of the Association of Asphalt Paving Technologists*, *88*, 221–248.

Kazmee, H., Murrell, S., Ricalde, L., Parsons, T., Duah, E., & Brill, D. R. (2026). *National Airport Pavement Test Facility Construction Cycle 9: Volume 1—Traffic Test Summary* (DOT/FAA/TC-26/11). U.S. Department of Transportation, Federal Aviation Administration, Airport Engineering Division, Washington, DC.

Mazzotta, C., Murrell, S., Evans, D., & Breder, E. (2024). *Exploring Construction Cycle 9 with Nondestructive Testing: Innovations and Insights in Full-Scale Airport Pavement Testing* (in publication). U.S. Department of Transportation, Federal Aviation Administration, Airport Engineering Division, Washington, DC.

Mooney, M. A., & Miller, P. K. (2009). Analysis of lightweight deflectometer test based on in situ stress and strain response. *Journal of Geotechnical and Geoenvironmental Engineering*, *135*(2), 199–208. https://doi.org/10.1061/(ASCE)1090-0241(2009)135:2(199)

Nazarian, S., Baker, M., & Crain, K. (1993). *Development and testing of a seismic pavement analyzer* (Research Report No. SHRP-H-375). Strategic Highway Research Program, National Research Council. https://onlinepubs.trb.org/onlinepubs/shrp/SHRP-H-375.pdf

Rushing, J., Little, D., & Garg, N. (2012). Asphalt pavement analyzer used to assess rutting susceptibility of hot-mix asphalt designed for high tire pressure aircraft. *Transportation Research Record: Journal of the Transportation Research Board*, *2296*(1), 97–105. Transportation Research Board of the National Academies. https://doi.org/10.3141/2296-10

Selig, E. T., & Grangaard, O. H. (1970). A new technique for soil strain measurement. *Materials Research and Standards*, *10*(11), 19–21

Shen, S., & Carpenter, S. H. (2007). Development of an asphalt fatigue model based on energy principles. *Asphalt Paving Technology*, *76,* 525–574.

Tomlinson, C., Traverzo, D., Cary, C., & Brynick, M. (2022). *Construction Cycle 9 (CC9) Construction Report* (DOT/FAA/TC-22/1). U.S. Department of Transportation, Federal Aviation Administration. https://www.airporttech.tc.faa.gov/Products/Airport-Pavement-Papers-Publications/Airport-Pavement-Detail/construction-cycle-9-cc9-construction-report

White, D. J., & Hodder, M. (2010). A simple model for the effect on soil strength of episodes of remoulding and reconsolidation. *Canadian Geotechnical Journal*, *47*(7), 821–826. https://doi.org/10.1139/T09-137

White, D. J., Doherty, J. P., Guevara, M., & Watson, P. G. (2022). A cyclic p-y model for the whole-life response of piles in soft clay. *Computers and Geotechnics*, *141*(5). https://doi.org/10.1016/j.compgeo.2021.104519

APPENDIX A—LAYOUT OF SENSORS IN OVERLOAD TEST ITEMS

Table A-1. Longitudinal Stations and Transverse Offsets of Embedded Sensors in Test Item LFC-5N

Sensor ID	Longitudinal Offset (ft)	Transverse Offset (ft)	Embedment Depth (in.)
CS-LFC5N-1	262.52	-17.27	30.58
CS-LFC5N-2	262.52	-17.27	33.58
CS-LFC5N-3	262.45	-12.79	30.48
CS-LFC5N-4	262.45	-12.79	33.48
LSG-LFC5N-1	245	-17.25	3
LSG-LFC5N-2	247	-17.25	3
LSG-LFC5N-3	245	-12.75	3
LSG-LFC5N-4	247	-12.75	3
LSG-LFC5N-5	276	-17.25	3
LSG-LFC5N-6	276	-12.75	3
MS-LFC5N-1	262.5	-15	35
MS-LFC5N-2	262.5	-15	42
PC-LFC5N-1	262.5	-15	9
PC-LFC5N-2	262.5	-15	29
T-LFC5N-1	262.5	-27	0
T-LFC5N-2	262.5	-27	1
T-LFC5N-3	262.5	-27	2
T-LFC5N-4	262.5	-27	3
TSG-LFC5N-1	249	-17.25	3
TSG-LFC5N-2	251	-17.25	3
TSG-LFC5N-3	249	-12.75	3
TSG-LFC5N-4	251	-12.75	3
TSG-LFC5N-5	278	-17.25	3
TSG-LFC5N-6	278	-12.75	3

Table A-2. Longitudinal Stations and Transverse Offsets of Embedded Sensors in Test item LFC-5S

Sensor ID	Longitudinal Offset (ft)	Transverse Offset (ft)	Embedment Depth (in.)
CS-LFC5S-1	262.44	17.19	30.66
CS-LFC5S-2	262.44	17.19	33.66
CS-LFC5S-3	262.46	12.77	30.58
CS-LFC5S-4	262.46	12.77	33.58
LSG-LFC5S-1	245	12.75	3
LSG-LFC5S-2	247	12.75	3
LSG-LFC5S-3	245	17.25	3
LSG-LFC5S-4	247	17.25	3
LSG-LFC5S-5	276	12.75	3
LSG-LFC5S-6	276	17.25	3
MS-LFC5S-1	262.5	15	35
PC-LFC5S-1	262.5	15	9
PC-LFC5S-2	262.5	15	29
TSG-LFC5S-1	249	12.75	3
TSG-LFC5S-2	251	12.75	3
TSG-LFC5S-3	249	17.25	3
TSG-LFC5S-4	251	17.25	3
TSG-LFC5S-5	278	12.75	3
TSG-LFC5S-6	278	17.25	3

APPENDIX B—MAXIMUM UPHEAVALS IN CONSTRUCTION CYCLE 9 OVERLOAD TEST ITEMS

Table B-1. Maximum Upheavals from Virtual Upheaval Calculator in CC9 Overload Test Items

Pass Number	Scan Date	LFC-5N STA 2+55		LFC-5N STA 2+70		LFC-5S STA 2+55		LFC-5S STA 2+70	
		Offset, ft[1]	Maximum Upheaval, in.	Offset, ft[1]	Maximum Upheaval, in.	Offset, ft[1]	Maximum Upheaval, in.	Offset, ft[1]	Maximum Upheaval, in.
6666	8/13/2021	-7.08	0.25	-8.08	0.2	21.92	0.2	6.25	0.12
12610	10/20/2021	-6.92	0.36	-8.08	0.25	21.92	0.31	22.08	0.17
13992	3/4/2022	-7.08	0.23	-6.42	0.13	22.25	0.16	6.25	0.08
15378	3/18/2022	-7.08	0.24	-6.42	0.13	22.58	0.2	23.42	0.09
16962	4/1/2022	-7.08	0.32	-6.42	0.22	22.08	0.26	6.25	0.17
18480	4/15/2022	-7.08	0.25	-6.58	0.11	22.25	0.18	22.92	0.09
20064	4/29/2022	-7.08	0.26	-6.42	0.15	22.08	0.21	6.25	0.1
22044	5/13/2022	-7.08	0.28	-6.42	0.18	22.08	0.22	23.42	0.14
23892	5/26/2022	-7.08	0.23	-7.08	0.1	22.58	0.18	23.08	0.06
25740	6/10/2022	-7.08	0.26	-6.42	0.14	22.08	0.19	6.25	0.08
27324	6/24/2022	-7.08	0.3	-7.08	0.17	22.58	0.23	22.92	0.11
33924	8/12/2022	-7.08	0.45	-7.92	0.28	21.92	0.4	7.92	0.2
35904	8/26/2022	-7.92	0.51	-7.92	0.33	21.92	0.44	7.92	0.24
37554	9/9/2022	-21.92	0.6	-7.92	0.36	22.08	0.51	7.92	0.28
38874	9/23/2022	-21.92	0.55	-7.92	0.32	22.08	0.47	22.08	0.25
40920	10/7/2022	-21.92	0.57	-22.08	0.31	21.92	0.51	22.08	0.26
43428	10/20/2022	-21.92	0.75	-22.25	0.36	21.92	0.51	22.08	0.26
47652	11/4/2022	-21.92	0.71	-22.08	0.31	21.92	0.47	22.08	0.23
51084	11/18/2022	-21.92	0.74	-7.92	0.34	22.08	0.48	22.08	0.26
54054	12/2/2022	-21.92	0.69	-22.25	0.28	21.92	0.44	22.08	0.2
56628	12/23/2022	-22.08	0.76	-7.58	0.4	22.08	0.52	22.08	0.31

[1] Negative offsets are north (left) of center of traffic. Positive offsets are south (right) of center of traffic.

APPENDIX C—VISUAL DISTRESS LOG

Table C-1. Log of Cracks Observed in Overload Test Item LFC-5N

Crack Number	Date of Recording	Start		End		Length of Crack (in.)
		X	Y	X	Y	
		(Offset from Centerline)	(Offset from Station)	(Offset from Centerline)	(Offset from Station)	
504	1-Jul-22	198	18 from 2+70↓	167	11 from 2+70↓	32
2283	1-Jul-22	180	10 from 2+70↓	179	13 from 2+70↓	3
2284	1-Jul-22	196	5 from 2+70↓	188	3.5 from 2+70↓	8
2285	1-Jul-22	188	2 from 2+70↑	188	3.5 from 2+70↓	1.5
2286	1-Jul-22	175	4 from 2+70↓	188	3.5 from 2+70↓	13
2287	1-Jul-22	215	16 from 2+70↑	224	14 from 2+70↑	9
2288	1-Jul-22	238.5	10 from 2+70↑	243	6 from 2+70↑	6
2289	1-Jul-22	224.5	19.5 from 2+70↑	229	17 from 2+70↑	5
2290	1-Jul-22	254	30 from 2+70↑	241.5	26 from 2+70↑	13
2291	1-Jul-22	254.5	58 from 2+70↑	240	57.5 from 2+70↑	14.5
2292	1-Jul-22	251	71.5 from 2+70↑	239	81 from 2+70↑	15.5
2293	1-Jul-22	238.5	63 from 2+70↑	232	71 from 2+70↑	10.5
2294	1-Jul-22	239	40 from 2+70↑	238	39.5 from 2+70↑	1
2295	1-Jul-22	239.5	39 from 2+70↑	238	39.5 from 2+70↑	1.5
2296	1-Jul-22	230	39.5 from 2+70↑	238	39.5 from 2+70↑	8
2297	1-Jul-22	233	28 from 2+70↑	230	27 from 2+70↑	3
2298	1-Jul-22	238	10.5 from 2+70↑	223.5	10 from 2+70↑	14.5
2299	1-Jul-22	216	25 from 2+70↑	223	23 from 2+70↑	7.5
328	1-Jul-22	214	27.5 from 2+70↑	198	26 from 2+70↑	16
2300	1-Jul-22	209	1 from 2+70↑	199.5	6 from 2+70↑	10.5
2301	1-Jul-22	193	7 from 2+70↑	199.5	5.5 from 2+70↑	6.5
2302	1-Jul-22	193.5	2.5 from 2+70↑	196.5	0 from 2+70↑	4
2303	1-Jul-22	193.5	2.5 from 2+70↑	193.5	4 from 2+70↑	1.5
2304	1-Jul-22	193.5	2.5 from 2+70↑	189	2.5 from 2+70↑	4.5
2305	1-Jul-22	197	26.5 from 2+70↑	192	33 from 2+70↑	8
2306	1-Jul-22	214	33 from 2+70↑	209.5	36 from 2+70↑	5.5
2307	1-Jul-22	204.5	47 from 2+70↑	208	54 from 2+70↑	8
2308	1-Jul-22	202	54.5 from 2+70↑	208	54 from 2+70↑	6
2309	1-Jul-22	212.5	87 from 2+70↑	208	88 from 2+70↑	4.5
2310	1-Jul-22	217	94.5 from 2+70↑	211.5	94 from 2+70↑	5.5
2311	1-Jul-22	223	98.5 from 2+70↑	211.5	94 from 2+70↑	12.5
2312	1-Jul-22	223	97.5 from 2+70↑	220.5	98 from 2+70↑	2.5
2313	1-Jul-22	223	97.5 from 2+70↑	211	98 from 2+70↑	12
2314	1-Jul-22	224.5	98 from 2+70↑	219	104 from 2+70↑	8
2315	1-Jul-22	219	61 from 2+70↑	217	67 from 2+70↑	6.5
2316	1-Jul-22	220	51 from 2+70↑	215	53 from 2+70↑	5.5
2317	1-Jul-22	214	50 from 2+70↑	215	53 from 2+70↑	3
2318	1-Jul-22	214	50 from 2+70↑	207	50.5 from 2+70↑	7
2319	1-Jul-22	198.5	93 from 2+70↑	194.5	93 from 2+70↑	4
2320	1-Jul-22	192	96 from 2+70↑	194.5	93 from 2+70↑	4
2321	1-Jul-22	196	71.5 from 2+70↑	183	72 from 2+70↑	13
2322	1-Jul-22	192	66.5 from 2+70↑	181	68 from 2+70↑	11
2323	1-Jul-22	185.5	81 from 2+70↑	179	78.5 from 2+70↑	7
2324	1-Jul-22	186	63 from 2+70↑	180	61 from 2+70↑	6.5

Crack Number	Date of Recording	Start		End		Length of Crack (in.)
		X	Y	X	Y	
		(Offset from Centerline)	(Offset from Station)	(Offset from Centerline)	(Offset from Station)	
846	1-Jul-22	186	55.5 from 2+70↑	174	56 from 2+70↑	12
2325	1-Jul-22	179	23 from 2+70↑	168	19.5 from 2+70↑	11.5
2326	1-Jul-22	178	15 from 2+70↑	167	21.5 from 2+70↑	13
2327	1-Jul-22	176	16 from 2+70↑	170	2.5 from 2+70↑	15
2328	1-Jul-22	166	18 from 2+70↑	166	21 from 2+70↑	3
2329	1-Jul-22	166	18 from 2+70↑	165	9 from 2+70↑	9
2330	1-Jul-22	169	86 from 2+70↑	159.5	77 from 2+70↑	13
2331	1-Jul-22	140.5	76 from 2+70↑	159.5	77 from 2+70↑	19
2332	1-Jul-22	158	79 from 2+70↑	159.5	77 from 2+70↑	2 1/2
2333	1-Jul-22	171	73.5 from 2+70↑	169	68 from 2+70↑	6
2334	1-Jul-22	173.5	64.5 from 2+70↑	169	68 from 2+70↑	5 1/2
2335	1-Jul-22	165	64 from 2+70↑	169	68 from 2+70↑	5 1/2
2336	1-Jul-22	165	64 from 2+70↑	172	60 from 2+70↑	8
2337	1-Jul-22	165	64 from 2+70↑	145.5	67.5 from 2+70↑	20
2338	1-Jul-22	177	35 from 2+70↑	166	32 from 2+70↑	11 1/2
2339	1-Jul-22	170.5	28.5 from 2+70↑	166	32 from 2+70↑	5 1/2
2340	1-Jul-22	164	33 from 2+70↑	166	32 from 2+70↑	2
2341	1-Jul-22	189	45 from 2+70↑	164.5	52 from 2+70↑	25 1/2
2342	1-Jul-22	145	48 from 2+70↑	164.5	52 from 2+70↑	20
2343	1-Jul-22	177	37 from 2+70↑	174	41 from 2+70↑	5
2344	1-Jul-22	176.5	42 from 2+70↑	174	41 from 2+70↑	2 1/2
2345	1-Jul-22	153.5	44.5 from 2+70↑	174	41 from 2+70↑	21
2346	1-Jul-22	153.5	44.5 from 2+70↑	144	40 from 2+70↑	10 1/2
2347	1-Jul-22	156	35 from 2+70↑	145.5	32 from 2+70↑	11
2348	1-Jul-22	144.5	33 from 2+70↑	162.5	33.5 from 2+70↑	18
2349	1-Jul-22	146	26.5 from 2+70↑	163	25 from 2+70↑	17
2350	1-Jul-22	145	27 from 2+70↑	130	17.5 from 2+70↑	18
2351	1-Jul-22	170	52 from 2+70↑	172	55.5 from 2+70↑	4
2352	1-Jul-22	168	62 from 2+70↑	172	55 from 2+70↑	8
2353	1-Jul-22	109	55 from 2+70↑	123.5	58.5 from 2+70↑	15
2354	1-Jul-22	108.5	71 from 2+70↑	123	73.5 from 2+70↑	14 1/2
2355	1-Jul-22	123	80 from 2+70↑	118.5	86 from 2+70↑	7 1/2
2356	1-Jul-22	107	88 from 2+70↑	118.5	86 from 2+70↑	11 1/2
2357	1-Jul-22	121	88 from 2+70↑	118.5	86 from 2+70↑	3
2358	1-Jul-22	108	83 from 2+70↑	108	97 from 2+70↑	14
2359	1-Jul-22	108	83 from 2+85↓	108	61 from 2+85↓	22
2360	1-Jul-22	109	71.5 from 2+85↓	118	68.5 from 2+85↓	9 1/2
2361	1-Jul-22	121.5	62.5 from 2+85↓	118	68.5 from 2+85↓	7
2362	1-Jul-22	123	72 from 2+85↓	118	68.5 from 2+85↓	6
2363	1-Jul-22	120.5	59 from 2+85↓	106	55 from 2+85↓	15
2364	1-Jul-22	106	38 from 2+85↓	106	55 from 2+85↓	17
2365	1-Jul-22	106	38 from 2+85↓	105	36 from 2+85↓	2
2366	1-Jul-22	107	29 from 2+85↓	106	22 from 2+85↓	7
2367	1-Jul-22	107	25 from 2+85↓	119	23.5 from 2+85↓	12
2368	1-Jul-22	118	38 from 2+85↓	120.5	37 from 2+85↓	2 1/2
2369	1-Jul-22	123	52 from 2+85↓	142	43 from 2+85↓	21
2370	1-Jul-22	123	49 from 2+85↓	125	48 from 2+85↓	2
2371	1-Jul-22	124.5	41.5 from 2+85↓	142	39.5 from 2+85↓	17 1/2
2372	1-Jul-22	122	63 from 2+85↓	188.5	61 from 2+85↓	66 1/2

Crack Number	Date of Recording	Start		End		Length of Crack (in.)
		X	Y	X	Y	
		(Offset from Centerline)	(Offset from Station)	(Offset from Centerline)	(Offset from Station)	
2373	1-Jul-22	209	67.5 from 2+85↓	188.5	61 from 2+85↓	21 1/2
2374	1-Jul-22	143.5	104.5 from 2+85↓	130	104 from 2+85↓	13 1/2
2375	1-Jul-22	124	100 from 2+85↓	130	104 from 2+85↓	7
2376	1-Jul-22	117.5	107 from 2+85↓	130	104 from 2+85↓	13
2377	1-Jul-22	142	72.5 from 2+85↓	131	71 from 2+85↓	11
2378	1-Jul-22	130.5	83 from 2+85↓	138	82 from 2+85↓	7 1/2
2379	1-Jul-22	141	75 from 2+85↓	138	82 from 2+85↓	7 1/2
2380	1-Jul-22	146	88.5 from 2+85↓	130	88.5 from 2+85↓	16
2381	1-Jul-22	141	74 from 2+85↓	144	76.5 from 2+85↓	4
2382	1-Jul-22	169	76.5 from 2+85↓	144	76.5 from 2+85↓	25
2383	1-Jul-22	169	76.5 from 2+85↓	178	72 from 2+85↓	10
2384	1-Jul-22	169	76.5 from 2+85↓	170	78 from 2+85↓	2
2385	1-Jul-22	175	83 from 2+85↓	170	78 from 2+85↓	7
2386	1-Jul-22	163	80 from 2+85↓	170	78 from 2+85↓	7 1/2
2387	1-Jul-22	183	53 from 2+85↓	181	54 from 2+85↓	2
2388	1-Jul-22	178	52 from 2+85↓	181	54 from 2+85↓	3 1/2
2389	1-Jul-22	178	52 from 2+85↓	180	50 from 2+85↓	3
2390	1-Jul-22	178	52 from 2+85↓	175	55.5 from 2+85↓	4 1/2
2391	1-Jul-22	171	56 from 2+85↓	175	55.5 from 2+85↓	4
2392	1-Jul-22	171	56 from 2+85↓	174	59 from 2+85↓	4
2393	1-Jul-22	162.5	56.5 from 2+85↓	174	59 from 2+85↓	12
2394	1-Jul-22	251.5	63.5 from 2+85↓	249	63.5 from 2+85↓	2 1/2
2395	1-Jul-22	249.5	56 from 2+85↓	248	60 from 2+85↓	4 1/2
2396	1-Jul-22	244.5	62 from 2+85↓	248	60 from 2+85↓	4
2397	1-Jul-22	244.5	62 from 2+85↓	238.5	59 from 2+85↓	6 1/2
2398	1-Jul-22	244.5	62 from 2+85↓	236.5	68.5 from 2+85↓	10 1/2
2399	1-Jul-22	249	44 from 2+85↓	243	45 from 2+85↓	6
2400	1-Jul-22	248	38.5 from 2+85↓	242.5	36 from 2+85↓	6
2401	1-Jul-22	242.5	33.5 from 2+85↓	242.5	37 from 2+85↓	3 1/2
2402	1-Jul-22	239	43 from 2+85↓	232.5	43 from 2+85↓	6 1/2
2403	1-Jul-22	217.5	56 from 2+85↓	208.5	54.5 from 2+85↓	9
2404	1-Jul-22	219.5	65 from 2+85↓	224.5	66.5 from 2+85↓	5
2405	1-Jul-22	220.5	67 from 2+85↓	224.5	66.5 from 2+85↓	4
2406	1-Jul-22	225	70 from 2+85↓	224.5	66.5 from 2+85↓	3 1/2
2407	1-Jul-22	206.5	74 from 2+85↓	212.5	79 from 2+85↓	8
2408	1-Jul-22	212.5	83 from 2+85↓	212.5	79 from 2+85↓	4
2409	1-Jul-22	218	76 from 2+85↓	212.5	79 from 2+85↓	6 1/2
2410	1-Jul-22	212.5	83 from 2+85↓	207	83.5 from 2+85↓	5 1/2
2411	1-Jul-22	154.5	42 from 2+85↓	153	38.5 from 2+85↓	4
2412	1-Jul-22	144	40.5 from 2+85↓	153	38.5 from 2+85↓	9
2413	1-Jul-22	142	13 from 2+85↓	121	20.5 from 2+85↓	22 1/2
2414	1-Jul-22	143.5	3.5 from 2+85↓	134	2.5 from 2+85↓	9 1/2
2415	1-Jul-22	162.5	14 from 2+85↓	171	12 from 2+85↓	8 1/2
2416	1-Jul-22	173	16.5 from 2+85↓	183	13 from 2+85↓	10 1/2
2417	1-Jul-22	184	38.5 from 2+85↓	191	40.5 from 2+85↓	7 1/2
2418	1-Jul-22	193	35.5 from 2+85↓	188	34 from 2+85↓	5
2419	1-Jul-22	164	32.5 from 2+85↓	164	47 from 2+85↓	14 1/2
2420	1-Jul-22	162.5	35 from 2+85↓	153.5	32 from 2+85↓	9 1/2
1572	1-Jul-22	153	28 from 2+85↓	144	31 from 2+85↓	9 1/2

Crack Number	Date of Recording	Start		End		Length of Crack (in.)
		X	Y	X	Y	
		(Offset from Centerline)	(Offset from Station)	(Offset from Centerline)	(Offset from Station)	
2421	1-Jul-22	144.5	18 from 2+85↓	153	18.5 from 2+85↓	8 1/2
2422	1-Jul-22	143	32 from 2+85↓	138	34 from 2+85↓	5 1/2
2423	1-Jul-22	131	33 from 2+85↓	138	34 from 2+85↓	7
2424	1-Jul-22	131	33 from 2+85↓	125.5	35.5 from 2+85↓	6
2425	1-Jul-22	164	1 from 2+85↓	162	4 from 2+85↓	3 1/2

Table C-2. Log of Cracks Observed in Control Test Item LFC-5S

Crack Number	Date of Recording	Start		End		Length of Crack (in.)
		X	Y	X	Y	
		(Offset from Centerline)	(Offset from Station)	(Offset from Centerline)	(Offset from Station)	
2608	12-Jul-22	99	20 from 2+70↓	106.5	15 from 2+70↓	9
2609	12-Jul-22	123	45 from 2+70↓	125	41 from 2+70↓	4 1/2
2610	12-Jul-22	142	24.5 from 2+70↓	147.5	25 from 2+70↓	5 1/2
2611	12-Jul-22	149.5	22 from 2+70↓	147.5	25 from 2+70↓	3 1/2
2612	12-Jul-22	149.5	22.5 from 2+70↓	153	22 from 2+70↓	3 1/2
2613	12-Jul-22	155.5	23.5 from 2+70↓	153	22 from 2+70↓	3
2614	12-Jul-22	155.5	23.5 from 2+70↓	155	29 from 2+70↓	5 1/2
2615	12-Jul-22	155.5	23.5 from 2+70↓	158	20 from 2+70↓	4 1/2
2616	12-Jul-22	145	8 from 2+70↓	149	7.5 from 2+70↓	4
2617	12-Jul-22	156.5	13 from 2+70↓	162	11.5 from 2+70↓	5 1/2
2618	12-Jul-22	156	4 from 2+70↓	162	3.5 from 2+70↓	6
2619	12-Jul-22	146.5	52.5 from 2+70↓	150.5	51 from 2+70↓	4 1/2
2620	12-Jul-22	151	53 from 2+70↓	150.5	51 from 2+70↓	2
2621	12-Jul-22	108	58.5 from 2+70↓	120.5	62.5 from 2+70↓	13
2622	12-Jul-22	122.5	62.5 from 2+70↓	120.5	62.5 from 2+70↓	2
2623	12-Jul-22	238	0.5 from 2+70↓	249.5	4.5 from 2+70↓	12
2624	12-Jul-22	234.5	29 from 2+70↑	225.5	29.5 from 2+70↑	9
2625	12-Jul-22	252	29 from 2+70↑	252.5	21.5 from 2+70↑	7 1/2
2626	12-Jul-22	251.5	30 from 2+70↑	251	45.5 from 2+70↑	15 1/2
2627	12-Jul-22	251	34 from 2+70↑	242.5	37 from 2+70↑	9
2628	12-Jul-22	247	64 from 2+70↑	250	65.5 from 2+70↑	3 1/2
2629	12-Jul-22	252.5	82.5 from 2+70↑	250	65.5 from 2+70↑	17
2630	12-Jul-22	252.5	82.5 from 2+70↑	247	87 from 2+70↑	7
2631	12-Jul-22	253	87 from 2+70↑	247	87 from 2+70↑	6
2632	12-Jul-22	244	87 from 2+70↑	247	87 from 2+70↑	3
2633	12-Jul-22	241	77.5 from 2+70↑	235	79.5 from 2+70↑	6 1/2
1793	12-Jul-22	234	78.5 from 2+70↑	229	80 from 2+70↑	5
2634	12-Jul-22	230	90 from 2+70↑	229	92 from 2+70↑	2
2635	12-Jul-22	217	95 from 2+70↑	229	92 from 2+70↑	12 1/2
2636	12-Jul-22	251	90 from 2+70↑	252	106 from 2+70↑	16
2637	12-Jul-22	235.5	106 from 2+70↑	252	106 from 2+70↑	16 1/2
2638	12-Jul-22	235	106 from 2+70↑	216.5	104 from 2+70↑	18 1/2
2639	12-Jul-22	216	106 from 2+70↑	216.5	104 from 2+70↑	2
2640	12-Jul-22	216	106 from 2+70↑	212	108 from 2+70↑	4 1/2
2641	12-Jul-22	218	36 from 2+70↑	218	47 from 2+70↑	11

Crack Number	Date of Recording	Start		End		Length of Crack (in.)
		X (Offset from Centerline)	Y (Offset from Station)	X (Offset from Centerline)	Y (Offset from Station)	
2642	12-Jul-22	216.5	40.5 from 2+70↑	208.5	41.5 from 2+70↑	8
2643	12-Jul-22	196.5	86 from 2+70↑	196.5	93 from 2+70↑	7
2644	12-Jul-22	206	33 from 2+70↑	197	33 from 2+70↑	9
2645	12-Jul-22	207	44.5 from 2+70↑	198	42 from 2+70↑	9 1/2
2646	12-Jul-22	207	48.5 from 2+70↑	197.5	48.5 from 2+70↑	9 1/2
2647	12-Jul-22	188.5	35.5 from 2+70↑	197.5	35.5 from 2+70↑	9
2648	12-Jul-22	193	52 from 2+70↑	192	53.5 from 2+70↑	2
2649	12-Jul-22	187.5	53.5 from 2+70↑	192	53.5 from 2+70↑	4 1/2
2650	12-Jul-22	181.5	64.5 from 2+70↑	181	62 from 2+70↑	2 1/2
2651	12-Jul-22	175	64 from 2+70↑	168	62.5 from 2+70↑	7
2652	12-Jul-22	173	75 from 2+70↑	161.5	74.5 from 2+70↑	11 1/2
2653	12-Jul-22	173	81.5 from 2+70↑	147.5	80 from 2+70↑	25 1/2
2654	12-Jul-22	141.5	75 from 2+70↑	147.5	80 from 2+70↑	8
2655	12-Jul-22	169	66 from 2+70↑	155.5	67.5 from 2+70↑	13 1/2
2656	12-Jul-22	160	57 from 2+70↑	160.5	67 from 2+70↑	10
2657	12-Jul-22	181.5	64 from 2+70↑	178.5	61.5 from 2+70↑	4
2658	12-Jul-22	175	59 from 2+70↑	178.5	61.5 from 2+70↑	4 1/2
2659	12-Jul-22	175	59 from 2+70↑	162.5	55 from 2+70↑	13
2660	12-Jul-22	153	58 from 2+70↑	162.5	55 from 2+70↑	10
2661	12-Jul-22	153	58 from 2+70↑	149.5	57 from 2+70↑	3 1/2
2662	12-Jul-22	179	42 from 2+70↑	174.5	37 from 2+70↑	6 1/2
2663	12-Jul-22	165.5	36.5 from 2+70↑	174.5	37 from 2+70↑	9
2664	12-Jul-22	187.5	25 from 2+70↑	174	27 from 2+70↑	13 1/2
2665	12-Jul-22	176	32 from 2+70↑	174	27 from 2+70↑	5 1/2
2666	12-Jul-22	176	32 from 2+70↑	187	36 from 2+70↑	11 1/2
2667	12-Jul-22	164.5	24.5 from 2+70↑	174	27 from 2+70↑	10
2668	12-Jul-22	164.5	24.5 from 2+70↑	157	29 from 2+70↑	8 1/2
2669	12-Jul-22	152	31 from 2+70↑	157	29 from 2+70↑	5 1/2
2670	12-Jul-22	156	44 from 2+70↑	155	48 from 2+70↑	4
2671	12-Jul-22	152.5	50 from 2+70↑	155	48 from 2+70↑	3
2672	12-Jul-22	149	51.5 from 2+70↑	152	58 from 2+70↑	7
2673	12-Jul-22	152	41 from 2+70↑	141.5	41 from 2+70↑	10 1/2
2674	12-Jul-22	147.5	80 from 2+70↑	148.5	89.5 from 2+70↑	9 1/2
2675	12-Jul-22	141.5	89.5 from 2+70↑	148.5	89.5 from 2+70↑	7
2676	12-Jul-22	159	95.5 from 2+70↑	148.5	89.5 from 2+70↑	12
2677	12-Jul-22	146.5	57 from 2+70↑	137.5	58 from 2+70↑	9
2678	12-Jul-22	138.5	37 from 2+70↑	128.5	34 from 2+70↑	10 1/2
2679	12-Jul-22	139	25.5 from 2+70↑	125.5	26.5 from 2+70↑	13 1/2
2680	12-Jul-22	126.5	31.5 from 2+70↑	125.5	26.5 from 2+70↑	5
1837	12-Jul-22	133.5	7.5 from 2+70↑	118	4.5 from 2+70↑	16
2681	12-Jul-22	122	51 from 2+70↑	132.5	58.5 from 2+70↑	13
2682	12-Jul-22	106.5	64 from 2+70↑	107.5	52 from 2+70↑	12
2683	12-Jul-22	106.5	78 from 2+70↑	109	85 from 2+70↑	7 1/2
2684	12-Jul-22	122.5	89.5 from 2+70↑	135.5	94.5 from 2+70↑	14
2685	12-Jul-22	108.5	65 from 2+85↓	118.5	60 from 2+85↓	11
2686	12-Jul-22	108.5	2.5 from 2+85↓	116	2 from 2+85↓	7 1/2
2687	12-Jul-22	117	0 from 2+85↓	116	2 from 2+85↓	2
2688	12-Jul-22	124	13.5 from 2+85↓	122.5	16 from 2+85↓	3
2689	12-Jul-22	118.5	16 from 2+85↓	122.5	16 from 2+85↓	4

Crack Number	Date of Recording	Start		End		Length of Crack (in.)
		X (Offset from Centerline)	Y (Offset from Station)	X (Offset from Centerline)	Y (Offset from Station)	
2690	12-Jul-22	126.5	13 from 2+85↓	132.5	9 from 2+85↓	7
2691	12-Jul-22	119	51.5 from 2+85↓	128.5	54 from 2+85↓	10
2692	12-Jul-22	138.5	67 from 2+85↓	151	66.5 from 2+85↓	12 1/2
2693	12-Jul-22	158	61.5 from 2+85↓	151	66.5 from 2+85↓	8 1/2
2694	12-Jul-22	158	61.5 from 2+85↓	166.5	60.5 from 2+85↓	8 1/2
2695	12-Jul-22	157	63 from 2+85↓	165.5	73.5 from 2+85↓	13 1/2
2696	12-Jul-22	163.5	1.5 from 2+85↓	179.5	3.5 from 2+85↓	16
2697	12-Jul-22	173	58 from 2+85↓	188.5	59 from 2+85↓	15 1/2
2698	12-Jul-22	168	35.5 from 2+85↓	179	37.5 from 2+85↓	11
2699	12-Jul-22	180.5	54 from 2+85↓	181.5	56.5 from 2+85↓	2 1/2
2700	12-Jul-22	188	38.5 from 2+85↓	188.5	42 from 2+85↓	3 1/2
2701	12-Jul-22	216	85 from 2+85↓	213	82.5 from 2+85↓	4
2702	12-Jul-22	215	71 from 2+85↓	210	58 from 2+85↓	14
2703	12-Jul-22	211.5	81 from 2+85↓	218	75 from 2+85↓	9
2704	12-Jul-22	220.5	55 from 2+85↓	218	75 from 2+85↓	20
2705	12-Jul-22	209	82 from 2+85↓	183	84 from 2+85↓	26
2706	12-Jul-22	178.5	87 from 2+85↓	183	84 from 2+85↓	5 1/2
2707	12-Jul-22	178.5	87 from 2+85↓	196	93 from 2+85↓	18 1/2
2708	12-Jul-22	178.5	87 from 2+85↓	162.5	83 from 2+85↓	16 1/2
2709	12-Jul-22	148.5	76 from 2+85↓	142.5	73 from 2+85↓	6 1/2
2710	12-Jul-22	198.5	25.5 from 2+85↓	210	27 from 2+85↓	11 1/2
2711	12-Jul-22	211	31 from 2+85↓	210	27 from 2+85↓	4
2712	12-Jul-22	232	35.5 from 2+85↓	228	20.5 from 2+85↓	15 1/2
2713	12-Jul-22	239	73.5 from 2+85↓	233	70 from 2+85↓	7
2714	12-Jul-22	232	66 from 2+85↓	233	70 from 2+85↓	4
2715	12-Jul-22	232	66 from 2+85↓	228.5	67 from 2+85↓	3 1/2
2716	12-Jul-22	253.5	74.5 from 2+85↓	251	50.5 from 2+85↓	24
2717	12-Jul-22	240.5	60 from 2+85↓	251.5	53 from 2+85↓	13
2718	12-Jul-22	251	51 from 2+85↓	253.5	26.5 from 2+85↓	24 1/2
2719	12-Jul-22	252	41 from 2+85↓	246.5	42.5 from 2+85↓	5 1/2
2720	12-Jul-22	238	43.5 from 2+85↓	246.5	39.5 from 2+85↓	9 1/2
2721	12-Jul-22	241	3.5 from 2+85↓	251	0 from 2+85↓	10 1/2
2722	12-Jul-22	239	11 from 2+85↓	229.5	9 from 2+85↓	9 1/2

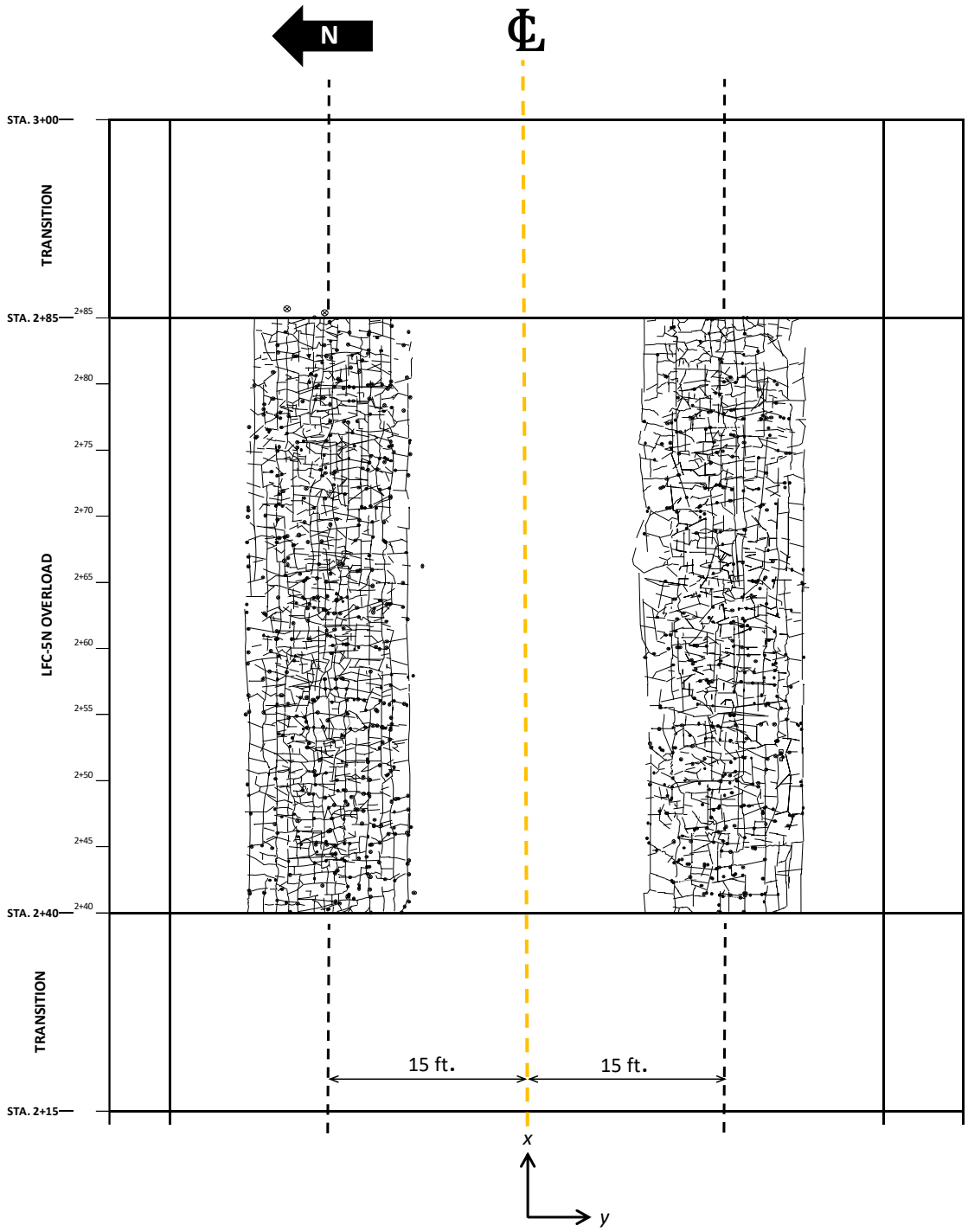

Figure D-1. Distribution of Cracks in CC9 Overload Test Items at the End of Trafficking

APPENDIX E—AIRCRAFT CLASSIFICATION NUMBER/PAVEMENT CLASSIFICATION NUMBER AND AIRCRAFT RATING NUMBER/PAVEMENT RATING NUMBER CALCULATIONS

I. PCN Analysis

Design Structure: 3-in. HMA
6-in. P-209
20-in. P-154
CBR 5 Subgrade

Standard structure for CBR method → evaluation thickness same as actual thickness.
Evaluation thickness = 29 in. on CBR 5 subgrade (ACN/PCN subgrade category C)
Assume design traffic = 1,350 annual departures of NAPTF D-36.
D-36: 36,000 lb wheel load @ 200 psi tire pressure.
Using COMFAA 3.0 obtain: **PCN 35.0/F/C**

Overload Table

Wheel Load, kips	Tire Pressure, psi	ACN/F/C	PCN/F/C	ACN/PCN
36	200	35.0	35.0	1.00
40	255	40.0	35.0	1.14
44	255	44.7	35.0	1.27
46	255	47.1	35.0	1.35
46.5	255	47.7	35.0	1.36
48	255	49.5	35.0	1.41
52	255	54.5	35.0	1.56
56	255	59.6	35.0	1.70

II. PCR Analysis

Design Structure: 3-in. HMA
6-in. P-209
20-in. P-154
CBR 5 Subgrade → E = 7500 psi (ACR/PCR category D)

Assume design traffic = 325 annual departures of NAPTF D-36.
D-36: 36,000 lb wheel load @ 200 psi tire pressure.
Using FAARFIELD 2.1, obtain **PCR 352.6/F/D**

Overload Table

Wheel Load, kips	Tire Pressure, psi	ACR/F/D	PCR/F/D	ACR/PCR
36	200	352.6	352.6	1.00
40	255	404.2	352.6	1.15
44	255	451.0	352.6	1.28
46	255	474.9	352.6	1.35
46.5	255	481.1	352.6	1.36
48	255	500.0	352.6	1.41
52	255	551.2	352.6	1.56
56	255	603.7	352.6	1.71
57	255	616.9	352.6	1.75

III. LEAF Output – 36,000 lb per wheel D-Gear (Normal Load)

Layer No.	Thickness	ELasticity Modulus	Poisson's Ratio	Interface Condition
1	3.00	200,000.0	0.350	1.000000
2	6.00	49,125.7	0.350	1.000000
3	4.00	19,603.3	0.350	1.000000
4	8.00	19,603.3	0.350	1.000000
5	8.00	13,155.0	0.350	1.000000
6	0.00	7,500.0	0.350	1.000000

Aircraft No. 1 NAPTF D36 (UDA)
Aircraft design load : Not Applicable
Fraction of load on main gear: 100.0
Gear load : 72,000.0
Number of tires : 2

Tire No.	Radius (in)	Cont.Area (sq.in)	Cont.Press (psi)	Tire Load (pounds)	X-Coord (in)	Y-Coord (in.)
1	7.57	180.00	200.00	36,000.00	-207.00	0.00
2	7.57	180.00	200.00	36,000.00	-153.00	0.00

Aircraft No. 1 NAPTF D36 (UDA)
Eval Point = 1 Layer No. = 6
X-Coord. = -180.000 Y-Coord. = 0.000 Z-Depth = 29.002900

	VERT STR	HOR Y STR	HOR X STR	XZ SHEAR	YZ SHEAR	XY SHEAR
Stress	-7.51288E+00	8.55867E-01	-2.52947E+00	0.00000E+00	0.00000E+00	0.00000E+00
Strain	-9.23616E-04	5.82758E-04	-2.66020E-05	0.00000E+00	0.00000E+00	0.00000E+00
Displt	7.95363E-02	0.00000E+00	0.00000E+00			

	PRIN 1	PRIN 2	PRIN 3	MAX SHEAR	OCT NORMAL	OCT SHEAR
Stress	-7.51288E+00	-2.52947E+00	8.55867E-01	-4.18437E+00	-3.06216E+00	3.43723E+00
Strain	-9.23616E-04	-2.66020E-05	5.82758E-04			

Eval Point = 2 Layer No. = 6
X-Coord. = -174.600 Y-Coord. = 0.000 Z-Depth = 29.002900

	VERT STR	HOR Y STR	HOR X STR	XZ SHEAR	YZ SHEAR	XY SHEAR
Stress	-7.82384E+00	8.82116E-01	-2.34676E+00	6.37262E-01	0.00000E+00	0.00000E+00
Strain	-9.74828E-04	5.92243E-04	1.10455E-05	2.29414E-04	0.00000E+00	0.00000E+00
Displt	7.98414E-02	0.00000E+00	-7.55182E-05			

	PRIN 1	PRIN 2	PRIN 3	MAX SHEAR	OCT NORMAL	OCT SHEAR
Stress	-7.89700E+00	-2.27359E+00	8.82116E-01	-4.38956E+00	-3.09616E+00	3.63095E+00
Strain	-9.87998E-04	2.42158E-05	5.92243E-04			

Eval Point = 3 Layer No. = 6
X-Coord. = -169.200 Y-Coord. = 0.000 Z-Depth = 29.002900

	VERT STR	HOR Y STR	HOR X STR	XZ SHEAR	YZ SHEAR	XY SHEAR
Stress	-8.67980E+00	9.51929E-01	-1.82779E+00	1.01507E+00	0.00000E+00	0.00000E+00
Strain	-1.11643E-03	6.17278E-04	1.16928E-04	3.65425E-04	0.00000E+00	0.00000E+00
Displt	8.06001E-02	0.00000E+00	2.43300E-04			

```
         PRIN 1       PRIN 2       PRIN 3      MAX SHEAR    OCT NORMAL   OCT SHEAR
Stress -8.82702E+00 -1.68058E+00  9.51929E-01 -4.88947E+00 -3.18522E+00  4.13158E+00
Strain -1.14293E-03  1.43426E-04  6.17278E-04

 Eval Point =    4       Layer No. =    6
 X-Coord.   =  -163.800   Y-Coord.  =    0.000   Z-Depth =  29.002900

         VERT STR     HOR Y STR    HOR X STR    XZ SHEAR     YZ SHEAR     XY SHEAR
Stress -9.81646E+00  1.03906E+00 -1.09323E+00  8.89078E-01  0.00000E+00  0.00000E+00
Strain -1.30633E-03  6.47660E-04  2.63848E-04  3.20068E-04  0.00000E+00  0.00000E+00
Displt  8.13509E-02  0.00000E+00  1.26297E-03

         PRIN 1       PRIN 2       PRIN 3      MAX SHEAR    OCT NORMAL   OCT SHEAR
Stress -9.90615E+00  1.03906E+00 -1.00353E+00 -4.45131E+00 -3.29021E+00  4.75192E+00
Strain -1.32248E-03  6.47660E-04  2.79993E-04

 Eval Point =    5       Layer No. =    6
 X-Coord.   =  -158.400   Y-Coord.  =    0.000   Z-Depth =  29.002900

         VERT STR     HOR Y STR    HOR X STR    XZ SHEAR     YZ SHEAR     XY SHEAR
Stress -1.07627E+01  1.10486E+00 -3.95118E-01  1.39546E-01  0.00000E+00  0.00000E+00
Strain -1.46815E-03  6.68013E-04  3.98018E-04  5.02364E-05  0.00000E+00  0.00000E+00
Displt  8.14097E-02  0.00000E+00  3.07070E-03

         PRIN 1       PRIN 2       PRIN 3      MAX SHEAR    OCT NORMAL   OCT SHEAR
Stress -1.07646E+01  1.10486E+00 -3.93240E-01 -5.18567E+00 -3.35099E+00  5.27776E+00
Strain -1.46849E-03  6.68013E-04  3.98356E-04

 Eval Point =    6       Layer No. =    6
 X-Coord.   =  -153.000   Y-Coord.  =    0.000   Z-Depth =  29.002900

         VERT STR     HOR Y STR    HOR X STR    XZ SHEAR     YZ SHEAR     XY SHEAR
Stress -1.09985E+01  1.11206E+00 -3.65266E-02 -1.07476E+00  0.00000E+00  0.00000E+00
Strain -1.51666E-03  6.63244E-04  4.56498E-04 -3.86915E-04  0.00000E+00  0.00000E+00
Displt  8.01134E-02  0.00000E+00  5.42321E-03

         PRIN 1       PRIN 2       PRIN 3      MAX SHEAR    OCT NORMAL   OCT SHEAR
Stress -1.11029E+01  1.11206E+00  6.78543E-02 -5.58538E+00 -3.30766E+00  5.52853E+00
Strain -1.53545E-03  6.63244E-04  4.75286E-04
```

IV. LEAF Output – 57,000 lb per wheel D-Gear (Overload)

Layer No.	Thickness	ELasticity Modulus	Poisson's Ratio	Interface Condition
1	3.00	200,000.0	0.350	1.000000
2	6.00	49,125.7	0.350	1.000000
3	4.00	19,603.3	0.350	1.000000
4	8.00	19,603.3	0.350	1.000000
5	8.00	13,155.0	0.350	1.000000
6	0.00	7,500.0	0.350	1.000000

Aircraft No. 1 NAPTF-Overload2(UDA)
Aircraft design load : Not Applicable
Fraction of load on main gear: 100.0
Gear load : 114,000.0
Number of tires : 2

Tire No.	Radius (in)	Cont.Area (sq.in)	Cont.Press (psi)	Tire Load (pounds)	X-Coord (in)	Y-Coord (in.)
1	8.44	223.53	255.00	57,000.00	-207.00	0.00
2	8.44	223.53	255.00	57,000.00	-153.00	0.00

Aircraft No. 1 NAPTF-Overload2(UDA)
Eval Point = 1 Layer No. = 6
X-Coord. = -180.000 Y-Coord. = 0.000 Z-Depth = 29.002900

	VERT STR	HOR Y STR	HOR X STR	XZ SHEAR	YZ SHEAR	XY SHEAR
Stress	-1.19139E+01	1.32950E+00	-3.95146E+00	0.00000E+00	0.00000E+00	0.00000E+00
Strain	-1.46616E-03	9.17649E-04	-3.29232E-05	0.00000E+00	0.00000E+00	0.00000E+00
Displt	1.25846E-01	0.00000E+00	0.00000E+00			

	PRIN 1	PRIN 2	PRIN 3	MAX SHEAR	OCT NORMAL	OCT SHEAR
Stress	-1.19139E+01	-3.95146E+00	1.32950E+00	-6.62169E+00	-4.84528E+00	5.44340E+00
Strain	-1.46616E-03	-3.29232E-05	9.17649E-04			

Eval Point = 2 Layer No. = 6
X-Coord. = -174.600 Y-Coord. = 0.000 Z-Depth = 29.002900

	VERT STR	HOR Y STR	HOR X STR	XZ SHEAR	YZ SHEAR	XY SHEAR
Stress	-1.23948E+01	1.36831E+00	-3.66563E+00	9.74752E-01	0.00000E+00	0.00000E+00
Strain	-1.54543E-03	9.31929E-04	2.58199E-05	3.50911E-04	0.00000E+00	0.00000E+00
Displt	1.26309E-01	0.00000E+00	-7.14111E-05			

	PRIN 1	PRIN 2	PRIN 3	MAX SHEAR	OCT NORMAL	OCT SHEAR
Stress	-1.25023E+01	-3.55811E+00	1.36831E+00	-6.93533E+00	-4.89738E+00	5.74131E+00
Strain	-1.56479E-03	4.51739E-05	9.31929E-04			

Eval Point = 3 Layer No. = 6
X-Coord. = -169.200 Y-Coord. = 0.000 Z-Depth = 29.002900

	VERT STR	HOR Y STR	HOR X STR	XZ SHEAR	YZ SHEAR	XY SHEAR
Stress	-1.37120E+01	1.47099E+00	-2.85857E+00	1.54078E+00	0.00000E+00	0.00000E+00
Strain	-1.76351E-03	9.69424E-04	1.90104E-04	5.54681E-04	0.00000E+00	0.00000E+00
Displt	1.27450E-01	0.00000E+00	4.70738E-04			

```
         PRIN 1       PRIN 2       PRIN 3      MAX SHEAR    OCT NORMAL   OCT SHEAR
Stress -1.39265E+01 -2.64407E+00  1.47099E+00 -7.69873E+00 -5.03319E+00  6.50904E+00
Strain -1.80212E-03  2.28713E-04  9.69424E-04

 Eval Point =    4       Layer No. =    6
 X-Coord.   =  -163.800   Y-Coord.  =    0.000   Z-Depth =  29.002900

         VERT STR     HOR Y STR    HOR X STR    XZ SHEAR     YZ SHEAR     XY SHEAR
Stress -1.54447E+01  1.59784E+00 -1.72736E+00  1.32529E+00  0.00000E+00  0.00000E+00
Strain -2.05325E-03  1.01441E-03  4.15871E-04  4.77104E-04  0.00000E+00  0.00000E+00
Displt  1.28550E-01  0.00000E+00  2.09503E-03

         PRIN 1       PRIN 2       PRIN 3      MAX SHEAR    OCT NORMAL   OCT SHEAR
Stress -1.55716E+01 -1.60049E+00  1.59784E+00 -8.58470E+00 -5.19140E+00  7.45511E+00
Strain -2.07608E-03  4.38707E-04  1.01441E-03

 Eval Point =    5       Layer No. =    6
 X-Coord.   =  -158.400   Y-Coord.  =    0.000   Z-Depth =  29.002900

         VERT STR     HOR Y STR    HOR X STR    XZ SHEAR     YZ SHEAR     XY SHEAR
Stress -1.68687E+01  1.69185E+00 -6.62171E-01  1.60366E-01  0.00000E+00  0.00000E+00
Strain -2.29721E-03  1.04369E-03  6.19961E-04  5.77317E-05  0.00000E+00  0.00000E+00
Displt  1.28557E-01  0.00000E+00  4.92410E-03

         PRIN 1       PRIN 2       PRIN 3      MAX SHEAR    OCT NORMAL   OCT SHEAR
Stress -1.68702E+01  1.69185E+00 -6.60584E-01 -8.10483E+00 -5.27966E+00  8.25186E+00
Strain -2.29749E-03  1.04369E-03  6.20247E-04

 Eval Point =    6       Layer No. =    6
 X-Coord.   =  -153.000   Y-Coord.  =    0.000   Z-Depth =  29.002900

         VERT STR     HOR Y STR    HOR X STR    XZ SHEAR     YZ SHEAR     XY SHEAR
Stress -1.72074E+01  1.69937E+00 -1.14644E-01 -1.70268E+00  0.00000E+00  0.00000E+00
Strain -2.36827E-03  1.03494E-03  7.08422E-04 -6.12967E-04  0.00000E+00  0.00000E+00
Displt  1.26468E-01  0.00000E+00  8.57929E-03

         PRIN 1       PRIN 2       PRIN 3      MAX SHEAR    OCT NORMAL   OCT SHEAR
Stress -1.73754E+01  1.69937E+00  5.33179E-02 -8.71434E+00 -5.20756E+00  8.63014E+00
Strain -2.39851E-03  1.03494E-03  7.38655E-04
```

APPENDIX F—FINITE ELEMENT MODEL ASSUMPTIONS AND CONDITIONS

Table E-1. Summary of Material Properties Used in ABAQUS

Pavement Layer	Modulus (psi)	Poisson's Ratio	Thickness (in.)
P-401 HMA Surface	200,000	0.35	3
P-209 Crushed Aggregate Base	49,125	0.35	6
P-154 Uncrushed Aggregate Subbase	15,000	0.35	20
Subgrade	7,500	0.35	100

Table E-2. Description of Pavement Geometry and Mesh Sizes

Pavement Layer	Width (ft) x Length (ft)	Mesh Size (in.)	Refined Mesh Size (in.)	Thickness (in.)	Mesh Size along Depth (in.)
P-401 HMA Surface	30 x 30	11.8	2.0	3	1.0
P-209 Crushed Aggregate Base				6	1.0
P-154 Uncrushed Aggregate Subbase				20	2.0
Subgrade				100	Varied (1.0 to 12.0)

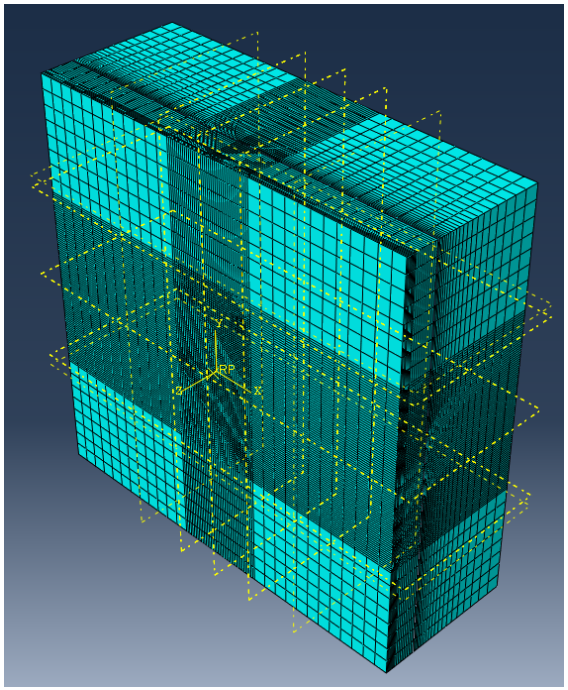

Figure E-1. Image of the Finite Element Mesh Including the Refined Mesh Area in the Wheel Load Area

Table E-3. Description of Pavement Boundary and Interface Conditions

Pavement Condition	Constraint	Description
Pavement Boundaries (All Sides and Bottom of Subgrade)	Pinned Boundary Condition	Restricts translation but allows rotation.
Surface Interface	Tie Constraint	Bonds the two surfaces together ensuring they move as a single unit, regardless of their mesh or material differences.
Tire – Surface Interface	Tie Constraint	Bonds the two surfaces together ensuring they move as a single unit, regardless of their mesh or material differences.